

Protected phase gate for the $0-\pi$ qubit using its internal modes

Xanda C. Kolesnikow, Thomas B. Smith, Felix Thomsen, Abhijeet A. Alase, and Andrew C. Doherty
*Centre for Engineered Quantum Systems, School of Physics,
 University of Sydney, Sydney, NSW 2006, Australia.*
 (Dated: March 20, 2025)

Protected superconducting qubits such as the $0-\pi$ qubit promise to substantially reduce physical error rates through a multi-mode encoding. This protection comes at the cost of controllability, as standard techniques for quantum gates are ineffective. We propose a protected phase gate for the $0-\pi$ qubit that utilises an internal mode of the circuit as an ancilla. The gate is achieved by varying the qubit-ancilla coupling via a tunable Josephson element. Our scheme is a modified version of a protected gate proposed by Brooks, Kitaev and Preskill that uses an external oscillator as an ancilla. We find that our scheme is compatible with the protected regime of the $0-\pi$ qubit, and does not suffer from spurious coupling to additional modes of the $0-\pi$ circuit. Through numerical simulations, we study how the gate error scales with the circuit parameters of the $0-\pi$ qubit and the tunable Josephson element that enacts the gate.

I. INTRODUCTION

Superconducting quantum circuits are a leading platform to achieve the low error rates demanded by quantum error-correcting codes [1, 2]. Qubits are typically encoded in single-mode circuits, such as the transmon [3] and fluxonium [4]. These relatively simple circuits can be engineered to highly suppress either bit-flips or phase-flips, but not both simultaneously. Substantial reduction of error rates beyond the state-of-the-art may require qubits encoded in more complex multi-mode circuits that are capable of suppressing both types of errors [5].

The $0-\pi$ qubit shown in Fig. 1(a) is a promising example of one such protected qubit [6, 7]. In an appropriate regime of the circuit parameters, this circuit encodes a nearly-degenerate qubit that is resilient to both bit-flips and phase-flips [8]. This protection arises from the multi-mode nature of the encoding; the $0-\pi$ qubit is encoded in two nonlinearly coupled modes of its circuit, labelled θ and φ in Fig. 1(a). The transmon-like mode θ is concatenated with the fluxonium-like mode φ , affording the $0-\pi$ qubit more protection than would be possible with a single mode. Despite its apparent complexity, the $0-\pi$ circuit has been experimentally realised, albeit in a ‘soft’ parameter regime where the encoded qubit is partially protected [9]. Current experimental efforts are dedicated to improving qubit protection by pushing into the ‘hard’ parameter regime [10, 11].

A consequence of increased qubit protection is an increased difficulty to perform quantum gates by conventional means. Rabi-style gates are infeasible for protected qubits since the matrix elements between computational states are small by design. This can be overcome in the near-term by utilising non-computational states for Raman-style gates [9, 12]. However, this strategy is only feasible for $0-\pi$ qubits in the partially protected parameter regime, and not in the protected regime.

In this paper, we propose a protected phase gate for the $0-\pi$ qubit that is compatible with its protected regime. The gate utilises the internal harmonic mode of the $0-\pi$ circuit, labelled ζ in Fig. 1(a), as an ancilla. Our imple-

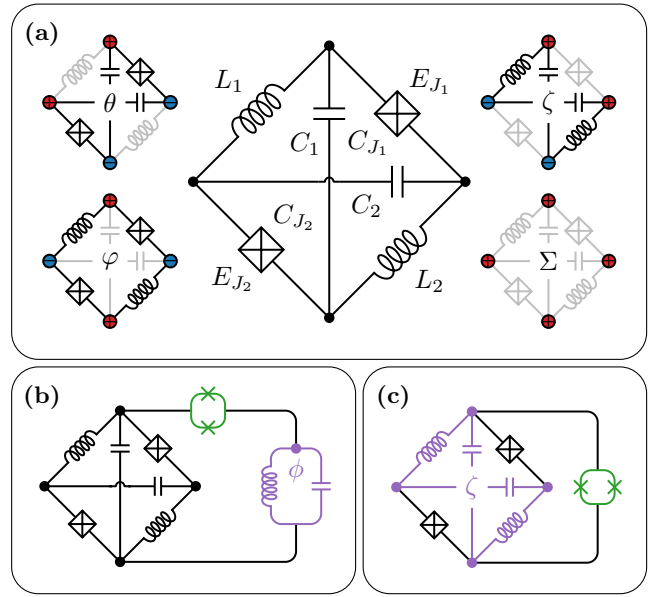


FIG. 1. Protected gates for the $0-\pi$ qubit. (a) Circuit diagram for the $0-\pi$ qubit; two capacitors, two inductors, and two Josephson junctions are connected in the geometry shown. The circuit has four quadrupole circuit modes; the θ and φ modes encode the qubit, the ζ mode is harmonic, and Σ is non-dynamical. (b) Implementation of the protected phase gate proposed in Refs. [6, 7]. A tunable Josephson element (green) couples the $0-\pi$ qubit to an oscillator mode ϕ (purple). (c) Our modified scheme that utilises the internal harmonic mode ζ (purple) instead of an external oscillator.

mentation is based on the Brooks-Kitaev-Preskill (BKP) protected gate proposed in Refs. [6, 7].

The BKP gate relies on a high-impedance harmonic oscillator that is coupled to a protected qubit via a tunable Josephson element. By appropriately varying the qubit-oscillator coupling, a logical phase gate can be enacted on the qubit. This phase gate does not break the protection of the qubit, has an error rate that is exponentially suppressed in the impedance of the oscillator, and is (to some degree) insensitive to the precise details of

the coupling pulse that enacts the gate. These qualities make the BKP gate a prime candidate for a protected $0-\pi$ qubit gate.

However, the proposed implementation of their gate, shown in Fig. 1(b), is complicated by the multi-mode nature of the $0-\pi$ qubit. As identified in Ref. [12], the qubit-oscillator coupling also involves the ζ mode:

$$\hat{H}_{\text{int}}(t) = -E_{J_{\text{int}}}(t) \cos(\hat{\phi} - \hat{\theta} + \hat{\zeta}). \quad (1)$$

This has deleterious effects on the performance of the gate. Since the ζ mode is harmonic, the coupling is suppressed by a factor proportional to $\langle \cos \hat{\zeta} \rangle \propto e^{-\pi Z_{\zeta}/2R_Q}$, where Z_{ζ} is the ζ -mode impedance, and $R_Q = h/4e^2$ is the superconducting resistance quantum. We show that this scaling is in direct competition with the protected regime of the $0-\pi$ qubit, which benefits from a large ζ -mode impedance.

We circumvent this problem by utilising the ζ mode as the requisite ancilla. Our implementation is shown in Fig. 1(c). This leads to an interaction of the form

$$\hat{H}_{\text{int}}(t) = -E_{J_{\text{int}}}(t) \cos(\hat{\theta} + \hat{\zeta}). \quad (2)$$

In this case, the coupling is no longer exponentially suppressed in the ζ -mode impedance and is therefore compatible with the protected regime of the $0-\pi$ qubit. This modification also reduces the hardware requirements for the gate by eliminating the need for an external high-impedance oscillator.

We analyse the efficacy of this scheme using numerical simulations, and compare our proposal to the original BKP gate. Our simulations show that a protected gate using an external oscillator would require excessively large Josephson coupling energies, whereas our scheme does not. We also find that a large ζ -mode impedance in combination with the large charging energy ratio of the $0-\pi$ qubit leads to an even larger φ -mode impedance required for a protected gate. In particular, we find that both schemes require a φ -mode impedance (which is the largest impedance of the $0-\pi$ circuit) of at least fifty times the resistance quantum, but that unprotected gates with error rates below 10^{-3} may be obtained at smaller impedances. We also analyse the effect of circuit disorder and show that our gate is robust to circuit parameter asymmetries of up to 25%.

The structure of this paper is as follows. In Section II we provide a review of the protected phase gate proposed in Refs. [6, 7]. As a point of reference, we simulate its performance for an idealised protected qubit, and determine the hardware requirements for a protected gate. In Section III we turn our attention to the implementation of a protected phase with the $0-\pi$ qubit. We describe our proposal that utilises the ζ mode as an ancilla, and compare our gate to the implementation proposed in Ref. [7] through numerical simulations. We show that our proposal is compatible with the protected regime of the $0-\pi$ qubit. We also introduce a one-dimensional model for the $0-\pi$ qubit, and discuss the possibility of a gate that

uses the φ mode as an ancilla. In Section IV we discuss the hardware requirements of our proposal. This includes simulations of the gate with $0-\pi$ circuit disorder, and simulations that quantify the constraints on circuit parameters for both of the $0-\pi$ circuit and the tunable Josephson element. We also discuss of the role of cooling and photon loss. In Section V we propose possible extensions of our scheme to protected magic gates and protected two-qubit gates. We conclude in Section VI.

II. PROTECTED GATE FOR AN IDEAL QUBIT

In this section, we review the single-qubit protected phase gate proposed in Ref. [6, 7]. To keep our discussion focused on the gate itself, we consider the implementation of the protected gate with an ideal protected qubit. The setup is shown in Fig. 2(a); a protected qubit mode θ is coupled to a harmonic oscillator mode ϕ via a tunable Josephson element (depicted here as a SQUID). The basic principle of the gate is as follows.

When the qubit-oscillator coupling is turned on, the oscillator evolves into an approximate Gottesman-Kitaev-Preskill (GKP) qubit codeword [13] that is dependent on the state of the protected qubit. The oscillator is then allowed to evolve for a time τ in order to perform a logical phase gate on the GKP state encoded in the oscillator. When the qubit-oscillator coupling is turned off, the oscillator returns to its original state, but with an accrued phase. At the end of this sequence, the system has acquired a qubit-state-dependent phase due to the evolution of the oscillator. We provide a detailed description of this gate sequence in the following sections.

In Section II A we describe the Hamiltonian for this circuit, which we find is most conveniently understood in terms of GKP stabiliser generators and logical operators. Following this, in Section II B we detail the evolution of the system throughout the gate sequence. Finally, in Section II C we determine through numerical simulations the circuit parameters required of the oscillator and tunable coupler to obtain a protected gate.

A. Hamiltonian

For this discussion we assume an ideal protected qubit, labelled θ in Fig. 2(a). The circuit consists of a π -periodic Josephson element with energy E_J shunted by a capacitor with capacitance C . The Josephson element only allows for the tunnelling of pairs of Cooper pairs. The Hamiltonian for this circuit is

$$\hat{H}_{\theta} = 4E_C \hat{n}_{\theta}^2 - E_J \cos 2\hat{\theta}, \quad (3)$$

where $[\hat{\theta}, \hat{n}_{\theta}] = i$ and $E_C = e^2/2C$. This Hamiltonian possesses a double-well potential with minima at $\theta = 0$ and $\theta = \pi$, as illustrated in Fig. 2(b). For $E_J \gg E_C$ the circuit has a pair of nearly degenerate ground states.

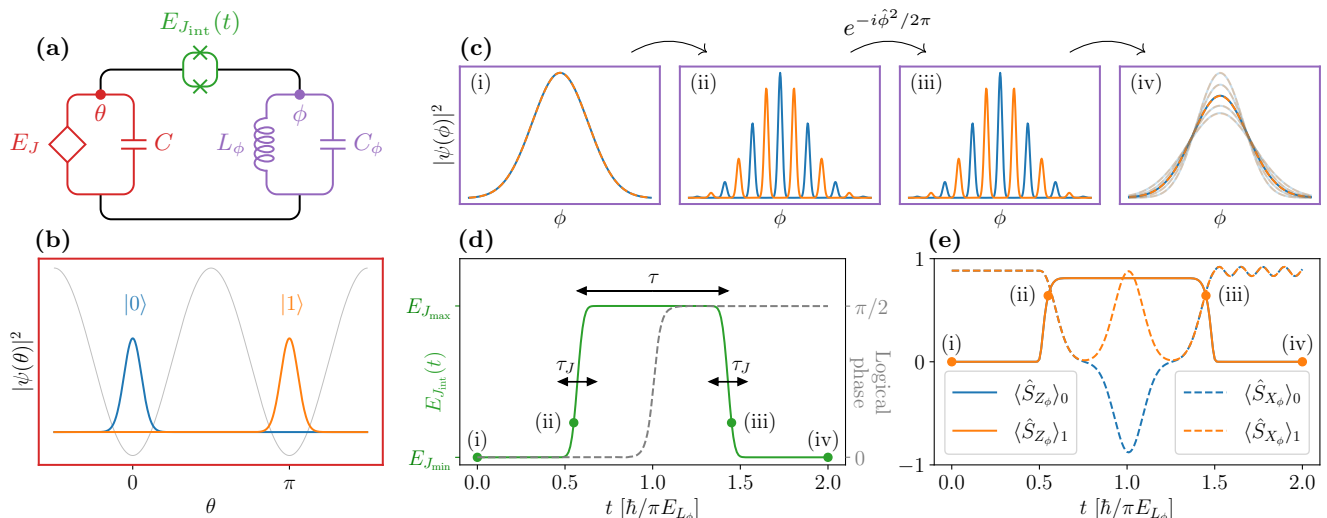


FIG. 2. Protected phase gate for a protected qubit. (a) Circuit diagram for a protected qubit mode θ (red) coupled to a harmonic oscillator mode ϕ (purple) via a tunable Josephson element (green). (b) Approximate eigenstates of the protected qubit GKP logical operator \bar{Z}_θ . Blue and orange wavefunctions corresponds to $\langle \bar{Z}_\theta \rangle \approx \pm 1$, respectively, and the potential energy for the qubit is shown in grey. (c) Qubit-state-dependent oscillator wavefunctions at various points in the gate sequence. (d) Pulse schedule for the tunable Josephson coupling (green); characterised by a wait-time τ and a ramp-time τ_J . Also shown, is the relative logical phase (grey) acquired by the states $|0\rangle$ and $|1\rangle$ throughout the gate sequence. (e) GKP stabiliser generator expectation values of the oscillator throughout the gate sequence.

These ground states are approximate GKP qubit codewords [13, 14], defined by the stabiliser generators,

$$\hat{S}_{X_\theta} = e^{-2i\pi\hat{n}_\theta}, \quad \hat{S}_{Z_\theta} = e^{2i\hat{\theta}}. \quad (4)$$

and the logical operators

$$\bar{X}_\theta = e^{-i\pi\hat{n}_\theta}, \quad \bar{Z}_\theta = e^{i\hat{\theta}}. \quad (5)$$

Due to the periodic boundary conditions of the rotor mode θ , every state in the Hilbert space of Eq. (3) satisfies $\langle \hat{S}_{X_\theta} \rangle = 1$. Furthermore, for $E_J \gg E_C$ the ground states also satisfy $\langle \hat{S}_{Z_\theta} \rangle \approx \exp(-\sqrt{2E_C/E_J})$. This can be shown by Taylor-expanding the double-well potential at $\theta = 0$ or $\theta = \pi$ and calculating the expectation value of the approximately harmonic wavefunctions. Thus, for $E_J \gg E_C$, Eq. (3) passively stabilises a GKP qubit encoded in a rotor. This results in a highly protected superconducting qubit [6]. Note that the ground states of the circuit are exact eigenstates of \bar{X}_θ . This is attributable to the perfect π -periodicity of the Hamiltonian.

The protected qubit is coupled to a high-impedance harmonic oscillator ϕ by a tunable Josephson element. The circuit Hamiltonian is $\hat{H}(t) = \hat{H}_\theta + \hat{H}_\phi + \hat{H}_{\text{int}}(t)$. The oscillator is described by the Hamiltonian

$$\hat{H}_\phi = 4E_{C_\phi}\hat{n}_\phi^2 + \frac{E_{L_\phi}}{2}\hat{\phi}^2, \quad (6)$$

where $[\hat{\phi}, \hat{n}_\phi] = i$, $E_{C_\phi} = e^2/2C_\phi$, $E_{L_\phi} = \phi_0^2/L_\phi$, and $\phi_0 = \hbar/2e$. The tunable Josephson element connecting θ and ϕ leads to a time-dependent interaction of the form

$$\hat{H}_{\text{int}}(t) = -E_{J_{\text{int}}}(t) \cos(\hat{\phi} - \hat{\theta}), \quad (7)$$

where $E_{J_{\text{int}}}(t)$ is the tunable Josephson energy. For simplicity, we assume the tunable Josephson element has no capacitance, and postpone an analysis of non-zero capacitance to Section IV B.

If the coupling is turned on at the correct rate, an approximate GKP qubit codeword is prepared in the oscillator. With this in mind, we rewrite Eq. (7) as

$$\hat{H}_{\text{int}}(t) = -\frac{E_{J_{\text{int}}}(t)}{2}(\bar{Z}_\phi\bar{Z}_\theta^{-1} + \bar{Z}_\theta\bar{Z}_\phi^{-1}), \quad (8)$$

where $\bar{Z}_\phi = e^{i\hat{\phi}}$ is the Z -type GKP logical operator for the oscillator. This form of the interaction Hamiltonian elucidates the nature of the tunable Josephson element; it acts as a GKP logical ZZ interaction between the protected qubit and the oscillator. When the qubit-oscillator coupling is turned on, the oscillator evolves to an eigenstate of \bar{Z}_ϕ that is dependent on the expectation value of the qubit logical operator \bar{Z}_θ . This interaction is the foundation of the protected phase gate, which we describe in the following section.

B. Gate sequence

The protected phase gate is most easily understood by tracking the evolution of the oscillator. Let us assume that the protected qubit is in an eigenstate of \bar{Z}_θ , such that $\langle \bar{Z}_\theta \rangle = \pm 1$. The Hamiltonian for the oscillator has the simplified form

$$\hat{H}(t) = 4E_{C_\phi}\hat{n}_\phi^2 + \frac{E_{L_\phi}}{2}\hat{\phi}^2 \mp \frac{E_{J_{\text{int}}}(t)}{2}(\bar{Z}_\phi + \bar{Z}_\phi^{-1}). \quad (9)$$

We neglect the qubit mode θ for this discussion since it is expected to be minimally affected during the gate. This is because the qubit is approximately stabilised by the operators \hat{S}_{X_θ} and \hat{S}_{Z_θ} . Since the interaction Hamiltonian in Eq. (8) commutes with both of these stabilisers, the qubit remains protected throughout the gate.

Figure 2(c) shows the qubit-state-dependent oscillator wavefunctions at four key moments throughout the gate, labelled (i) through to (iv). These are also indicated on Fig. 2(d), which shows the time-dependent Josephson coupling pulse that enacts the gate, and Fig. 2(e) which shows the GKP stabiliser expectation values of the oscillator. We colour-code the plots based on the the initial state of the qubit. Blue corresponds to a protected qubit state localised at $\theta = 0$ with $\langle \bar{Z}_\theta \rangle = +1$, and orange corresponds to a protected qubit state localised at $\theta = \pi$ with $\langle \bar{Z}_\theta \rangle = -1$. We stress that the expectation values plotted in Fig. 2(e) pertain to the dynamics of the oscillator mode ϕ , and not the qubit mode θ .

The start of the gate sequence is denoted (i). At this point, the Josephson coupling is at a minimum value $E_{J_{\min}} \ll E_{C_\phi}, E_{L_\phi}$ such that the oscillator is approximately in the ground state of Eq. (6). This ground state has a large variance in ϕ owing to the high impedance of the oscillator. The GKP stabiliser expectation values at this point in the sequence are

$$\langle \hat{S}_{X_\phi} \rangle = e^{-\pi R_Q/2Z_\phi}, \quad \langle \hat{S}_{Z_\phi} \rangle = e^{-2\pi Z_\phi/R_Q}, \quad (10)$$

where $\hat{S}_{X_\phi} = e^{-2i\pi\hat{n}_\phi}$ and $\hat{S}_{Z_\phi} = e^{2i\hat{\phi}}$ are the GKP stabiliser generators for the oscillator, and $Z_\phi = \sqrt{L_\phi/C_\phi}$ is the impedance of the oscillator. Consequently, we have that $\langle \hat{S}_{X_\phi} \rangle \approx 1$ and $\langle \hat{S}_{Z_\phi} \rangle \approx 0$.

The Josephson coupling is then turned on at a rate characterised by the ramp-time $\tau_J \approx \hbar/\sqrt{8E_{C_\phi}E_{L_\phi}}$. The ramp-time must be slow enough to prevent plasmonic excitations within each well of the cosine potential, but fast enough to preserve the envelope of the initial state. Once the Josephson coupling reaches a value $E_{J_{\text{int}}}(t) \gg E_{C_\phi}, E_{L_\phi}$, the logical ZZ interaction between the protected qubit and oscillator dominates. The oscillator evolves to an approximate eigenstate of \bar{Z}_ϕ , and $\langle \hat{S}_{Z_\phi} \rangle$ increases. At point (ii) in Fig. 2(e), the expectation values of both the X - and Z -type stabiliser generators are close to one. This signifies that the state of the oscillator is in the approximate GKP codespace.

From here, the GKP state prepared in the oscillator starts to evolve under the inductive term in Eq. (6). The unitary evolution after a time t is given by the operator

$$\hat{U}(t) = e^{-iE_{L_\phi}\hat{\phi}^2 t/2\hbar}. \quad (11)$$

This operator commutes with \hat{S}_{Z_ϕ} , but not \hat{S}_{X_ϕ} . The effect of this can be observed in Fig. 2(e): the mid-pulse expectation values of the X -type stabiliser differs depending on the initial qubit logical state. This leads to a fault-tolerant logical phase gate for the GKP state encoded in the oscillator after an evolution time $t = \hbar/\pi E_{L_\phi}$ [13].

At point (iii), the oscillator is back in the approximate GKP codespace after having acquired a state-dependent phase. However, the system acquires a relative phase dependent on the initial state of the qubit. The evolution of this relative phase is plotted in grey in Fig. 2(d).

The end of the gate sequence is denoted (iv). When the coupling is turned off at the rate characterised by τ_J , the oscillator returns to an approximate ground state of Eq. (6), but may be left with some excess entropy depending on the exact timing of the pulse. This mistiming error leaves the oscillator ‘ringing’, which is observed in the oscillations of $\langle \hat{S}_{X_\phi} \rangle$ in Fig. 2(e). Importantly, this extra entropy may be extracted by cooling the oscillator mode, leaving the qubit unaffected.

This gate is protected for three reasons. First, the qubit-oscillator coupling commutes with the stabiliser generators of the protected qubit. Second, the high impedance of the oscillator along with the strong Josephson coupling allow for the preparation of an approximate GKP logical state in the oscillator. Third, the GKP state encoded in the oscillator possesses a fault-tolerant logical phase gate.

The second condition places constraints on the oscillator impedance Z_ϕ and the maximum Josephson coupling $E_{J_{\max}}$. If they are not sufficiently large, then the state in the oscillator will be a poor approximation of a GKP state. We require the following energy hierarchy:

$$E_{L_\phi} \ll E_{C_\phi} \ll E_{J_{\max}}. \quad (12)$$

The third condition provides flexibility in the details of the pulse shape $E_{J_{\text{int}}}(t)$. Due to the fault-tolerant nature of the GKP logical phase gate, the gate is robust to errors in the pulse wait-time τ and ramp-time τ_J . The degree to which the gate is robust is determined by the quality of the GKP state. Thus, lower tolerance to errors can be traded for reduced hardware requirements on Z_ϕ and $E_{J_{\max}}$ and vice versa. In the following section, we numerically quantify constraints on these parameters to obtain a protected gate.

C. Numerical simulations

Here we simulate the dynamics of the protected gate under the Hamiltonian $\hat{H}(t) = \hat{H}_\theta + \hat{H}_\phi + \hat{H}_{\text{int}}(t)$ where the three terms are given by Eqs. (3), (6) and (7), respectively. When $E_{J_{\text{int}}}(t) = 0$, the two ground states of this Hamiltonian have a tensor product structure:

$$|+\rangle = |+\rangle_\theta \otimes |0\rangle_\phi, \quad |-\rangle = |-\rangle_\theta \otimes |0\rangle_\phi, \quad (13)$$

where $|\pm\rangle_\theta$ are the ± 1 eigenstates of the GKP logical operator \bar{X}_θ and the ground states of Eq. (3), and $|0\rangle_\phi$ is the harmonic ground state Eq. (6). We emphasise that the following simulations treat both the qubit and oscillator as dynamical variables, and do not assume a perfect qubit like the previous section. We provide the details of our numerical methods in Appendix B.

For our simulations, we initialise the system in the ground state $|\psi_i\rangle = |+\rangle_\theta \otimes |0\rangle_\phi$. We vary the Josephson coupling following the error-function-shaped pulse shown in Fig. 2(d). As described in the previous section, this should result in a logical phase and the final state $|\psi_f\rangle = |-i\rangle_\theta \otimes |0\rangle_\phi$, where $|-i\rangle_\theta$ is the -1 eigenstate of the GKP logical operator \bar{Y}_θ .

We use a metric for the gate performance that takes into account the passive error-correcting properties of the $0-\pi$ qubit. Whilst the logical operator \bar{Z}_θ may be used, this is overly pessimistic since superpositions of the ground states of Eq. (3) are only ± 1 eigenstates of this operator in the $E_J/E_C \rightarrow \infty$ limit. Due to the properties of the GKP code, the modular value of θ can be used to determine the qubit state, whereby states whose support lies in the range $\theta = [-\pi/2, \pi/2)$ are deemed to be correctable to $|0\rangle$ and states whose support lies in $\theta = [\pi/2, 3\pi/2)$ are deemed to be correctable to $|1\rangle$. To this end, in Appendix C1 we use a subsystem decomposition [15, 16] to define effective qubit operators \bar{X}_{eff} , \bar{Y}_{eff} , and \bar{Z}_{eff} , whereby the ± 1 eigenstates of \bar{Z}_{eff} are precisely the states that can be corrected to produce logical eigenstates of \bar{Z}_θ . We stress that this simply amounts to a redefinition of the qubit and does not imply any additional error-correction protocol is required.

In Appendix C2 we show that the diamond norm deviation of the gate from its ideal action may be expressed in terms of these operators as

$$\varepsilon_\diamond = \frac{1}{2} \sqrt{(1 + \langle \bar{Y}_{\text{eff}} \rangle)^2 + \langle \bar{X}_{\text{eff}} \rangle^2}, \quad (14)$$

where the expectation values are taken with respect to the final state after the gate. Note that because the effective qubit operators act as the identity on the oscillator Hilbert space, this metric is agnostic to the state of the oscillator. We use the diamond norm deviation rather than the average gate fidelity because it aligns with the gate error in threshold theorems [17–19]. For coherent errors, which we focus on here, the average gate fidelity potentially underestimates the effect of an error in the context of fault-tolerant quantum computing [20, 21].

We describe the qubit-oscillator system with the following parameters for our simulations. The qubit is characterised by the tunnelling energy ratio E_J/E_{C_ϕ} , and the oscillator by its impedance Z_ϕ/R_Q . The relative energy scale of the two systems is determined by the charging energy ratio E_{C_ϕ}/E_C , and the Josephson coupling between them is captured by the minimum and maximum coupling ratios $E_{J_{\min}}/E_{C_\phi}$ and $E_{J_{\max}}/E_{C_\phi}$, respectively.

1. Impedance of the oscillator

Our first set of simulations interrogate the protected nature of the gate for different values of the oscillator impedance. For these simulations we set $E_{J_{\min}}/E_{C_\phi} = 0$ and $E_{J_{\max}}/E_{C_\phi} = 100$. In the following section we show

that these constraints can be relaxed while maintaining a protected gate.

To analyse the protection of the phase gate, we consider the effect of a mistimed pulse on the gate error ε_\diamond . An unprotected gate (e.g. a Rabi pulse) is one in which a mistimed gate leads to a linear increase in the gate error when measured by the diamond norm. In contrast, a protected gate is one whose sensitivity to gate mistiming is exponentially suppressed in some system parameter.

In Fig. 3(a) we plot the gate error ε_\diamond as a function of the mistiming parameter

$$\delta\tau = \tau - \tau_{\text{opt}}, \quad (15)$$

where τ is the pulse wait-time as indicated in Fig. 2(d), and τ_{opt} is the optimal wait-time. We plot the gate error for multiple values of Z_ϕ/R_Q and observe two qualitatively different types of gates. For $Z_\phi/R_Q = 2$ (dashed line), the gate error increases linearly around $\delta\tau = 0$, signifying an unprotected gate. For $Z_\phi/R_Q = 4-10$ (solid lines), the gate error is extremely flat near $\delta\tau = 0$, indicating that the gate is protected against mistiming.

We consider two characteristic parameters to quantify the imprecision and robustness of the protected gate. Imprecision is captured by the minimum gate error $\min(\varepsilon_\diamond)$ at $\delta\tau = 0$. Robustness is captured by the maximum range of mistiming $\Delta_\tau(\varepsilon_\diamond^*)$ to remain below a particular gate error threshold ε_\diamond^* . A protected gate should have an imprecision that is exponentially suppressed in some circuit parameter, along with some non-zero robustness at a reasonable threshold error rate. We plot both of these quantities as a function Z_ϕ/R_Q in Figs. 3(b) and 3(c), respectively. In Fig. 3(c) we plot the robustness for different threshold error rates ε_\diamond^* .

Figure 3(b) shows that the imprecision is exponentially suppressed with the impedance of the oscillator for $Z_\phi/R_Q \geq 4$, and plateaus around $Z_\phi/R_Q = 10$. This exponential suppression is indicative of a protected gate. The plateau arises due to the finite charging energy ratio between the oscillator and the protected qubit, which we have set to $E_{C_\phi}/E_C = 100$. In Appendix D3 we show that the imprecision continues to decrease for larger E_{C_ϕ}/E_C . In the limit that $E_C \rightarrow 0$ then $E_J/E_C \rightarrow \infty$ and the superposition of the ground states of Eq. (3) are the ± 1 eigenstates of the logical operator \bar{Z}_θ . In this case, the system reduces to the ideal model Eq. (9), and the gate error continues to be exponentially suppressed at arbitrarily large Z_ϕ/R_Q .

Figure 3(c) shows that the robustness increases from zero at approximately $Z_\phi/R_Q = 4$ for multiple values of ε_\diamond^* . This indicates that the gate has appreciable tolerance to mistiming errors, providing further evidence that the gate is protected for $Z_\phi/R_Q \geq 4$. Notably, for each ε_\diamond^* , there exists an optimal value of Z_ϕ/R_Q that maximises the robustness of the gate. This arises from the fact that there is an optimal value of $\langle \hat{S}_{Z_\phi} \rangle$ to minimise the gate error for a given mistiming error (see Appendix D1). Since this expectation value is controlled by the impedance of

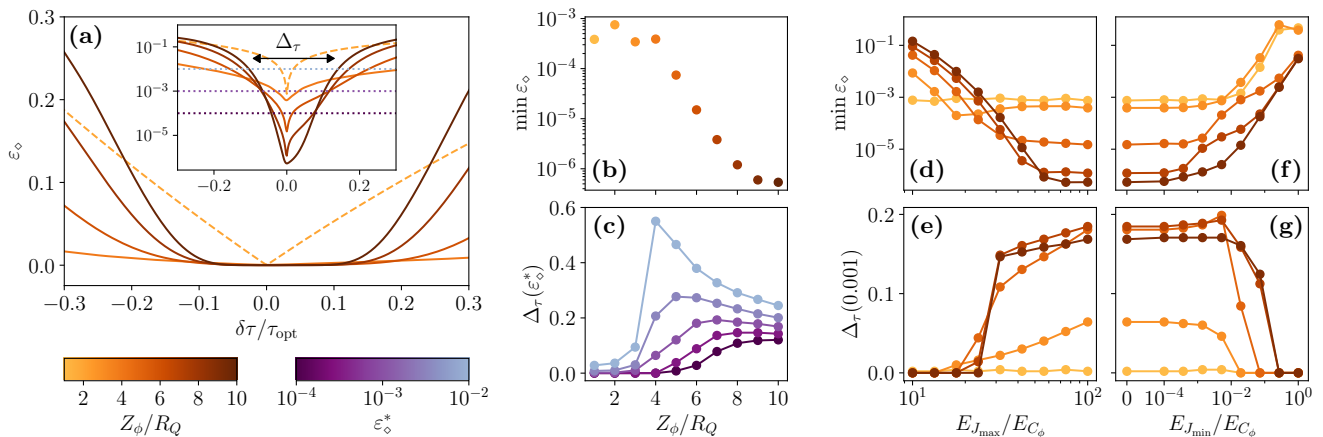


FIG. 3. Performance of a protected phase gate for an ideal qubit. (a) Gate error ε_\diamond (measured by the diamond norm deviation) as a function of deviations in the pulse wait-time $\delta\tau$, where $\delta\tau$ is given by Eq. (15), calculated for different values of the oscillator impedance Z_ϕ . Protected gates are marked in solid lines whereas the dashed line denotes an unprotected gate. Inset: identical data on a log-linear plot. Dotted lines correspond to threshold gate errors ε_\diamond^* for (c). (b) Gate imprecision (measured by the minimum gate error $\min \varepsilon_\diamond$) as a function of Z_ϕ . (c) Gate robustness (measured by the maximum range of $\delta\tau$ to remain below a threshold error rate ε_\diamond^*) as a function of Z_ϕ . (d) Imprecision, and (e) robustness as a function of the maximum Josephson coupling $E_{J_{\text{max}}}$. (f) Imprecision, and (g) robustness as a function of the minimum Josephson coupling $E_{J_{\text{min}}}$. For these simulations, $E_{C_\phi}/E_C = 100$, $E_J/E_{C_\phi} = 1$, and in panels (a) – (c), $E_{J_{\text{min}}} = 0$ and $E_{J_{\text{max}}}/E_{C_\phi} = 100$.

the oscillator [Eq. (10)], this leads to an optimal value of the impedance.

From these results, we conclude that a minimum oscillator impedance of $Z_\phi/R_Q \approx 4$ is required to obtain a protected gate. Note that while here we have considered the pulse wait-time τ as the basic metric to study the protection of the gate, in Appendix D 2 we show that the protected gate is similarly robust to deviations in the pulse ramp-time τ_J .

2. Dynamic range of the Josephson coupling

In the previous section we assumed that the tunable Josephson coupling has minimum and maximum values of $E_{J_{\text{min}}}/E_{C_\phi} = 0$ and $E_{J_{\text{max}}}/E_{C_\phi} = 100$. The most obvious candidate to achieve a tunable Josephson coupling is a SQUID, which consists of two Josephson junctions in a loop. The effective Josephson energy is tunable via the external magnetic flux threading the loop, ideally going to zero at half-flux. However, any asymmetry in the Josephson energies of the junctions leads to a non-zero effective Josephson energy at half-flux [3, 22]. Motivated by this limitation, here we quantify the dynamic range of the Josephson coupling $E_{J_{\text{max}}}/E_{J_{\text{min}}}$ required for a protected gate.

In Figs. 3(d) to 3(g) we plot the imprecision and robustness of the gate (as defined previously) as a function of both $E_{J_{\text{min}}}/E_{C_\phi}$ and $E_{J_{\text{max}}}/E_{C_\phi}$. Each curve corresponds to a different value of Z_ϕ/R_Q . For the robustness parameter, we choose a fixed threshold error rate of $\varepsilon_\diamond^* = 10^{-3}$. For the remainder of the paper, we choose this value when quantifying robustness.

Figure 3(d) shows that, for $Z_\phi/R_Q \geq 4$, the imprecision is exponentially suppressed with increasing $E_{J_{\text{max}}}/E_{C_\phi}$ and then plateaus. The point at which this plateau occurs increases with increasing Z_ϕ/R_Q . This means that increasing the maximum Josephson coupling beyond a particular value is only beneficial for a sufficiently large oscillator impedance. Figure 3(e) shows that, for $Z_\phi/R_Q \geq 4$, the gate possesses non-zero robustness for $E_{J_{\text{max}}}/E_{C_\phi} \geq 30$. We use this as a rough estimate of the minimum value of $E_{J_{\text{max}}}/E_{C_\phi}$ for a protected gate.

Figure 3(f) shows that, for $Z_\phi/R_Q \geq 4$, the imprecision is exponentially suppressed with decreasing $E_{J_{\text{min}}}/E_{C_\phi}$ and then plateaus. This means that decreasing the minimum Josephson coupling below a particular value is only beneficial for a sufficiently large oscillator impedance. Figure 3(g) shows that, for $Z_\phi/R_Q \geq 4$, the gate possesses non-zero robustness for values below $E_{J_{\text{min}}}/E_{C_\phi} \approx 0.005$, and for $Z_\phi/R_Q \geq 8$ this value increases to $E_{J_{\text{min}}}/E_{C_\phi} \approx 0.08$.

From these results, we find that a protected gate requires a tunable Josephson element with a minimum dynamic range of $E_{J_{\text{max}}}/E_{J_{\text{min}}} \approx 6 \times 10^3$ for $Z_\phi/R_Q \geq 4$. This requirement is slightly alleviated for a larger oscillator impedance; we require $E_{J_{\text{max}}}/E_{J_{\text{min}}} \approx 4 \times 10^2$ for $Z_\phi/R_Q \geq 8$. In Section IV B we discuss some ideas for how to achieve these large dynamic ranges.

These hardware requirements are obtained assuming an ideal protected qubit. In the following section, we describe our implementation of this protected gate for the $0-\pi$ qubit, and discuss how the hardware requirements of the circuit are changed.

III. PROTECTED GATE FOR THE $0-\pi$ QUBIT

In this section, we describe our proposal for a protected gate with the $0-\pi$ qubit. In Section III A we introduce the $0-\pi$ qubit, and explain the difficulties encountered when utilising an external oscillator as an ancilla for a protected phase gate. We propose a modified gate that instead utilises an internal harmonic mode. In Section III B we describe an effective model for the $0-\pi$ qubit that facilitates a numerical investigation of the hardware requirements of the gate, which we present in Section III C. Finally, in Section III D we briefly discuss the possibility of utilising another internal mode of the $0-\pi$ qubit for a protected gate.

A. Hamiltonian

The circuit for the $0-\pi$ qubit is shown in Fig. 1(a). It is a four-node circuit that consists of a pair of capacitors with capacitances $C_{1,2}$, a pair of inductors with inductances $L_{1,2}$, and a pair of Josephson junctions with Josephson energies $E_{J_{1,2}}$ and capacitances $C_{J_{1,2}}$. The Hamiltonian for this circuit is most conveniently expressed in terms of the modes θ , φ and ζ . These modes are quadrupole combinations of the original circuit nodes that are illustrated in Fig. 1(a). A fourth mode Σ does not appear in the Hamiltonian and is discarded. We derive the full Hamiltonian in Appendix A 1.

For symmetric circuit parameters between each pair of elements (i.e. $C_1 = C_2 = C$, $L_1 = L_2 = L$, etc.) the Hamiltonian for the $0-\pi$ qubit is $\hat{H} = \hat{H}_{\theta\varphi} + \hat{H}_{\zeta}$. The qubit is encoded in the two-mode Hamiltonian

$$\hat{H}_{\theta\varphi} = 4E_{C_\theta}\hat{n}_\theta^2 + 4E_{C_\varphi}\hat{n}_\varphi^2 + E_L\hat{\varphi}^2 - 2E_J \cos\hat{\theta} \cos\hat{\varphi}, \quad (16)$$

where $[\hat{\theta}, \hat{n}_\theta] = i$, $[\hat{\varphi}, \hat{n}_\varphi] = i$, $E_{C_\theta} = e^2/4(C + C_J)$, $E_{C_\varphi} = e^2/4C_J$, and $E_L = \phi_0^2/L$. The θ and φ modes are decoupled from the harmonic mode ζ :

$$\hat{H}_{\zeta} = 4E_{C_\zeta}\hat{n}_\zeta^2 + E_L\hat{\zeta}^2, \quad (17)$$

where $[\hat{\zeta}, \hat{n}_\zeta] = i$ and $E_{C_\zeta} = e^2/4C$. The two-mode Hamiltonian in Eq. (16) has an egg-carton-shaped potential with local minima at values $\theta + \varphi = 0 \pmod{2\pi}$ and local maxima at $\theta + \varphi = \pi \pmod{2\pi}$, as shown in Fig. 4(b). For

$$E_L, E_{C_\theta} \ll E_J, E_{C_\varphi}, \quad (18)$$

the circuit has a pair of nearly degenerate ground states that are simultaneously localised in θ ($E_J \gg E_{C_\theta}$) and delocalised in φ ($E_L \ll E_{C_\varphi}$) as shown in Fig. 4(a). In this parameter regime, the $0-\pi$ qubit is protected from both dephasing and relaxation [5].

The $0-\pi$ qubit is characterised by a charging energy ratio $E_{C_\theta}/E_{C_\varphi}$, a Josephson energy E_J/E_{C_φ} and an inductive energy E_L/E_{C_φ} . The protected regime corresponds

to the limit of $E_{C_\theta}/E_{C_\varphi} \rightarrow 0$ and $E_L/E_{C_\varphi} \rightarrow 0$ however, at non-zero values of $E_{C_\theta}/E_{C_\varphi}$ and E_L/E_{C_φ} , there exists an optimal value of E_J/E_{C_φ} that maximises the protection of the qubit [8]. We analyse this further in Appendix E 1.

We now consider a protected gate for the $0-\pi$ qubit. The most straightforward extension of the scheme discussed in Section II is to replace the ideal qubit with the $0-\pi$ circuit, resulting in the circuit shown in Fig. 1(b). The Hamiltonian is $\hat{H}(t) = \hat{H}_\phi + \hat{H}_{\theta\varphi} + \hat{H}_\zeta + \hat{H}_{\text{int}}^\phi(t)$, where the first three terms are given by Eqs. (6), (16) and (17), respectively, and the interaction term is [12]

$$\hat{H}_{\text{int}}^\phi(t) = -E_{J_{\text{int}}}(t) \cos(\hat{\phi} - \hat{\theta} + \hat{\zeta}), \quad (19)$$

as we show in Appendix A 2. The harmonic ζ mode is involved in the qubit-oscillator interaction. This is problematic for the protected gate. To see this, we assume the ζ mode is in the ground state of Eq. (17). This is a generous assumption considering that the mode is naturally low-frequency in the protected regime described by Eq. (18), and will have increasingly high thermal population. Nevertheless, the interaction term becomes

$$\hat{H}_{\text{int}}^\phi(t) = -E_{J_{\text{int}}}(t)e^{-\pi Z_\zeta/2R_Q} \cos(\hat{\phi} - \hat{\theta}), \quad (20)$$

where $Z_\zeta = \sqrt{L/4C}$ is the ζ -mode impedance. The effective Josephson coupling between the $0-\pi$ qubit and the oscillator is exponentially suppressed in the impedance of the ζ mode, which makes it very difficult to achieve the $E_{J_{\text{max}}}$ required for a protected gate.

To solve this issue, we propose a gate that utilises the ζ mode in place of an external oscillator. This is achieved by shunting the $0-\pi$ circuit with a tunable Josephson element as shown in Fig. 1(c). In Appendix A 3 we show that this leads to an interaction Hamiltonian of the form

$$\hat{H}_{\text{int}}^\zeta(t) = -E_{J_{\text{int}}}(t) \cos(\hat{\zeta} + \hat{\theta}). \quad (21)$$

Comparing this expression to Eq. (20) we can see that ζ takes the role of the ancilla, replacing the oscillator mode ϕ . Importantly, the qubit-ancilla interaction is no longer suppressed in the impedance of the ζ mode.

In the following sections, we investigate the circuit parameters required of the $0-\pi$ qubit to obtain a protected gate. We show that the interaction described by Eq. (21) is compatible with the protected regime of the $0-\pi$ qubit, while the interaction described by Eq. (20) is not. First, however, we describe a single-mode effective model for the two-mode Hamiltonian in Eq. (16). This allows us to reduce the overhead of our numerical simulations.

B. Effective model

We seek to reduce the time-dependent Hamiltonian $\hat{H}(t)$ from three modes to two modes. To achieve this, we approximate the Hamiltonian in Eq. (16) with a single-mode effective model. Single-mode models for the $0-\pi$

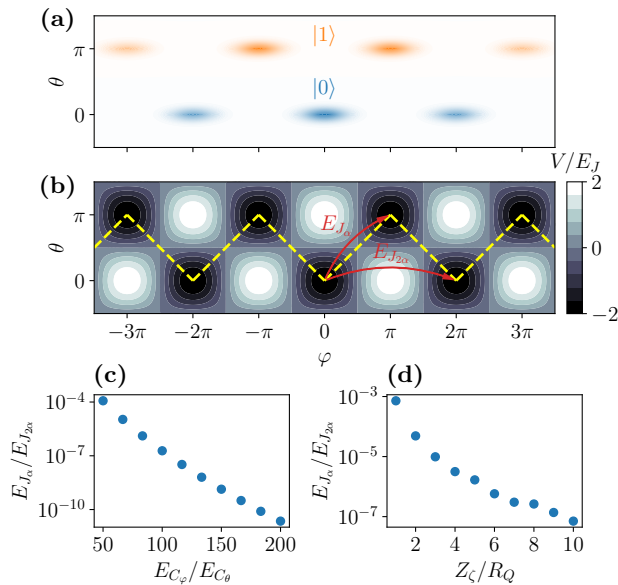


FIG. 4. Effective one-dimensional model for the $0-\pi$ qubit. (a) Wavefunctions for the $0-\pi$ qubit logical states. (b) Two-dimensional potential of the $0-\pi$ qubit, with the effective one-dimensional model (yellow) constructed from the local minima. The nearest-neighbour and next-nearest-neighbour tunnelling rates are E_{J_α} and $E_{J_{2\alpha}}$, respectively. (c) Ratio of the tunnelling rates $E_{J_\alpha}/E_{J_{2\alpha}}$ as a function of the $0-\pi$ qubit charging energy ratio E_{C_ϕ}/E_{C_θ} . (d) Ratio of the tunnelling rates as a function of the ζ -mode impedance Z_ζ , with E_J/E_{C_ϕ} given by the value that maximises the protection of the $0-\pi$ qubit at each impedance. Throughout all results, $E_{C_\phi}/E_{C_\theta} = 100$, and in panels (a) – (c), $E_J/E_{C_\phi} = 5$ and $Z_\zeta/R_Q = 10$.

qubit have been explored previously [11, 12, 23]. Here we use a tight-binding approximation in the discrete local minimum basis [24, 25]. This is valid in the parameter regime $2E_J > E_{C_\phi}, E_{C_\theta}, 2E_L$. A derivation of the effective model is provided in Appendix E 2, along with a discussion of an effective model when $2E_J$ is not the dominant circuit parameter.

We construct a one-dimensional system based on the local minima of the two-dimensional potential, as illustrated in Fig. 4(b). The effective Hamiltonian for this one-dimensional system is

$$\hat{H}_\alpha = 4E_{C_\alpha} \hat{n}_\alpha^2 - E_{J_\alpha} \cos \hat{\alpha} - E_{J_{2\alpha}} \cos 2\hat{\alpha}, \quad (22)$$

where $[\hat{\alpha}, \hat{n}_\alpha] = i$ and the effective energies are given by

$$E_{C_\alpha} = \frac{\pi^2 E_L}{4}, \quad (23)$$

$$E_{J_\alpha} \propto e^{-2(\sqrt{2}-1)\sqrt{2E_J/E_{C_\theta}} - \pi(\sqrt{2}-1)\sqrt{E_J/2E_{C_\phi}}}, \quad (24)$$

$$E_{J_{2\alpha}} \propto e^{-4\sqrt{E_J/E_{C_\phi}}}. \quad (25)$$

This effective Hamiltonian is similar to Eq. (3), with the addition of a term $\cos \hat{\alpha}$ that splits the near-degeneracy

of the two qubit states. In the language of the logical operators for the GKP code, this additional term acts like the Z -type logical operator $\bar{Z}_\alpha = e^{i\hat{\alpha}}$.

The expressions for the effective charging energy E_{C_α} and tunnelling energies E_{J_α} and $E_{J_{2\alpha}}$ are derived from the tight-binding model and depend on the circuit parameters of the $0-\pi$ qubit. The charging energy is proportional to the inductive energy E_L of the $0-\pi$ qubit because flux-like variables get mapped to charge-like variables in the effective model. The exponential scalings for the tunnelling rates are calculated from the classical action over the tunnelling paths. Their prefactors, which are polynomials in the circuit parameters may be found using WKB or instanton methods [14, 26].

First we consider $E_{J_{2\alpha}}$, which describes next-nearest-neighbour tunnelling in the effective model. Since this tunnelling occurs solely in the φ direction and there is a large separation in the charging energies ($E_{C_\phi} \gg E_{C_\theta}$), the qubit wavefunctions are confined in the θ direction. Thus, $E_{J_{2\alpha}}$ may be approximated using the one-dimensional tunnelling rate for a transmon [3]; see Eq. (E12) for its full expression. We find this to be a good approximation for $E_{C_\phi}/E_{C_\theta} \geq 50$.

Now we consider E_{J_α} , the nearest-neighbour tunnelling rate. Unlike the next-nearest-neighbour tunnelling, the nearest-neighbour tunnelling occurs through a non-trivial path in θ and φ , which are computed in Appendix E 2 c. Due to the component of the tunnelling path in the θ direction, its rate is exponentially suppressed in $\sqrt{E_{C_\phi}/E_{C_\theta}}$ relative to $E_{J_{2\alpha}}$. Therefore, E_{J_α} is suppressed relative to $E_{J_{2\alpha}}$ for the protected regime of the $0-\pi$ qubit. For simplicity, we calculate the prefactor for E_{J_α} numerically by fitting Eq. (22) to Eq. (16), with E_{C_α} and $E_{J_{2\alpha}}$ fixed.

In Fig. 4(c) we plot the ratio of the tunnelling energies as a function of E_{C_ϕ}/E_{C_θ} . We see that $E_{J_\alpha}/E_{J_{2\alpha}}$ is suppressed, as expected. Furthermore, in Fig. 4(d) we show that the nearest-neighbour tunnelling rate is also suppressed in the impedance of the internal ζ mode, for $E_{C_\phi}/E_{C_\theta} = 100$. Thus, a higher ζ -mode impedance leads to a more protected $0-\pi$ qubit. This directly conflicts with the suppression of the effective qubit-oscillator coupling in Eq. (20), but not the interaction term when using the ζ mode in Eq. (21).

Finally, we can rewrite the interaction Hamiltonians in Eqs. (20) and (21) in terms of the effective mode α by letting $\hat{\theta} = \pi\hat{n}_\alpha$,

$$\hat{H}_{\text{int}}^\phi(t) = -E_{J_{\text{int}}}(t) e^{-\pi Z_\zeta/2R_Q} \cos(\hat{\phi} - \pi\hat{n}_\alpha), \quad (26)$$

$$\hat{H}_{\text{int}}^\zeta(t) = -E_{J_{\text{int}}}(t) \cos(\hat{\zeta} - \pi\hat{n}_\alpha). \quad (27)$$

In the following section, we use this effective model to simulate a protected gate for the $0-\pi$ qubit.

C. Numerical simulations

Here we simulate the dynamics of a protected phase gate for the $0-\pi$ qubit. We contrast two models: one that uses an external oscillator mode ϕ , and our approach that uses the ζ mode of the $0-\pi$ circuit. We simulate the Hamiltonian $\hat{H}(t) = \hat{H}_\phi + \hat{H}_\alpha + \hat{H}_{\text{int}}(t)$, where the first two terms are given by Eqs. (6) and (22), and the final term is given by either Eq. (26) or Eq. (27), depending on the model of interest. Our numerical approach is similar to the simulations in Section II C, though there are some slight differences that we discuss in Appendix B.

In Figs. 5(a) and 5(b) we plot the imprecision and robustness of a gate that uses an external oscillator with $Z_\phi/R_Q = 10$. In Figs. 5(c) and 5(d) we plot the same metrics for a gate that uses the internal ζ mode. In both cases, the metrics are plotted as a function of the ζ -mode impedance Z_ζ/R_Q . We fix the charging energy ratios to $E_{C_\phi}/E_{C_\theta} = E_{C_\varphi}/E_{C_\theta} = 100$ and for each value of Z_ζ/R_Q , we set E_J/E_{C_φ} such that the $0-\pi$ qubit protection is maximised. We have also set $E_{J_{\text{min}}} = 0$, while the maximum Josephson coupling is set to a critical value denoted $E_{J_{\text{max}}}^*$. This is the minimum value of $E_{J_{\text{max}}}$ required to obtain a protected gate with robustness $\Delta_\tau(0.001) > 0$. If that is not possible, then $E_{J_{\text{max}}}^*$ is simply the value that minimises the imprecision of the gate. This is intended to reflect the hardware requirements of the tunable Josephson element for a protected gate, as we vary Z_ζ/R_Q .

Figure 5 shows that both versions of the gate require $Z_\zeta/R_Q \geq 5$ to acquire appreciable robustness. This is due to the suppression of the symmetry-breaking $\cos \alpha$ term in Eq. (22) that occurs for large Z_ζ , which may be seen in Fig. 4(d). A larger ζ -mode impedance is therefore preferable, as it recovers the ideal qubit Hamiltonian in Eq. (3). However, in this protected regime the value of $E_{J_{\text{max}}}^*$ required to achieve a robust gate becomes very large for a gate that uses the external oscillator, reaching values of $E_{J_{\text{max}}}^*/E_{C_\phi} > 10^8$ for $Z_\zeta/R_Q = 10$. This aligns with the exponential suppression of the Josephson coupling in Eq. (26). By contrast, a gate that uses the ζ mode has $E_{J_{\text{max}}}^*/E_{C_\zeta} \leq 100$ for all Z_ζ . For comparison, in Section II we found that $E_{J_{\text{max}}}^*/E_{C_\phi} \approx 30$ for the case of an ideal qubit.

Performing a protected gate with the $0-\pi$ qubit using an external oscillator is very challenging due to the two competing effects of increasing the ζ -mode impedance. On the one hand, a large ζ -mode impedance coincides with the protected regime of the $0-\pi$ qubit. On the other hand, it exponentially suppresses the qubit-oscillator interaction. Using the ζ mode in place of the external oscillator solves this issue because the interaction strength is no longer suppressed with the ζ -mode impedance.

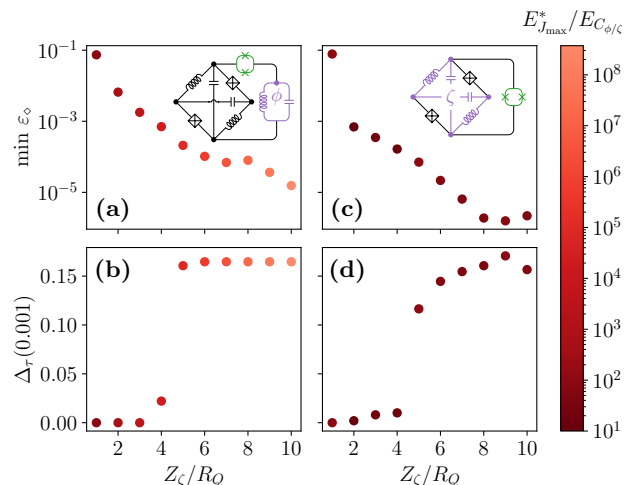


FIG. 5. Comparison of two different implementations of a protected phase gate for the $0-\pi$ qubit. (a) Imprecision and (b) robustness of a gate that uses an external oscillator ϕ as a function of the ζ -mode impedance Z_ζ of the $0-\pi$ qubit. We have set $Z_\phi/R_Q = 10$. (c) Imprecision and (d) robustness of a gate that uses the ζ mode of the $0-\pi$ qubit, instead of an external oscillator. For each data point, a different value of $E_{J_{\text{max}}}$ is chosen, denoted $E_{J_{\text{max}}}^*$. This is defined to be the minimal value of $E_{J_{\text{max}}}$ for which $\Delta_\tau(0.001) > 0$, if it exists, or the value that maximises the precision, otherwise. Its units are in E_{C_ϕ} for the left column and E_{C_ζ} for the right column. Throughout all simulations, $E_{C_\varphi}/E_{C_\theta} = 100$ and $E_{J_{\text{min}}} = 0$. The circuit diagrams corresponding to each implementation of the gate are shown as insets for each column.

D. φ mode

An alternative to using the internal ζ mode for a protected gate with the $0-\pi$ qubit is to use the internal φ mode. This could be achieved by replacing the static Josephson junctions in the $0-\pi$ qubit with tunable Josephson elements, facilitating a tunable coupling between the θ and φ modes.

In Appendix D 4, we simulate this version of the gate but find that a protected gate is not feasible for near-term experimental charging energy ratios. The underlying reason is that tuning the coupling between the θ and φ modes of the qubit to perform the gate simultaneously tunes the barrier height in both the φ and θ directions of the qubit. In Section II C we showed a requirement of $E_{J_{\text{min}}} < E_{C_\phi}$ to obtain a protected gate. When using the internal φ mode, this translates to $E_{J_{\text{min}}} < E_{C_\varphi}$. However, we find that this small value leads to unwanted tunnelling between the two logical states throughout the gate. At larger values of $E_{J_{\text{min}}}$, this unwanted tunnelling is reduced, but the protection of the gate is compromised due to the smaller dynamic range.

The tunnelling between the two qubit states could be reduced whilst maintaining a sufficiently small $E_{J_{\text{min}}}$ for

a protected gate by increasing the charging energy ratio $E_{C_\varphi}/E_{C_\theta}$. However, given that increasing $E_{C_\varphi}/E_{C_\theta}$ is experimentally challenging (which we discuss in Section IV C), the ζ mode is likely to be an easier path to a protected gate.

IV. HARDWARE CONSTRAINTS

In this section we delve further into the hardware constraints for implementing a protected gate. In Section IV A we analyse the impacts of circuit disorder in the $0-\pi$ qubit on the performance of the gate, and in Section IV B we consider the hardware requirements for the tunable Josephson element to achieve a protected gate. Sections IV C and IV D examine the constraints on the charging energy ratio and ancilla impedance for a protected gate, respectively. Finally, in Sections IV E and IV F, we discuss the role of cooling and photon loss, respectively.

A. Circuit disorder

So far we have ignored the circuit disorder of the $0-\pi$ qubit; in Eqs. (16) and (17) we assume each pair of circuit components in the $0-\pi$ qubit are identical. In practice, this symmetry will be broken due to limitations of device fabrication. In Appendix A 1, we derive the Hamiltonian for the $0-\pi$ circuit in the presence of disorder. Here we analyse the impact of disorder on our proposed gate.

Inductive asymmetry leads to the flux-flux interaction term $\delta E_L \hat{\varphi} \hat{\zeta}$, where $\delta E_L = \phi_0^2/L_1 - \phi_0^2/L_2$. To simulate this, we add the term $\delta E_L \pi \hat{n}_\alpha \hat{\zeta}$ to Eq. (27) because $\hat{\varphi} \rightarrow \pi \hat{n}_\alpha$ in the effective model. In Figs. 6(a) and 6(b) we plot the gate error as a function of Z_ζ for different inductive asymmetries. We find that it is almost entirely insensitive to an inductive asymmetry of $\delta E_L/2E_L = 5\%$, and begins to lose its robustness at $\delta E_L/2E_L = 25\%$. The robustness of the gate to inductive asymmetries may be attributed to the $0-\pi$ qubit's insensitivity to flux noise.

Josephson asymmetry leads to a nonlinear interaction term $\delta E_J \sin \hat{\theta} \sin \hat{\varphi}$, where $\delta E_J = E_{J_1} - E_{J_2}$. This flattens the egg-carton-shaped potential of the $0-\pi$ qubit, and leads to an increase in $E_{J_\alpha}/E_{J_{2\alpha}}$ for the effective model in Eq. (22). In Figs. 6(c) and 6(d) we plot the gate error as a function of Z_ζ for different Josephson asymmetries. We find that the gate is almost entirely insensitive to asymmetries up to $\delta E_J/2E_J = 50\%$, and only begins to lose its robustness once $\delta E_J/2E_J = 70\%$. This is due to the fact that the location of the minima in the potential are unaffected by the $\sin \hat{\theta} \sin \hat{\varphi}$ term and tunnelling between the two qubit states remains exponentially suppressed in E_J/E_{C_θ} so long as the reduced barrier height remains larger than E_{C_θ} .

Capacitive asymmetry leads to charge-charge coupling between the θ , φ and ζ modes. Here we explain that these effects are less significant than the asymmetries in

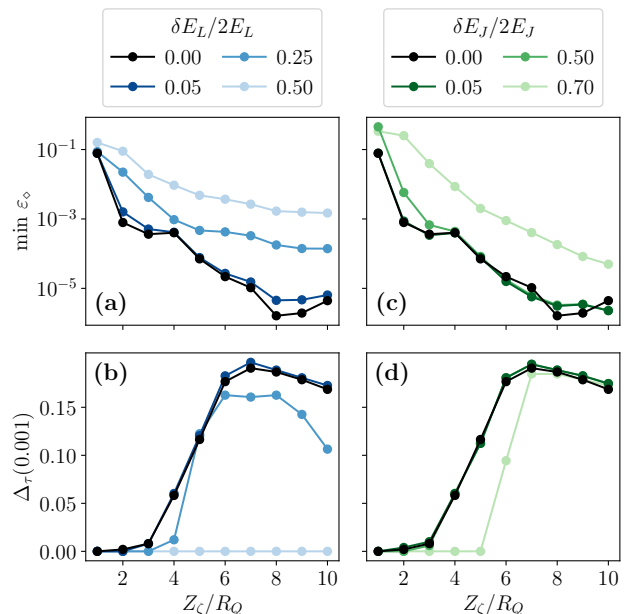


FIG. 6. Impact of circuit disorder on the protected phase gate for the $0-\pi$ qubit that uses the internal ζ mode. (a) Imprecision and (b) robustness as a function of the ζ -mode impedance Z_ζ , for different asymmetries in the inductors δE_L . (c) Imprecision and (d) robustness as a function of the ζ -mode impedance Z_ζ , for different asymmetries in the Josephson junctions δE_J . Throughout all simulations, the charging energy ratio is fixed to $E_{C_\varphi}/E_{C_\theta} = 100$ and the minimum and maximum Josephson couplings are $E_{J_{\min}} = 0$ and $E_{J_{\max}}/E_{C_\zeta} = 100$.

the inductors and Josephson junctions. Additional terms that arise due to capacitive disorder may be obtained by substituting $\hat{n}_\theta \rightarrow \hat{n}_\theta - r_\varphi \hat{n}_\varphi - r_\zeta \hat{n}_\zeta$ into Eq. (16), where $r_\zeta = (C_1 - C_2)/(C_1 + C_2)$ and $r_\varphi = (C_{J_1} - C_{J_2})/(C_{J_1} + C_{J_2})$ quantify the relative disorder in the capacitances. We start by considering the effects of this disorder that are linear in the parameters r_ζ and r_φ .

Asymmetry in the junction capacitances leads to an interaction term $r_\varphi E_{C_\theta} \hat{n}_\theta \hat{n}_\varphi$. It is possible to repeat our numerical fitting of the effective one-dimensional model to Eq. (16) with this additional contribution to the Hamiltonian. However, we find that this term has a negligible impact on the spectrum of the $0-\pi$ qubit up to asymmetries of $|r_\varphi| = 1$. This is consistent with the findings of Ref. [8].

Asymmetry in the capacitors leads to an interaction term $r_\zeta E_{C_\theta} \hat{n}_\theta \hat{n}_\zeta$. It is also possible to capture the effect of this noise in the tight-binding model of the $0-\pi$ qubit. The tight-binding eigenstates $|n_\alpha\rangle$ are approximately harmonic oscillator ground states localised at the minima of the potential of the Hamiltonian in Eq. (16). This makes it possible to approximate the matrix elements $\langle n'_\alpha | \hat{n}_\theta | n_\alpha \rangle$ for these states. When $n_\alpha \neq n'_\alpha$ these matrix elements couple distinct wells of the cosine poten-

tial and are exponentially suppressed since these states are highly localised. On the other hand, the expectation values $\langle n_\alpha | \hat{n}_\theta | n_\alpha \rangle$ vanish because of the $\hat{\theta} \rightarrow -\hat{\theta}$ symmetry of the potential. Note that this symmetry persists for all values of E_L so that even in analysing corrections to the harmonic oscillator ground state, these mean values remain equal to zero. The perturbative correction to the tight-binding model is of the form

$$r_\zeta E_{C_\theta} \hat{n}_\zeta \sum_{n_\alpha, n'_\alpha \in \mathbb{Z}} \langle n'_\alpha | \hat{n}_\theta | n_\alpha \rangle |n'_\alpha\rangle \langle n_\alpha|, \quad (28)$$

and is therefore expected to be negligible compared to the inductive and Josephson disorder. This is consistent with the fact that transmons are insensitive to offset charge and the $0-\pi$ qubit is inheriting this insensitivity through the θ mode.

At the next order in r there are three additional contributions to the Hamiltonian. The first two of these, $r_\varphi^2 E_{C_\theta} \hat{n}_\varphi^2$ and $r_\zeta^2 E_{C_\theta} \hat{n}_\zeta^2$, can be absorbed as small adjustments to the charging energy of the φ and ζ modes and we do not discuss them further. The final correction is $r_\zeta r_\varphi E_{C_\theta} \hat{n}_\varphi \hat{n}_\zeta$ and this can be analysed in the same way as the $\hat{n}_\theta \hat{n}_\zeta$ term. However, here the inductive potential in Eq. (16) does break the $\hat{\varphi} \rightarrow -\hat{\varphi}$ symmetry leading to non-zero mean values $\langle n_\alpha | \hat{n}_\varphi | n_\alpha \rangle$. Nevertheless, this contribution is second order in r and will be suppressed by some power of $E_L/\sqrt{E_J E_{C_\varphi}}$. Therefore, we do not pursue a quantitative discussion of this contribution, which will be smaller than the effects of the inductive and Josephson junction asymmetries that we analysed above.

B. Tunable Josephson element

In Section II C we found that the tunable Josephson element requires a dynamic range of at least two orders of magnitude to obtain a protected gate, with larger dynamic ranges required at lower ancilla impedances. Whilst two orders of magnitude may be achievable using a SQUID, where asymmetries in the Josephson energies of the junctions are usually at the percent level [22], anything larger will be experimentally challenging. Voltage-tunable Josephson junctions [27, 28] might provide an alternative as they have no such symmetry requirements. Instead, the dynamic range will be dictated by the sensitivity of the device to voltage fluctuations of the electrostatic gate that tunes the Josephson energy.

Another possible route to achieve a tunable Josephson element with a larger dynamic range is to use a SQUID with multiple inductive loops. Similar devices have been used in Refs. [29–31]. In Appendix A 6 b we calculate the effective Josephson energy of a multi-loop SQUID. We find that the dynamic range of the effective Josephson energy scales with the noise on the external magnetic fluxes, rather than the asymmetry in the Josephson energies of the junctions. Since typical flux noise amplitudes

are on the order of $\phi_0 \times 10^{-6}$ [32, 33], this suggests that tunable Josephson elements with a larger dynamic range could be achieved for a protected gate.

We have also treated the tunable Josephson element as a purely inductive element. However, in reality it will have some non-zero capacitance C_{int} . This reduces the effective charging energy ratio between the oscillator mode and qubit mode, and introduces undesired charge-charge coupling between the two modes. In Appendix A 6 a we consider these effects for the case of the ideal qubit coupled to an oscillator. Here, we find that the gate remains unaffected so long as $C_{\text{int}}/C_\phi < 0.1$.

A smaller C_{int} also implies a smaller $E_{J_{\text{max}}}$ for a fixed plasma frequency $\omega_p = \sqrt{8E_{J_{\text{max}}}E_{C_{\text{int}}}}/\hbar$. This makes it very challenging to achieve the large values of $E_{J_{\text{max}}}^*/E_{C_\phi}$ required for the protected gate with the $0-\pi$ qubit using the external oscillator whilst maintaining a small ratio of C_{int}/C_ϕ . For example, in Section III C we found a minimum ζ -mode impedance of $Z_\zeta/R_Q = 5$ at an oscillator impedance of $Z_\phi/R_Q = 10$ was necessary to achieve a gate with appreciable robustness. At this ζ -mode impedance, a coupling strength of $E_{J_{\text{max}}}/E_{C_\phi} > 8 \times 10^4$ is required. Assuming the oscillator impedance may be obtained with $E_{C_\phi}/h = 1$ GHz and $E_{L_\phi}/h = 2$ MHz, the maximum Josephson coupling required for the protected gate would be greater than $E_{J_{\text{max}}}/h = 80$ THz. With a plasma frequency of the tunable Josephson element of $\omega_p/2\pi = 40$ GHz, this implies that $C_{\text{int}}/C_\phi > 100$, which is well above the requirement for the gate to remain protected.

When using either of the internal modes of the $0-\pi$ qubit instead of the external oscillator, the capacitance of the tunable Josephson element will simply add to the capacitance of the ζ or φ mode. In this way, so long as the capacitance in the device remains approximately symmetric, the capacitance of the tunable Josephson element has no effect on the performance of the gate, regardless of its value. This is another advantage of utilising the internal modes of the $0-\pi$ qubit to perform a gate.

C. Charging energy ratio

In all of the above numerical results we have fixed the largest ratio of the physical capacitances in the system to two orders of magnitude. Ideally this quantity should be made as large as possible, but larger values pose an experimental challenge. In the case of the $0-\pi$ qubit, a large $E_{C_\varphi}/E_{C_\theta}$ is achieved by minimising the capacitance of the Josephson junctions C_J whilst simultaneously maximising the capacitance of the capacitors C . In Ref. [9], a charging energy ratio of $E_{C_\varphi}/E_{C_\theta} \approx 12$ was achieved for the soft $0-\pi$ qubit. This relatively small separation in charging energies is the reason for the partial protection of this device. Methods to increase this ratio include different capacitor geometries [10] as well as using a silicon-insulator substrate for the device to reduce the effect of stray capacitances that decrease E_{C_φ} [11]. We choose

to focus on a ratio of two orders of magnitude as a representative near-term value, but in Appendix D 3 b we investigate the impact of different charging energy ratios on the performance of a protected gate. Here we find that a protected gate can be recovered with smaller charging energy ratios, but that it requires a larger impedance of the ζ mode.

D. Ancilla impedance

The results in Section II C showed that an oscillator impedance of at least $Z_\phi/R_Q = 4$ was necessary to obtain a protected gate for an ideal qubit coupled to an oscillator. This value is achievable with current superinductors, where impedances up to $Z_\phi/R_Q = 4.8$ have been demonstrated using chains of Josephson junctions [34] or geometric coils [35].

In Section III C we found that a ζ -mode impedance of $Z_\zeta/R_Q \geq 5$ was necessary to obtain a protected gate. These results assumed a charging energy ratio of $E_{C_\varphi}/E_{C_\theta} = 100$ in the $0-\pi$ qubit, meaning that the φ -mode impedance $Z_\varphi = \sqrt{L/4C_J}$ is larger than Z_ζ by a factor of 10. Therefore, the ζ -mode impedance requirement of $Z_\zeta/R_Q = 5$ translates to a φ -mode impedance (which is the largest impedance in the device) of $Z_\varphi/R_Q = 50$. In Appendix D 3 b we simulate the gate at lower charging energy ratios, but find that this increases the required ζ -mode impedance for the gate to be protected such that $Z_\varphi/R_Q = 50$ remains the lowest φ -mode impedance to achieve protection. This is an order of magnitude larger than what has been achieved with current superinductors, suggesting that further improvements in superinductors are necessary to obtain a protected gate with the $0-\pi$ qubit.

E. Cooling

As mentioned in Section II, the ancillary mode must be cooled between performing gates in order to extract entropy from the circuit. For an external oscillator, this is possible using well-established techniques for oscillator cooling [22]. In the case of using one of the internal modes as an ancilla, this mode may be cooled using the scheme provided in Ref. [12], which involves capacitively coupling the $0-\pi$ qubit to a lossy oscillator, and activating sideband transitions between the ancillary mode and the oscillator. We note that this cooling oscillator does not require a superinductor, in contrast to the ancillary oscillator required to perform a protected gate. However, it does require a tunable inductance in order to modulate its frequency and coupling strength. Given that it is likely to be necessary to cool the ζ mode of the $0-\pi$ qubit to prevent coupling to the φ mode during idling [12, 36], implementation of this cooling mechanism is likely a requirement regardless of whether or not an internal mode is used to perform the gate.

F. Photon loss

Throughout this paper we have used the gate's robustness to pulse mistiming as a proxy for its protection. Another useful metric would be the error of the gate in the presence of photon loss in the ancillary mode. However, simulating this presents a theoretical and/or computational challenge due to the dynamic non-linearity present in the interaction Hamiltonian.

For example, let us consider the case of the ideal qubit coupled to an oscillator via Eq. (7). In the regime where $E_{J_{\text{int}}}(t) \ll \sqrt{8E_{L_\phi}E_{C_\phi}}$, photon loss may be efficiently simulated using a Lindblad master equation with collapse operators given by the annihilation operators for the oscillator mode ϕ . Likewise, photon loss may be efficiently simulated in the opposite regime, $E_{J_{\text{int}}}(t) \gg \sqrt{8E_{L_\phi}E_{C_\phi}}$, by using collapse operators that transition between tight-binding eigenstates [37].

However, in the intermediate regime between these extremes, the situation is more complicated. Unlike qubit gates involving resonant driving, the Hamiltonian changes during the gate in ways that cannot be described perturbatively. This means that there are no consistent collapse operators for the full time-dependent gate simulation as $E_{J_{\text{int}}}(t)$ crosses through the aforementioned regimes. For these general time-dependent systems, the master equation is much more computationally expensive since it involves diagonalising the system at each time step. Moreover, the Markov approximation that leads to a master equation requires that the energy levels in the Hamiltonian are well-separated compared to the photon-loss rate. This requirement may not hold for intermediate values of $E_{J_{\text{int}}}(t)$.

Nevertheless, we expect the gate to be robust to photon loss for the following reasons. In the large $E_{J_{\text{int}}}(t)$ regime of the gate, the ancillary mode is encoded into the GKP code, which is particularly resilient to photon loss [38]. Therefore, photon loss errors that occur during this time should be correctable upon cooling the ancillary mode. When this mode is not encoded in the GKP code during the small $E_{J_{\text{int}}}(t)$ regime of the pulse, then photon loss benefits the gate by cooling the ancillary mode.

Finally, we note that our pulses are not optimised for pulse duration, and that pulse optimisation techniques such as DRAG [39] may yield faster gate times with smaller errors.

V. BEYOND THE PHASE GATE

In this paper, we have focused on the implementation of a protected single-qubit phase gate. In Refs. [6] and [7], an extension of the single-qubit phase gate to a protected two-qubit phase gate is outlined. Universal fault-tolerance is then obtained by supplementing these protected gates with unprotected single-qubit rotations and repeated noisy measurements in the logical X and Z bases. In Section V A we outline a way to use the internal

modes of two coupled $0-\pi$ qubits to perform a protected two-qubit gate, and in Section VB we briefly discuss an extension of the protected S -gate to a T -gate.

A. Two-qubit gate

The two-qubit gate proposed in Refs. [6, 7] involves connecting two $0-\pi$ qubits in series and shunting the entire circuit with a high-impedance oscillator. This is intended to implement an interaction term

$$\hat{H}_{\text{int}} = -E_{J_{\text{int}}}(t) \cos(\hat{\theta}_a + \hat{\theta}_b - \hat{\phi}), \quad (29)$$

where θ_a and θ_b label two protected qubit modes, and ϕ denotes the oscillator mode. This term means that a phase of $\pi/2$ is acquired in the oscillator when the logical states of the two qubits are $|01\rangle$ or $|10\rangle$ and no phase is accrued when the qubit states are in $|00\rangle$ or $|11\rangle$, enacting the logical unitary operation $\exp(-i\frac{\pi}{4}\hat{Z} \otimes \hat{Z})$. Similarly to the single-qubit case, we find that the envisaged circuit gives rise to coupling to internal ζ modes of both qubits, making the protected gate challenging to achieve due to the exponential suppression of the interaction strength.

In Appendix A5, we show that it is possible to utilise these ζ modes to perform this gate by instead shunting the two qubits with a tunable Josephson element. For this gate to work, the two qubits must be brought into resonance with each other to utilise the symmetric superposition of the two internal ζ modes in place of the external oscillator. This suggests the need to make $0-\pi$ qubits tunable when scaling to a multi-qubit system based on $0-\pi$ qubits.

B. Magic gate

The protected S -gate relies on the fact that the quadratic potential enacts an encoded S -gate on the GKP code. In Refs. [13, 40] higher-order polynomial potentials are shown to enact a T -gate on GKP codewords. However, the resulting gate is deemed to be non fault-tolerant due to the fact that higher-order polynomials distort GKP codewords in an uncorrectable way. In Appendix D5, we investigate replacing the quadratic potential in Eq. (6) with a quartic potential in order to realise a potentially protected T -gate. A quartic potential may be generated using a superconducting nonlinear asymmetric inductive element (SNAIL) oscillator [41–43] rather than a linear oscillator. We find that a T -gate with errors $< 10^{-3}$ may be obtained, but that the gate is less robust than the equivalent S -gate. This is a consequence of the encoded T -gate being non fault-tolerant for the GKP code. Nevertheless, this provides a way of performing a T -gate that does not explicitly break the protection of the qubit. We believe there is much room for exploring other protected gates based on different potentials or different bosonic codes.

VI. CONCLUSIONS

In conclusion, we have proposed and analysed a protected phase gate for the $0-\pi$ qubit that is compatible with the protected regime of the qubit. Our approach is based on the BKP gate proposed in Refs. [6, 7], which utilises an external oscillator. Through numerical simulations, facilitated by a one-dimensional model for the $0-\pi$ qubit, we compared the performance of the gate using an external oscillator to the gate using the internal ζ mode. The results revealed that a ζ -mode impedance of $Z_\zeta/R_Q = 5$ is necessary for a protected gate in both cases, but that infeasibly large Josephson energies would be required to recover this protection when using an external oscillator.

Whilst our scheme substantially reduces the hardware requirements for the protected gate relative to BKP's original proposal, we summarise three of the main experimental challenges. First, a large dynamic range of the tunable Josephson element is required; we found a requirement of greater than two orders of magnitude. This may be challenging with standard SQUIDS and necessitate a different coupling element, such as a SQUID with multiple inductive loops. Second, a large charging energy ratio of $E_{C_\varphi}/E_{C_\theta} = 100$ is necessary. Whilst the soft $0-\pi$ qubit only achieved a charging energy ratio of $E_{C_\varphi}/E_{C_\theta} \approx 12$, there exist several approaches to substantially increase this value. Third, owing to the large charging energy ratio, the ζ -mode impedance requirement of $Z_\zeta/R_Q = 5$ translates to a φ -mode impedance of $Z_\varphi/R_Q = 50$. This is roughly an order of magnitude larger than what has been achieved with current superconductors. Increasing circuit impedance is an active experimental effort since this is a requirement of many types of superconducting qubits [14, 34, 44–46]. It is therefore reasonable to assume that this level of impedance is in line with the fabrication advancements required to make a protected superconducting qubit.

Although improvements in current fabrication techniques are required to achieve a protected gate with the $0-\pi$ qubit, our results also show that unprotected gates with gate errors $< 10^{-3}$ are possible with current parameters. Given the inherent challenge in manipulating protected qubits, our results are valuable in providing a number of viable approaches to perform gates with these qubits both in the near and long term.

Finally, we gave two possible extensions of the protected single-qubit phase gate to a protected magic and two-qubit gate. We believe there are many opportunities for exploring other types of protected gates based on different bosonic codes, and tailoring protected gates to other types of protected qubits.

ACKNOWLEDGEMENTS

We would like to thank Joshua Combes, Xanthe Croot, Farid Hassani and Mackenzie Shaw for insightful discus-

sions. We acknowledge support from the Australian Research Council via the Centre of Excellence in Engineered Quantum Systems (CE170100009), and the US Army Research Office (W911NF-23-10092). X. C. K. is supported by an Australian Government Research Training Program (RTP) Scholarship. X. C. K. acknowledges access to the University of Sydney's high performance computing facility, Artemis, for obtaining numerical results. F. T. is supported by the Sydney Quantum Academy. We acknowledge the traditional owners of the land on which this work was undertaken at the University of Sydney, the Gadigal people of the Eora Nation.

Appendix A: Circuit quantisation

In this appendix we provide details for the quantisation of circuits discussed in the main text. After introducing the methodology used, we derive Hamiltonians for the following circuits: a $0-\pi$ qubit in Appendix A 1, a $0-\pi$ qubit Josephson-coupled to an oscillator in Appendix A 2, modified $0-\pi$ qubits Josephson-coupled to their internal modes in Appendices A 3 and A 4, and two $0-\pi$ qubits coupled in series in Appendix A 5. In Appendix A 6 we use the established quantisation procedure to analyse the effects of capacitance and extend the dynamic range of the tunable Josephson element.

We now provide an overview of our generic circuit quantisation procedure. Our procedure closely follows Refs. [47, 48].

The classical Lagrangian of a circuit is

$$\mathcal{L} = T - V, \quad (\text{A1})$$

where T is the kinetic energy associated with capacitors and V is the potential energy associated with inductors and Josephson junctions. Each circuit element has a corresponding branch flux variable:

$$\Phi_k(t) = \int_{-\infty}^t d\tau V_k(\tau), \quad (\text{A2})$$

where V_k is the voltage across the branch k . Faraday's law and fluxoid quantisation leads to a constraint on branch fluxes that form a loop ℓ :

$$\sum_{k \in \ell} \Phi_k = \phi_{\text{ext}}, \quad (\text{A3})$$

where ϕ_{ext} is the external flux threading the loop ℓ . This constraint provides a relationship between branch flux variables Φ_k and node flux variables ϕ_n . Specifically,

$$\Phi_k = \phi_n - \phi_{n'} + \phi_{\text{ext},k}, \quad (\text{A4})$$

where $\phi_{\text{ext},k}$ is the contribution of the external flux ϕ_{ext} to the branch k . Eqs. (A3) and (A4) may be written in a more compact vector form:

$$\mathbf{G}\Phi = \phi_{\text{ext}}, \quad (\text{A5})$$

$$\Phi = \mathbf{A}\phi + \mathbf{B}\phi_{\text{ext}}. \quad (\text{A6})$$

We define three column vectors: Φ contains the k branch fluxes, ϕ contains the n node fluxes, and ϕ_{ext} contains the l external fluxes. The $l \times k$ matrix \mathbf{G} ensures that the sum of branch fluxes in a loop equals the external flux threading that loop. The $k \times n$ matrix \mathbf{A} relates each branch flux to a phase difference between two node fluxes, which is determined by the choice of spanning tree. The $k \times l$ matrix \mathbf{B} assigns external fluxes to the closure branches of the circuit.

The kinetic energy of a circuit is given by

$$T(\dot{\Phi}) = \frac{1}{2} \dot{\Phi}^T \mathbf{C} \dot{\Phi}, \quad (\text{A7})$$

where \mathbf{C} is a diagonal matrix containing the capacitances of each branch. Substituting Eq. (A6) into Eq. (A7) gives

$$T(\dot{\phi}, \dot{\phi}_{\text{ext}}) = \frac{1}{2} \dot{\phi}^T \mathbf{C}_\phi \dot{\phi} + \dot{\phi}_{\text{ext}}^T \mathbf{C}_c \dot{\phi}, \quad (\text{A8})$$

where $\mathbf{C}_\phi = \mathbf{A}^T \mathbf{C} \mathbf{A}$ and $\mathbf{C}_c = \mathbf{B}^T \mathbf{C} \mathbf{A}$. We omit terms that are quadratic in the classical external fluxes ϕ_{ext} , as these terms are discarded when the circuit Hamiltonian is quantised. Importantly, the second term in Eq. (A8) indicates that time-dependence in the external fluxes ϕ_{ext} generates an EMF acting on the node fluxes ϕ [49, 50]. The irrotational gauge, where this coupling term vanishes, corresponds to the choice [47]

$$\mathbf{B} = \left(\begin{array}{c} \mathbf{A}^T \mathbf{C} \\ \mathbf{G} \end{array} \right)^+ \left(\begin{array}{c} \mathbf{0} \\ \mathbf{I} \end{array} \right), \quad (\text{A9})$$

where the zero matrix $\mathbf{0}$ has size $n \times l$, the identity matrix \mathbf{I} has size $l \times l$, and \mathbf{O}^+ indicates the psuedoinverse of the matrix \mathbf{O} . For this choice of \mathbf{B} , the kinetic energy has the simplified form

$$T(\dot{\phi}) = \frac{1}{2} \dot{\phi}^T \mathbf{C}_\phi \dot{\phi}. \quad (\text{A10})$$

The potential energy of a circuit is given by

$$V(\Phi) = \frac{1}{2} \Phi^T \mathbf{L}^{-1} \Phi - \sum_{k \in \mathcal{S}_J} E_{J_k} \cos(\Phi_k / \phi_0), \quad (\text{A11})$$

where \mathbf{L}^{-1} is a diagonal matrix containing the inverse inductances of each branch, \mathcal{S}_J is the set of branches that contain Josephson junctions, E_{J_k} is the Josephson energy of the branch Φ_k , and $\phi_0 = \hbar/2e$ is the reduced flux quantum. Substituting Eq. (A6) into Eq. (A11) gives

$$V(\phi, \phi_{\text{ext}}) = \frac{1}{2} \phi^T \mathbf{L}_\phi^{-1} \phi + \phi_{\text{ext}}^T \mathbf{L}_c^{-1} \phi - \sum_{k \in \mathcal{S}_J} E_{J_k} \cos[(\mathbf{A}_k \phi - \mathbf{B}_k \phi_{\text{ext}}) / \phi_0], \quad (\text{A12})$$

where $\mathbf{L}_\phi^{-1} = \mathbf{A}^T \mathbf{L}^{-1} \mathbf{A}$ and $\mathbf{L}_c^{-1} = \mathbf{B}^T \mathbf{L}^{-1} \mathbf{A}$, and \mathbf{A}_k and \mathbf{B}_k are the k -th rows of \mathbf{A} and \mathbf{B} . Again, we omit terms that are quadratic in ϕ_{ext} .

The Lagrangian for a circuit in the irrotational gauge is given by Eqs. (A10) and (A12). Taking the Legendre transform gives us the Hamiltonian:

$$H \equiv \mathbf{q}^T \dot{\boldsymbol{\phi}} - \mathcal{L}, \quad (\text{A13})$$

where \mathbf{q} is a column vector that contains the n node charge variables that are canonically conjugate to the node flux variables $\boldsymbol{\phi}$. By definition,

$$\mathbf{q} \equiv \frac{\partial \mathcal{L}}{\partial \dot{\boldsymbol{\phi}}} = \mathbf{C}_\phi \dot{\boldsymbol{\phi}}, \quad (\text{A14})$$

where we use the fact that $\mathbf{C}_\phi = \mathbf{C}_\phi^T$. Since Eq. (A10) is quadratic in $\boldsymbol{\phi}$, the Hamiltonian for a circuit is given by

$$H = T + V, \quad (\text{A15})$$

where the kinetic energy, expressed in terms of \mathbf{q} , is

$$T(\mathbf{q}) = \frac{1}{2} \mathbf{q}^T \mathbf{C}_\phi^{-1} \mathbf{q}, \quad (\text{A16})$$

and the potential energy is given by Eq. (A12).

However, for many of the circuits that we consider, the node capacitance matrix \mathbf{C}_ϕ is singular and a coordinate transformation is required to obtain a Hamiltonian. We consider coordinate transformations of the form

$$\boldsymbol{\theta} = \frac{1}{\phi_0} \mathbf{M}^{-1} \boldsymbol{\phi}, \quad (\text{A17})$$

where $\boldsymbol{\theta}$ is a column vector containing (unitless) superconducting phase variables, and the coordinate transformation matrix \mathbf{M} is invertible. Substituting Eq. (A17) into Eqs. (A10) and (A12) gives

$$T(\dot{\boldsymbol{\theta}}) = \frac{\phi_0^2}{2} \dot{\boldsymbol{\theta}}^T \mathbf{C}_\theta \dot{\boldsymbol{\theta}}, \quad (\text{A18})$$

where $\mathbf{C}_\theta = \mathbf{M}^T \mathbf{C}_\phi \mathbf{M}$, and

$$V(\boldsymbol{\theta}, \boldsymbol{\varphi}_{\text{ext}}) = \frac{\phi_0^2}{2} \boldsymbol{\theta}^T \mathbf{L}_\theta^{-1} \boldsymbol{\theta} + \phi_0^2 \boldsymbol{\varphi}_{\text{ext}}^T \mathbf{L}_c^{-1} \mathbf{M} \boldsymbol{\theta} - \sum_{k \in \mathcal{S}_J} E_{J_k} \cos(\mathbf{A}_k \mathbf{M} \boldsymbol{\theta} - \mathbf{B}_k \boldsymbol{\varphi}_{\text{ext}}). \quad (\text{A19})$$

where $\mathbf{L}_\theta^{-1} = \mathbf{M}^T \mathbf{L}_\phi^{-1} \mathbf{M}$ and $\boldsymbol{\varphi}_{\text{ext}} = \boldsymbol{\phi}_{\text{ext}}/\phi_0$. The variables canonically conjugate to $\boldsymbol{\theta}$ are given by

$$\mathbf{p} \equiv \frac{\partial \mathcal{L}}{\partial \dot{\boldsymbol{\theta}}} = \phi_0^2 \mathbf{C}_\theta \dot{\boldsymbol{\theta}}, \quad (\text{A20})$$

which have units of angular momentum. It is conventional to define unitless charge number variables

$$\mathbf{n} \equiv \frac{\mathbf{p}}{\hbar} = \frac{\phi_0}{2e} \mathbf{C}_\theta \dot{\boldsymbol{\theta}}. \quad (\text{A21})$$

We can relate the new variables \mathbf{n} to the old variables \mathbf{q} by substituting in Eqs. (A14) and (A17):

$$\mathbf{n} = \frac{1}{2e} \mathbf{M}^T \mathbf{q}. \quad (\text{A22})$$

This allows us to rewrite Eq. (A15) in terms of $\boldsymbol{\theta}$ and \mathbf{n} :

$$H(\mathbf{n}, \boldsymbol{\theta}) = T(\mathbf{n}) + V(\boldsymbol{\theta}, \boldsymbol{\varphi}_{\text{ext}}), \quad (\text{A23})$$

where the kinetic energy, expressed in terms of \mathbf{n} , is

$$T(\mathbf{n}) = \frac{4e^2}{2} \mathbf{n}^T \mathbf{C}_\theta^{-1} \mathbf{n}. \quad (\text{A24})$$

Finally, the circuit Hamiltonian is quantised; classical variables are promoted to quantum operators that satisfy the commutation relations

$$[\hat{\boldsymbol{\theta}}_k, \hat{\mathbf{n}}_l] = i\delta_{kl}. \quad (\text{A25})$$

In the following sections, we use this procedure to derive Hamiltonians for the circuits presented in the main text.

1. $0-\pi$ qubit

The circuit for a $0-\pi$ qubit, shown in Fig. 1(a), has $n = 4$ nodes, $k = 6$ branches, and $l = 1$ loops. The first and second branches have Josephson energies $E_{J_{1,2}}$ and capacitances $C_{J_{1,2}}$, the third and fourth branches have capacitances $C_{1,2}$, and the fifth and sixth branches have inductances $L_{1,2}$. We ignore the capacitance of the inductors, capacitive coupling to ground, and capacitive coupling to any offset voltages. In terms of the branch fluxes, the capacitance matrix is

$$\mathbf{C} = \text{diag}(C_{J_1}, C_{J_2}, C_1, C_2, 0, 0), \quad (\text{A26})$$

and the inverse inductance matrix is

$$\mathbf{L}^{-1} = \text{diag}(0, 0, 0, 0, L_1^{-1}, L_2^{-1}). \quad (\text{A27})$$

The branch fluxes $\boldsymbol{\Phi}$ are related to the node fluxes $\boldsymbol{\phi}$ according to Eq. (A6), where

$$\mathbf{A} = \begin{pmatrix} 1 & -1 & 0 & 0 \\ 0 & 0 & 1 & -1 \\ 1 & 0 & 0 & -1 \\ 0 & 1 & -1 & 0 \\ 1 & 0 & -1 & 0 \\ 0 & 1 & 0 & -1 \end{pmatrix}, \quad (\text{A28})$$

and \mathbf{B} is given by Eq. (A9). The external flux ϕ_{ext} is related to the branch fluxes $\boldsymbol{\Phi}$ by Eq. (A5), where

$$\mathbf{G} = (1 \ -1 \ 0 \ 0 \ -1 \ 1). \quad (\text{A29})$$

The Hamiltonian for the circuit is $H = T + V$, where T is given by Eq. (A16), and V is given by Eq. (A12). However, the matrix $\mathbf{C}_\phi = \mathbf{A}^T \mathbf{C} \mathbf{A}$ evaluates to

$$\mathbf{C}_\phi = \begin{pmatrix} C_1 + C_{J_1} & -C_{J_1} & 0 & -C_1 \\ -C_{J_1} & C_2 + C_{J_1} & -C_2 & 0 \\ 0 & -C_2 & C_2 + C_{J_2} & -C_{J_2} \\ -C_1 & 0 & -C_{J_2} & C_1 + C_{J_2} \end{pmatrix}, \quad (\text{A30})$$

which is singular. To proceed, we perform a coordinate transformation according to Eqs. (A17) and (A22). We define new superconducting phase and number variables

$$\boldsymbol{\theta} = \begin{pmatrix} \theta \\ \varphi \\ \zeta \\ \Sigma \end{pmatrix}, \quad \mathbf{n} = \begin{pmatrix} n_\theta \\ n_\varphi \\ n_\zeta \\ n_\Sigma \end{pmatrix}, \quad (\text{A31})$$

and the invertible transformation matrix [8]

$$\mathbf{M}^{-1} = \frac{1}{2} \begin{pmatrix} 1 & -1 & 1 & -1 \\ 1 & -1 & -1 & 1 \\ 1 & 1 & -1 & -1 \\ 1 & 1 & 1 & 1 \end{pmatrix}. \quad (\text{A32})$$

The matrix \mathbf{M}^{-1} is orthogonal, so $\mathbf{M}^{-1} = \mathbf{M}^T$. The new variables $\boldsymbol{\theta}$ and \mathbf{n} are quadrupole combinations of $\boldsymbol{\phi}$ and \mathbf{q} , respectively. The quadrupoles are illustrated in Fig. 1(a). The transformed capacitance matrix is

$$\mathbf{C}_\theta = \mathbf{M}^T \mathbf{C}_\phi \mathbf{M} = \begin{pmatrix} C_\zeta + C_\varphi & \delta C_\varphi & \delta C_\zeta & 0 \\ \delta C_\varphi & C_\varphi & 0 & 0 \\ \delta C_\zeta & 0 & C_\zeta & 0 \\ 0 & 0 & 0 & 0 \end{pmatrix}, \quad (\text{A33})$$

where $C_\zeta = C_1 + C_2$, $C_\varphi = C_{J_1} + C_{J_2}$, $\delta C_\zeta = C_1 - C_2$, and $\delta C_\varphi = C_{J_1} - C_{J_2}$. Following a similar process, the transformed inverse inductance matrix is

$$\mathbf{L}_\theta^{-1} = \frac{1}{\phi_0^2} \begin{pmatrix} 0 & 0 & 0 \\ 0 & 2\bar{E}_L & \delta E_L & 0 \\ 0 & \delta E_L & 2\bar{E}_L & 0 \\ 0 & 0 & 0 & 0 \end{pmatrix}, \quad (\text{A34})$$

where $\bar{E}_L = \phi_0^2/2L_1 + \phi_0^2/2L_2$ and $\delta E_L = \phi_0^2/L_1 - \phi_0^2/L_2$.

We can now write the circuit Hamiltonian in terms of the new variables, where T is given by Eq. (A24) and V is given by Eq. (A19). The circuit Hamiltonian is obtained by inverting the capacitance matrix \mathbf{C}_θ . Since the Σ variable does appear in the Lagrangian, we can restrict our model to the three remaining variables. It is also convenient to rewrite Eq. (A33) in the form

$$\mathbf{C}_\theta = \begin{pmatrix} C_\theta + r_\varphi^2 C_\varphi + r_\zeta^2 C_\zeta & r_\varphi C_\varphi & r_\zeta C_\zeta \\ r_\varphi C_\varphi & C_\varphi & 0 \\ r_\zeta C_\zeta & 0 & C_\zeta \end{pmatrix}, \quad (\text{A35})$$

where $C_\theta = C_\zeta(1 - r_\zeta^2) + C_\varphi(1 - r_\varphi^2)$, $r_\zeta = \delta C_\zeta/C_\zeta$, and $r_\varphi = \delta C_\varphi/C_\varphi$. The inverse of Eq. (A35) is

$$\mathbf{C}_\theta^{-1} = \begin{pmatrix} \frac{1}{C_\theta} & -\frac{r_\varphi}{C_\theta} & -\frac{r_\zeta}{C_\theta} \\ -\frac{r_\varphi}{C_\theta} & \frac{1}{C_\varphi} + \frac{r_\varphi^2}{C_\theta} & \frac{r_\zeta r_\varphi}{C_\theta} \\ -\frac{r_\zeta}{C_\theta} & \frac{r_\zeta r_\varphi}{C_\theta} & \frac{1}{C_\zeta} + \frac{r_\zeta^2}{C_\theta} \end{pmatrix}. \quad (\text{A36})$$

The irrotational gauge constraint Eq. (A9) is particularly messy when $\delta C_\varphi \neq 0$. For simplicity, we provide

two sets of expressions for T and V . The first is for symmetric circuit elements, discussed in Section III,

$$\begin{aligned} \hat{T}_{\text{sym}} &= 4E_{C_\theta} \hat{n}_\theta^2 + 4E_{C_\varphi} \hat{n}_\varphi^2 + 4E_{C_\zeta} \hat{n}_\zeta^2, \\ \hat{V}_{\text{sym}} &= E_L \left[\left(\hat{\phi} - \frac{\varphi_{\text{ext}}}{2} \right)^2 + \hat{\zeta}^2 \right] - 2E_J \cos \hat{\theta} \cos \hat{\phi}, \end{aligned} \quad (\text{A37})$$

where $E_{C_\theta} = e^2/2C_\theta$, $E_{C_\varphi} = e^2/2C_\varphi$, $E_{C_\zeta} = e^2/2C_\zeta$, $E_L = \phi_0^2/L_1 = \phi_0/L_2$ and $E_J = E_{J_1} = E_{J_2}$. The second is for asymmetric circuit elements and $\phi_{\text{ext}} = 0$,

$$\begin{aligned} \hat{T}_{\text{asym}} &= 4E_{C_\theta} (\hat{n}_\theta - r_\varphi \hat{n}_\varphi - r_\zeta \hat{n}_\zeta)^2 + 4E_{C_\varphi} \hat{n}_\varphi^2 + 4E_{C_\zeta} \hat{n}_\zeta^2, \\ \hat{V}_{\text{asym}} &= \bar{E}_L (\hat{\phi}^2 + \hat{\zeta}^2) + \delta E_L \hat{\phi} \hat{\zeta} - 2\bar{E}_J \cos \hat{\theta} \cos \hat{\phi} \\ &\quad + \delta E_J \sin \hat{\theta} \sin \hat{\phi}, \end{aligned} \quad (\text{A38})$$

where $\bar{E}_J = (E_{J_1} + E_{J_2})/2$ and $\delta E_J = E_{J_1} - E_{J_2}$. This is discussed in Section IV A.

2. $0-\pi$ qubit coupled to an oscillator

Next we consider the circuit for a $0-\pi$ qubit that is Josephson-coupled to a harmonic oscillator, as shown in Fig. 1(b). Here we treat the tunable Josephson element as a purely inductive element, consisting of two symmetric Josephson junctions with no capacitance threaded by an external flux. In Appendices A 6 a and A 6 b we consider the effects of non-zero capacitance and asymmetry in the tunable Josephson element.

This circuit has $n = 5$ nodes, $k = 10$ branches, and $l = 3$ loops. The circuit is much the same as the bare $0-\pi$ qubit described in the previous section, with the addition of four new circuit elements. We have added two Josephson junction with energies E_{J_s} , a capacitor with capacitance C_ϕ and inductor with inductance L_ϕ . This modifies the branch capacitance matrix

$$\mathbf{C} = \text{diag}(C_{J_1}, C_{J_2}, 0, 0, C_1, C_2, 0, 0, C_\phi, 0), \quad (\text{A39})$$

and the inverse inductance matrix

$$\mathbf{L}^{-1} = \text{diag}(0, 0, 0, 0, 0, 0, L_1^{-1}, L_2^{-1}, 0, L_\phi^{-1}). \quad (\text{A40})$$

The vector of external fluxes for the three loops is

$$\boldsymbol{\phi}_{\text{ext}} = \begin{pmatrix} \phi_{\text{ext}}^q \\ \phi_{\text{ext}}^s \\ \phi_{\text{ext}}^{\text{qs}} \end{pmatrix}, \quad (\text{A41})$$

where ϕ_{ext}^q , ϕ_{ext}^s are the external fluxes threading the $0-\pi$ qubit loop and the SQUID loop, and $\phi_{\text{ext}}^{\text{qs}}$ is the external flux threading the loop between the $0-\pi$ qubit and the oscillator. We assume all external fluxes have the same orientation. As before, we must specify the matrices \mathbf{A} and \mathbf{G} that relate the branch fluxes $\boldsymbol{\Phi}$ to the nodes fluxes $\boldsymbol{\phi}$ and external fluxes $\boldsymbol{\phi}_{\text{ext}}$, respectively. The matrix \mathbf{A}

has four added rows (for the four added branches) and a single added column (for the single added node):

$$\mathbf{A} = \begin{pmatrix} 1 & -1 & 0 & 0 & 0 \\ 0 & 0 & 1 & -1 & 0 \\ 1 & 0 & 0 & 0 & -1 \\ 1 & 0 & 0 & 0 & -1 \\ 1 & 0 & 0 & -1 & 0 \\ 0 & 1 & -1 & 0 & 0 \\ 1 & 0 & -1 & 0 & 0 \\ 0 & 1 & 0 & -1 & 0 \\ 0 & 0 & 0 & 1 & -1 \\ 0 & 0 & 0 & 1 & -1 \end{pmatrix}. \quad (\text{A42})$$

Likewise, the matrix \mathbf{G} has two added rows (for the two added external fluxes) and four added columns (for the four added branches):

$$\mathbf{G} = \begin{pmatrix} 1 & -1 & 0 & 0 & 0 & 0 & -1 & 1 & 0 & 0 \\ 0 & 0 & -1 & 1 & 0 & 0 & 0 & 0 & 0 & 0 \\ -1 & 0 & 1 & 0 & 0 & 0 & 0 & -1 & 0 & -1 \end{pmatrix}. \quad (\text{A43})$$

As before, we perform a coordinate transformation to a new set of variables, which we denote

$$\boldsymbol{\theta} = \begin{pmatrix} \theta \\ \varphi \\ \zeta \\ \Sigma \end{pmatrix}, \quad \mathbf{n} = \begin{pmatrix} n_\theta \\ n_\varphi \\ n_\zeta \\ n_\Sigma \\ n_\phi \end{pmatrix}, \quad (\text{A44})$$

where the invertible transformation matrix is [12]

$$\mathbf{M}^{-1} = \frac{1}{2} \begin{pmatrix} 1 & -1 & 1 & -1 & 0 \\ 1 & -1 & -1 & 1 & 0 \\ 1 & 1 & -1 & -1 & 0 \\ 1 & 1 & 1 & 1 & 0 \\ 0 & 0 & 0 & -2 & 2 \end{pmatrix}. \quad (\text{A45})$$

The transformed capacitance matrix is

$$\mathbf{C}_\theta = \begin{pmatrix} C_\zeta + C_\varphi & \delta C_\varphi & \delta C_\zeta & 0 & 0 \\ \delta C_\varphi & C_\varphi & 0 & 0 & 0 \\ \delta C_\zeta & 0 & C_\zeta & 0 & 0 \\ 0 & 0 & 0 & 0 & 0 \\ 0 & 0 & 0 & 0 & C_\phi \end{pmatrix}, \quad (\text{A46})$$

and the transformed inverse inductance matrix is

$$\mathbf{L}_\theta^{-1} = \frac{1}{\phi_0^2} \begin{pmatrix} 0 & 0 & 0 & 0 & 0 \\ 0 & 2\bar{E}_L & \delta E_L & 0 & 0 \\ 0 & \delta E_L & 2\bar{E}_L & 0 & 0 \\ 0 & 0 & 0 & 0 & 0 \\ 0 & 0 & 0 & 0 & E_{L\phi} \end{pmatrix}, \quad (\text{A47})$$

where we have defined $E_{L\phi} = \phi_0^2/L_\phi$. In the regime of symmetric $0-\pi$ circuit elements, and after fixing the flux between the qubit and oscillator to be $\varphi_{\text{ext}}^{\text{qs}} = -\varphi_{\text{ext}}^{\text{q}}/2 - \varphi_{\text{ext}}^{\text{s}}/2$, the full expressions for the kinetic and potential

energies are

$$\begin{aligned} \hat{T} &= \hat{T}_{\text{sym}} + 4E_{C_\phi} \hat{n}_\phi^2, \\ \hat{V} &= \hat{V}_{\text{sym}} + \frac{E_{L\phi}}{2} \hat{\phi}^2 - 2E_{J_s} \cos\left(\frac{\varphi_{\text{ext}}^{\text{s}}}{2}\right) \cos(\hat{\phi} - \hat{\theta} + \hat{\zeta}), \end{aligned} \quad (\text{A48})$$

where \hat{T}_{sym} and \hat{V}_{sym} are given in Eq. (A37) with $\varphi_{\text{ext}} = \varphi_{\text{ext}}^{\text{q}}$. The last term in the potential gives rise to the interaction Hamiltonian in Eq. (19) with $E_{J_{\text{int}}}(t) = 2E_{J_s} \cos(\varphi_{\text{ext}}^{\text{s}}/2)$, and the full Hamiltonian is therefore equal to $\hat{H}(t) = \hat{H}_\phi + \hat{H}_{\theta\varphi} + \hat{H}_\zeta + \hat{H}_{\text{int}}^\phi(t)$, with the terms given by Eqs. (6), (16), (17) and (19), respectively.

3. Coupling to the internal ζ mode

Figure 1(c) shows the circuit diagram for coupling to the internal ζ mode. Once again, we assume the tunable Josephson element to be a symmetric SQUID with Josephson energies E_{J_s} and no capacitance. This circuit has $n = 5$ nodes, $k = 8$ branches and $l = 3$ loops. Similarly to the previous section we denote by $\phi_{\text{ext}}^{\text{q}}$, $\phi_{\text{ext}}^{\text{s}}$ and $\phi_{\text{ext}}^{\text{qs}}$ the external fluxes threading the $0-\pi$ qubit, the tunable Josephson element, and the loop threading the qubit and tunable Josephson element, respectively. As in the previous section, we fix the latter flux to be $\phi_{\text{ext}}^{\text{qs}} = -\phi_{\text{ext}}^{\text{q}}/2 - \phi_{\text{ext}}^{\text{s}}/2$. Then, following the same quantisation procedure and assuming symmetry in the $0-\pi$ qubit, the kinetic and potential energies become

$$\begin{aligned} \hat{T} &= \hat{T}_{\text{sym}}, \\ \hat{V} &= \hat{V}_{\text{sym}} - 2E_{J_s} \cos\left(\frac{\varphi_{\text{ext}}^{\text{s}}}{2}\right) \cos(\hat{\zeta} + \hat{\theta}), \end{aligned} \quad (\text{A49})$$

where \hat{T}_{sym} and \hat{V}_{sym} are given in Eq. (A37) with $\varphi_{\text{ext}} = \varphi_{\text{ext}}^{\text{q}}$. The last term in the potential gives rise to the interaction Hamiltonian in Eq. (21) with $E_{J_{\text{int}}}(t) = 2E_{J_s} \cos(\varphi_{\text{ext}}^{\text{s}}/2)$, and the full Hamiltonian is therefore equal to $\hat{H}(t) = \hat{H}_\phi + \hat{H}_{\theta\varphi} + \hat{H}_\zeta + \hat{H}_{\text{int}}^\phi(t)$, with the terms given by Eqs. (6), (16), (17) and (21), respectively.

Relaxing the symmetry requirement in the $0-\pi$ qubit leads to the same Hamiltonian, but with \hat{T}_{sym} and \hat{V}_{sym} in Eq. (A49) replaced with \hat{T}_{asym} and \hat{V}_{asym} from Eq. (A38). However, the irrotational gauge constraint requires $\phi_{\text{ext}}^{\text{qs}}$ to be given by a different linear combination of $\phi_{\text{ext}}^{\text{q}}$ and $\phi_{\text{ext}}^{\text{s}}$, which may be found by solving a linear system. We omit its expression here for the sake of clarity.

Finally, we note that non-zero capacitance in the tunable Josephson element may be accounted for by simply redefining the capacitive disorder in \hat{T}_{asym} to be $\delta C_\zeta = C_1 + C_{\text{int}} - C_2$, where C_{int} is the capacitance of the tunable Josephson element.

4. Coupling to the internal φ mode

The inset of Fig. 13(b) shows the circuit diagram for coupling to the internal φ mode for the gate considered in

Section III D and Appendix D 4. We assume both tunable Josephson elements are symmetric SQUIDS with Josephson energies E_{J_s} and capacitances $C_J/2$. Furthermore, we assume the flux threading both tunable Josephson elements are identical. This circuit has $n = 5$ nodes, $k = 8$ branches and $l = 3$ loops. Here we denote by ϕ_{ext}^q and ϕ_{ext}^s the external fluxes threading the qubit and the two tunable Josephson elements, respectively. Following the same procedure as in the previous sections, and assuming symmetry in the $0-\pi$ qubit, the kinetic and potential energies become

$$\begin{aligned} \hat{T} &= \hat{T}_{\text{sym}}, \\ \hat{V} &= E_L \left[\left(\hat{\varphi} - \frac{\varphi_{\text{ext}}^q}{2} - \frac{\varphi_{\text{ext}}^s}{2} \right)^2 + \hat{\zeta}^2 \right] \\ &\quad - 4E_{J_s} \cos\left(\frac{\varphi_{\text{ext}}^s}{2}\right) \cos \hat{\theta} \cos \hat{\varphi}, \end{aligned} \quad (\text{A50})$$

where \hat{T}_{sym} is given in Eq. (A37). Upon identifying $\varphi_{\text{ext}}^q + \varphi_{\text{ext}}^s$ with φ_{ext} and $4E_{J_s} \cos(\varphi_{\text{ext}}^s/2)$ with $2E_J$, this becomes identical to Eq. (A37). The last term in the potential becomes the interaction Hamiltonian, which we use in Eq. (D10) with $E_{J_{\text{int}}}(t) = 4E_{J_s} \cos(\varphi_{\text{ext}}^s/2)$.

5. Series $0-\pi$ qubits

Figure 7 shows the circuit diagram for two $0-\pi$ qubits connected in series and shunted by a SQUID for the two-qubit gate discussed in Section V A. This circuit consists of $n = 7$ nodes, $k = 14$ branches and $l = 4$ loops. To separate out the symmetric and anti-symmetric ζ modes of the coupled system, we define the following new set of variables

$$\boldsymbol{\theta} = \begin{pmatrix} \theta_a \\ \varphi_a \\ \theta_b \\ \varphi_b \\ \zeta_+ \\ \zeta_- \\ \Sigma \end{pmatrix}, \quad \mathbf{n} = \begin{pmatrix} n_{\theta_a} \\ n_{\varphi_a} \\ n_{\theta_b} \\ n_{\varphi_b} \\ n_{\zeta_+} \\ n_{\zeta_-} \\ n_{\Sigma} \end{pmatrix}, \quad (\text{A51})$$

which are related to the 7 nodes of the circuit shown in Fig. 7 via the following coordinate transformation

$$\mathbf{M}^{-1} = \frac{1}{2} \begin{pmatrix} 1 & -1 & 1 & -1 & 0 & 0 & 0 \\ 1 & -1 & -1 & 1 & 0 & 0 & 0 \\ 0 & 0 & 0 & 1 & -1 & 1 & -1 \\ 0 & 0 & 0 & 1 & -1 & -1 & 1 \\ 1 & 1 & -1 & 0 & 1 & -1 & -1 \\ 1 & 1 & -1 & -2 & -1 & 1 & 1 \\ 1 & 1 & 1 & 1 & 1 & 1 & 1 \end{pmatrix}. \quad (\text{A52})$$

For simplicity, we assume each $0-\pi$ qubit to be symmetric, and treat each tunable Josephson element as a symmetric SQUID with no capacitance. We denote the external fluxes in each $0-\pi$ qubit by ϕ_{ext}^a and ϕ_{ext}^b , the external flux threading the tunable Josephson element by

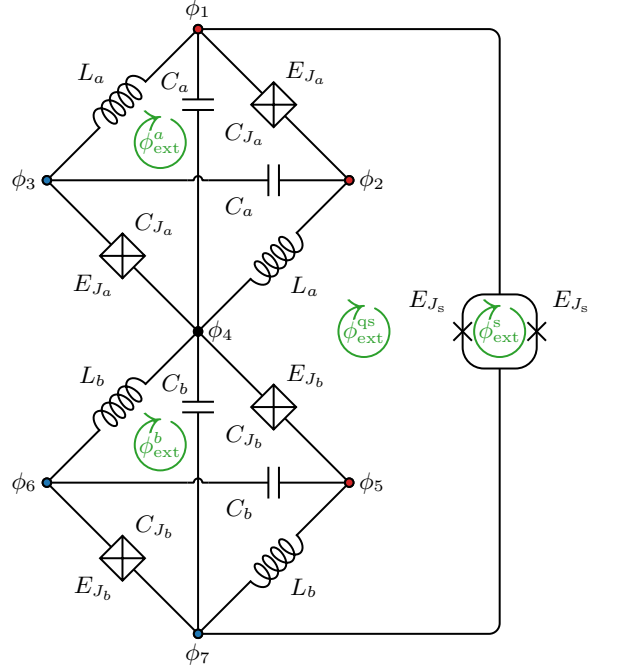


FIG. 7. Circuit diagram for a protected two-qubit gate using the internal ζ modes of two $0-\pi$ qubits connected in series. The node colours correspond to the symmetric coupled ζ mode, ζ_+ , which is used to perform the gate. Each $0-\pi$ qubit is assumed to be symmetric, and the gate is performed by bringing the qubits onto resonance ($C_a = C_b$, $L_a = L_b$).

ϕ_{ext}^s , and the external flux threading the loop between the qubits and the tunable Josephson junction by $\phi_{\text{ext}}^{\text{qs}}$. Using the well-established quantisation procedure, and fixing $\phi_{\text{ext}}^{\text{qs}} = -(\phi_{\text{ext}}^a + \phi_{\text{ext}}^b + \phi_{\text{ext}}^s)/2$, the kinetic and potential energies for the circuit are

$$\begin{aligned} \hat{T} &= \sum_{i=a,b} \left[4E_{C_{\theta_i}} \hat{n}_{\theta_i}^2 + 4E_{C_{\varphi_i}} \hat{n}_{\varphi_i}^2 \right] \\ &\quad + 4E_{C_{\zeta}} (\hat{n}_{\zeta_+}^2 + \hat{n}_{\zeta_-}^2 - 2r_{\zeta} \hat{n}_{\zeta_+} \hat{n}_{\zeta_-}), \\ \hat{V} &= \sum_{i=a,b} \left[E_{L_i} \left(\hat{\varphi}_i + \frac{\varphi_{\text{ext}}^i}{2} \right)^2 - 2E_{J_i} \cos(\hat{\theta}_i) \cos(\hat{\varphi}_i) \right] \\ &\quad + E_{L_{\zeta}} (\hat{\zeta}_+^2 + \hat{\zeta}_-^2) - \delta E_L \hat{\zeta}_+ \hat{\zeta}_- \\ &\quad - 2E_{J_s} \cos\left(\frac{\varphi_{\text{ext}}^s}{2}\right) \cos(\hat{\theta}_a + \hat{\theta}_b + \hat{\zeta}_+). \end{aligned} \quad (\text{A53})$$

Here, $E_{C_{\theta_i}} = e^2/4(C_i + C_{J_i})$, $E_{C_{\varphi_i}} = e^2/4C_{J_i}$, $E_{C_{\zeta}} = e^2/4E_{C_a} + e^2/4C_b$, $r_{\zeta} = (C_a - C_b)/(C_a + C_b)$, $E_{L_i} = \phi_0^2/L_i$, $E_{L_{\zeta}} = (E_{L_a} + E_{L_b})/2$ and $\delta E_L = (E_{L_a} - E_{L_b})/2$. Crucially, when the two $0-\pi$ qubits are brought on resonance ($C_a = C_b$ and $L_a = L_b$), then $r_{\zeta} = \delta E_L = 0$ and the symmetric and antisymmetric ζ -modes decouple. In this case, the final term facilitates a conditional phase of $\pi/2$ acquired by the ζ_+ mode when $\theta_a = \theta_b = \pi \bmod 2\pi$, thus enacting the logical unitary

operation $\exp(-i\frac{\pi}{4}\hat{Z} \otimes \hat{Z})$.

If the SQUID is replaced by an ancillary oscillator, as originally proposed in Ref. [6, 7], then the resulting Hamiltonian is the same as Eq. (A53) with the addition of the bare-oscillator Hamiltonian and with the replacement $\cos(\hat{\theta}_a + \hat{\theta}_b + \hat{\zeta}_+) \rightarrow \cos(\hat{\theta}_a + \hat{\theta}_b + \hat{\zeta}_+ - \hat{\phi})$ in the final term in Eq. (A53), where $\hat{\phi}$ represents the degree of freedom for the ancillary oscillator. Therefore, the coupling to the ζ -mode persists when coupling two qubits to an external oscillator, leading to the same exponential suppression of the interaction strength as for the single-qubit gate.

6. Tunable Josephson element

Here we give supporting analysis for the implementation of the tunable Josephson element. In Appendix A 6 a we discuss the effect of its capacitance and in Appendix A 6 b we discuss ways to obtain a large dynamic range.

a. Capacitance of the tunable Josephson element

For simplicity, we consider the case of the ideal qubit coupled to an external oscillator. Here, a non-zero capacitance in the tunable Josephson element leads to the following kinetic energy for the coupled system

$$\hat{T} = 4E'_C \hat{n}_\theta^2 + 4E'_{C_\phi} \hat{n}_\phi^2 + 4E_{C_{\theta\phi}} \hat{n}_\theta \hat{n}_\phi, \quad (\text{A54})$$

where $E'_C = e^2(C_\phi + C_{\text{int}})/2\tilde{C}$ and $E'_{C_\phi} = e^2(C_\theta + C_{\text{int}})/2\tilde{C}$ are the dressed charging energies for the qubit and oscillator, respectively, and $E_{C_{\theta\phi}} = e^2 C_{\text{int}}/2\tilde{C}$ is an effective charging energy for the charge-charge coupling term. Here, $C_\theta = C_J + C$, C_ϕ and C_{int} are the capacitances of the qubit, oscillator and the tunable Josephson element, respectively, and $\tilde{C} = C_\theta C_\phi + C_\theta C_{\text{int}} + C_\phi C_{\text{int}}$. In the limit that $C_{\text{int}} \rightarrow 0$, we recover $E'_C = E_C$, $E'_{C_\phi} = E_{C_\phi}$ and $E_{C_{\theta\phi}} = 0$, which corresponds to the kinetic energy considered in Section II. The dressed charging energies may be expressed in terms of the ratios $r_{\text{int}} = C_{\text{int}}/C_\phi$ and $r_{\theta\phi} = C_\theta/C_\phi$ as

$$\frac{E_{C_{\text{int}}}}{E'_{C_\phi}} = \frac{r_{\text{int}}}{r_{\theta\phi} + r_{\text{int}}} \approx \frac{r_{\text{int}}}{r_{\theta\phi}}, \quad (\text{A55})$$

$$\frac{E'_{C_\theta}}{E'_{C_\phi}} = \frac{1 + r_{\text{int}}}{r_{\theta\phi} + r_{\text{int}}} \approx \frac{1}{r_{\theta\phi}} + \frac{r_{\text{int}}}{r_{\theta\phi}}, \quad (\text{A56})$$

where the approximations hold for $r_{\text{int}} \ll 1 \ll r_{\theta\phi}$. This reveals that the spurious charge-charge coupling is approximately proportional to $r_{\text{int}}/r_{\theta\phi} = C_{\text{int}}/C_\theta$ and that the charging energy ratio, $E'_{C_\theta}/E'_{C_\phi}$ is increased by this same quantity.

Figure 8 shows the effect of r_{int} on the performance of a gate with an ideal qubit coupled to an external oscillator. The results show that the gate is nearly un-

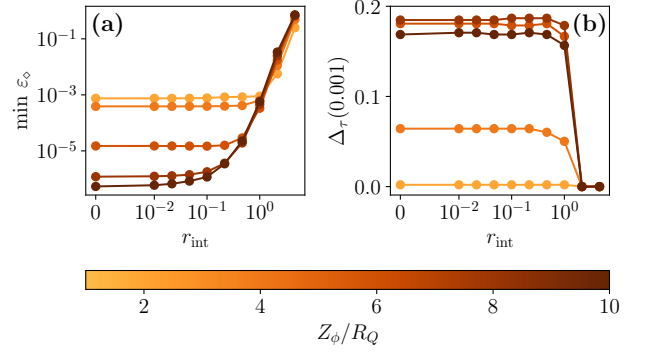


FIG. 8. Gate errors for an ideal qubit coupled to an external oscillator with non-zero Josephson element capacitance. Imprecision (a) and robustness (b) of the gate as a function of the capacitance ratio $r_{\text{int}} = C_{\text{int}}/C_\phi$, for different impedances of the oscillator Z_ϕ . Throughout, $r_{\theta\phi} = C_\theta/C_\phi = 100$, $E_{J_{\text{min}}} = 0$, $E_{J_{\text{max}}}/E'_{C_\phi} = 100$ and $E_J/E'_{C_\phi} = 1$.

affected up until $r_{\text{int}} = 0.1$ and begins to lose its protection once $r_{\text{int}} > 1$. For a fixed plasma frequency, $\hbar\omega_p = \sqrt{8E_{J_{\text{max}}}E_{C_{\text{int}}}}$, where $E_{C_{\text{int}}} = e^2/2C_{\text{int}}$ is the charging energy of the tunable Josephson element, the maximal interaction strength is given by

$$\frac{E_{J_{\text{max}}}}{E'_{C_\phi}} = \frac{r_{\theta\phi}r_{\text{int}} + r_{\theta\phi}r_{\text{int}}^2 + r_{\text{int}}^2}{8(r_{\theta\phi} + r_{\text{int}})} \left(\frac{\hbar\omega_p}{E_{C_\phi}} \right)^2 \quad (\text{A57})$$

$$\approx \frac{r_{\text{int}}}{8} \left(\frac{\hbar\omega_p}{E_{C_\phi}} \right)^2, \quad (\text{A58})$$

where the approximation holds for $r_{\text{int}} \ll 1 \ll r_{\theta\phi}$.

The above analysis may be taken as a best-case scenario for a $0-\pi$ qubit coupled to an external oscillator. Assuming the oscillator impedance may be obtained with $E_{C_\phi}/h = 1$ GHz and $E_{L_\phi}/h = 2$ MHz, the maximum Josephson coupling required for the protected gate would be greater than $E_{J_{\text{max}}}/h = 8 \times 10^4$ GHz. With a plasma frequency of the tunable Josephson element of $\omega_p/2\pi = 40$ GHz, this implies that $C_{\text{int}}/C_\phi > 100$, which is well above the requirement for the gate to remain protected. Assuming a plasma frequency of $\omega_p/2\pi = 40$ GHz and a bare oscillator charging energy of $E_{C_\phi}/h = 1$ GHz yields a maximal coupling strength of $E_{J_{\text{max}}}/E'_{C_\phi} \approx 200r_{\text{int}}$. Requiring $r_{\text{int}} < 1$ then restricts the dynamic range to values $E_{J_{\text{max}}}/E'_{C_\phi} < 200$. This upper bound is larger than the values considered in Section II. However, taking this bound as a best-case scenario for the $0-\pi$ qubit coupled to an external oscillator, its value is too small to achieve a protected gate, where we found a value of $E_{J_{\text{max}}}/E_{C_\phi} > 8 \times 10^4$ was necessary in Section III C. As mentioned in Appendix A 3, the capacitance in the tunable Josephson element may be lumped into the capacitance for the ζ mode, which avoids these spurious effects so long as the $0-\pi$ qubit remains symmetric.

b. *Extending the dynamic range of a flux-tunable Josephson element*

Consider the potential energy for a SQUID with Josephson junction energies E_{J_1} and E_{J_2} ,

$$\begin{aligned}\hat{V} &= -(E_{J_1} + E_{J_2}) \cos(\varphi_{\text{ext}}) \cos(\hat{\phi}) \\ &\quad - (E_{J_1} - E_{J_2}) \sin(\varphi_{\text{ext}}) \sin(\hat{\phi}) \\ &= E_{J_{\text{eff}}}(\varphi_{\text{ext}}) \cos(\hat{\phi} - \varphi_0),\end{aligned}\quad (\text{A59})$$

where

$$E_{J_{\text{eff}}}(\varphi_{\text{ext}}) = (E_{J_1} + E_{J_2}) \sqrt{1 + d^2 \tan^2(\varphi_{\text{ext}})}, \quad (\text{A60})$$

$d = (E_{J_1} - E_{J_2}) / (E_{J_1} + E_{J_2})$ is the Josephson asymmetry and $\tan \varphi_0 = d \tan \varphi_{\text{ext}}$. Its dynamic range is then given by $1/d$, and is therefore determined by the asymmetry of the two Josephson junctions. Now consider the case where each Josephson junction is replaced by a SQUID as shown in Fig. 9(a). The basic idea is that the two time-independent fluxes in each of the smaller loops ϕ_a and ϕ_b are used to bring the effective Josephson energies of each loop closer to each other, whilst the time-dependent flux in the central loop ϕ_t is used to tune the overall potential energy. Here we show that this results in a dynamic range that is limited by the flux noise in the external fluxes rather than the static Josephson asymmetries.

Following the procedure outlined in Appendix A, the potential energy for the circuit is

$$\hat{V} = - \sum_{i=1}^4 E_{J_i} \cos(\hat{\phi} + \mathbf{C}_{J_i} \varphi), \quad (\text{A61})$$

where

$$\varphi = \begin{pmatrix} \varphi_a \\ \varphi_t \\ \varphi_b \end{pmatrix} \quad (\text{A62})$$

and \mathbf{C}_{J_i} denotes the i -th row of the matrix

$$\mathbf{C}_J = \frac{1}{C_\Sigma} \begin{pmatrix} C_{J_1} - C_\Sigma & -C_{J_3} - C_{J_4} & -C_{J_4} \\ C_{J_1} & -C_{J_3} - C_{J_4} & -C_{J_4} \\ C_{J_1} & C_{J_1} + C_{J_2} & -C_{J_4} \\ C_{J_1} & -C_{J_1} - C_{J_2} & C_{J_4} - C_\Sigma \end{pmatrix}, \quad (\text{A63})$$

with $C_\Sigma = C_{J_1} + C_{J_2} + C_{J_3} + C_{J_4}$ the total capacitance.

Taking all Josephson junctions to be equal up to the

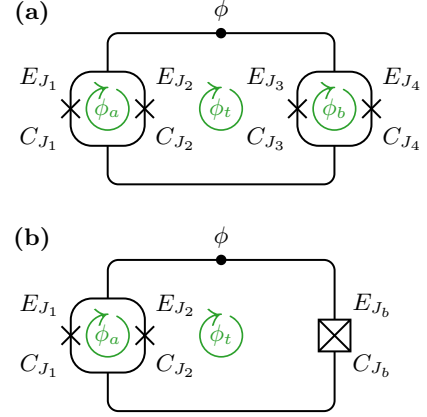


FIG. 9. (a) Three-loop and (b) two-loop SQUIDs for realising a tunable Josephson element. ϕ_a and ϕ_b are time-independent external fluxes, whereas ϕ_t is a time-dependent external flux. ϕ denotes the single degree of freedom in the circuit.

following asymmetries

$$\begin{aligned}d_a &= \frac{C_{J_1} - C_{J_2}}{C_{J_1} + C_{J_2}} \\ &= \frac{E_{J_1} - E_{J_2}}{E_{J_1} + E_{J_2}},\end{aligned}\quad (\text{A64})$$

$$\begin{aligned}d_b &= \frac{C_{J_3} - C_{J_4}}{C_{J_3} + C_{J_4}} \\ &= \frac{E_{J_3} - E_{J_4}}{E_{J_3} + E_{J_4}},\end{aligned}\quad (\text{A65})$$

$$\begin{aligned}d_{ab} &= \frac{C_{J_1} + C_{J_2} - C_{J_3} - C_{J_4}}{C_{J_1} + C_{J_2} + C_{J_3} + C_{J_4}} \\ &= \frac{E_{J_1} + E_{J_2} - E_{J_3} - E_{J_4}}{E_{J_1} + E_{J_2} + E_{J_3} + E_{J_4}},\end{aligned}\quad (\text{A66})$$

Eq. (A61) may be rewritten as

$$\begin{aligned}\hat{V} &= -E_{J_a^{\text{eff}}}(\varphi'_a) \cos(\hat{\phi} - \varphi'_t - \varphi_0 + d_{ab}\varphi'_t) \\ &\quad - E_{J_b^{\text{eff}}}(\varphi'_b) \cos(\hat{\phi} + \varphi'_t - \varphi_0 + d_{ab}\varphi'_t),\end{aligned}\quad (\text{A67})$$

where

$$E_{J_i^{\text{eff}}}(\varphi'_i) = E_{J_i} \sqrt{1 + d_i^2 \tan^2(\varphi'_i)} \cos(\varphi'_i), \quad (\text{A68})$$

are the effective tunable Josephson energies for the left ($i = a$) and right ($i = b$) loops with $E_{J_a} = E_{J_1} + E_{J_2}$ and $E_{J_b} = E_{J_3} + E_{J_4}$. In these equations, the transformed fluxes are

$$\varphi'_a = \frac{\varphi_a}{2} \quad (\text{A69})$$

$$\varphi'_b = \frac{\varphi_b}{2} \quad (\text{A70})$$

$$\varphi'_t = \frac{1}{2} (\varphi_t - \varphi'_a - \varphi'_b + \alpha_a - \alpha_b) \quad (\text{A71})$$

$$\varphi_0 = \frac{1}{2} [(1 + d_{ab})(d_a \varphi'_a + \alpha_a) + (1 - d_{ab})(d_b \varphi'_b + \alpha_b)], \quad (\text{A72})$$

with $\tan \alpha_a = d_a \tan \varphi'_a$ and $\tan \alpha_b = d_b \tan \varphi'_b$. Importantly, we note that φ'_t is the only time-dependent quantity in these equations. Equation (A67) can now be rewritten in terms of a single cosine potential as

$$\hat{V} = -E_{J_t^{\text{eff}}}(\varphi'_t) \cos(\hat{\phi} - \varphi_0 + d_{ab}\varphi'_t - \alpha_t), \quad (\text{A73})$$

where $E_{J_t^{\text{eff}}}$ is given by Eq. (A68) with $i = t$ and

$$E_{J_t} = E_{J_a^{\text{eff}}}(\varphi'_a) + E_{J_b^{\text{eff}}}(\varphi'_b), \quad (\text{A74})$$

$$d_t = \frac{E_{J_a^{\text{eff}}}(\varphi'_a) - E_{J_b^{\text{eff}}}(\varphi'_b)}{E_{J_a^{\text{eff}}}(\varphi'_a) + E_{J_b^{\text{eff}}}(\varphi'_b)}, \quad (\text{A75})$$

$$\tan \alpha_t = d_t \tan \varphi'_t. \quad (\text{A76})$$

Therefore, by fixing the time-independent fluxes in the left and right loops such that

$$E_{J_a^{\text{eff}}}(\varphi'_a) = E_{J_b^{\text{eff}}}(\varphi'_b), \quad (\text{A77})$$

then d_t and α_t vanish in Eq. (A73). Since φ_0 is a time-independent phase, it may be ignored, leaving us with the potential

$$\hat{V} = -E_{J_t^{\text{eff}}} \cos(\varphi'_t) \cos(\hat{\phi} + d_{ab}\varphi'_t). \quad (\text{A78})$$

Crucially, the dynamic range is not affected by the static asymmetries in the Josephson energies and the time-dependent phase $d_{ab}\varphi'_t$ only leads to a small deformation of the cosine potential when the pulse is being turned on and off.

One such choice of the time-independent fluxes that satisfies Eq. (A77) is

$$\varphi_a = 2 \arctan \sqrt{\frac{1 - r_{E_J}^2}{r_{E_J}^2 - d_a^2}}, \quad (\text{A79})$$

$$\varphi_b = 0, \quad (\text{A80})$$

where $r_{E_J} = E_{J_b}/E_{J_a}$ and we have assumed $E_{J_a} > E_{J_b}$ without loss of generality. Since the right loop is now superfluous, this choice may be realised with three Josephson junctions and two external fluxes as shown in Fig. 9(b).

Assuming there is noise in the external flux so that $\varphi_a \rightarrow \varphi_a + \delta\varphi$, and expanding d_{eff} to first-order in $\delta\varphi$, yields

$$d_{\text{eff}} = \delta\varphi \frac{\sqrt{(1 - r_{E_J}^2)(r_{E_J}^2 - d_a^2)}}{(r_{E_J}^2 + 1)^2} \quad (\text{A81})$$

$$\approx \delta\varphi \frac{\sqrt{d_{ab}}}{2} \quad (\text{A82})$$

where we have expanded to leading order in the asymmetries in the final line. This shows that the dynamic range is limited by the flux noise rather than the static Josephson energy asymmetries.

Appendix B: Numerical simulations

In this appendix we explain our numerical methods used to simulate the gate. Our simulations make use of the split-operator method [51] to perform time evolution and find ground states via imaginary time evolution. In the following we explain these methods and our implementation of them. For ease of notation we set $\hbar = 1$ in this section.

1. Time evolution

We exploit the fact that there are no terms that couple position and momentum of the same mode. Considering the simple case of a single-mode Hamiltonian to begin with, the time-evolution unitary may be decomposed via a second-order Trotterisation,

$$\hat{U}(dt) = \hat{U}_x(dt/2)\hat{U}_p(dt)\hat{U}_x(dt/2) + O(dt^3), \quad (\text{B1})$$

where $\hat{U}(t) = e^{-i(\hat{H}_x + \hat{H}_p)t}$, $\hat{U}_{x/p}(dt) = e^{-i\hat{H}_{x/p}dt}$, are unitary operators for the Hamiltonian, with $\hat{H}_{x/p}$ denoting the parts of the Hamiltonian that are functions of only position/momentum operators. Time evolution may then be simulated through alternating multiplications of the unitaries $\hat{U}_x(dt)$ and $\hat{U}_p(dt)$ onto a state's wavefunction interleaved with Fourier and inverse Fourier transforms to alternate between the position and momentum bases:

$$\psi(t + dt) = \hat{U}_x(dt/2) \mathcal{F}^{-1} \hat{U}_p(dt) \mathcal{F} U_x(dt/2) \psi(t), \quad (\text{B2})$$

where $\psi(t)$ denotes the position wavefunction at time t , and \mathcal{F} and \mathcal{F}^{-1} denote the Fourier and inverse Fourier transform operators, respectively. That is, by repeated applications of the time step in Eq. (B2) the time-evolved state $\psi(t)$ may be computed from an initial state $\psi(0)$. Crucially, owing to the Fourier transforms, \hat{U}_x and \hat{U}_p are diagonal in the basis on which they act, and therefore may be represented by vectors with the same dimensions as $\psi(t)$. Moreover, by concatenating Eq. (B2), the half time-steps may be combined at intermediate times so that $N - 1$ applications of the sequence of operators

$$\hat{U}_x(dt)\mathcal{F}^{-1}\hat{U}_p(dt)\mathcal{F} \quad (\text{B3})$$

onto the state $\hat{U}_x(dt/2)\psi(0)$, with a final application of $\hat{U}_x(dt/2)\mathcal{F}^{-1}\hat{U}_p(dt)\mathcal{F}$, yields the time-evolved state $\psi(t)$ with an error of $O(dt^3) = O((t/N)^3)$.

All of the Hamiltonians considered in this manuscript are two-mode Hamiltonians with no coupling between the position and momentum of the same mode. Furthermore, the Hamiltonian for the gate with the idealised protected qubit involves no cross terms that couple position of one mode to momentum of another mode. In this case, the update rule in Eq. (B3) may be applied by casting the

vectors ψ , \hat{U}_x and \hat{U}_p into matrices, with each dimension representing position or momentum in each mode, and using a two-dimensional Fourier transform. In contrast, the interaction Hamiltonians for simulating a gate with the $0-\pi$ qubit [Eqs. (26) and (27)] involve a term that couples position of one mode to momentum of the other. In this case, the full Hamiltonian may be written as

$$\hat{H} = \sum_{i=1,2} \hat{H}_{x_i} + \hat{H}_{p_i} + \hat{H}_{x_1,p_2}, \quad (\text{B4})$$

where \hat{H}_{x_i/p_i} denotes the part of the Hamiltonian that is a function of position/momentum operators acting solely on the i -th mode, and \hat{H}_{x_1,p_2} couples the position of one mode to the momentum of the other. The Fourier transforms in each dimension must now be staggered, yielding the following modified update rule

$$\mathcal{F}_2^{-1} U_{x_1,p_2}(dt) \mathcal{F}_2 U_x(dt/2) \mathcal{F}^{-1} U_p(dt) \mathcal{F} U_x(dt/2), \quad (\text{B5})$$

for all $N - 1$ intermediate updates, with the initial and final updates given by

$$\mathcal{F}_2^{-1} \hat{U}_{x_1,p_2}(dt/2) \mathcal{F}_2, \quad (\text{B6a})$$

$$\mathcal{F}_2^{-1} \hat{U}_{x_1,p_2}(dt/2) \mathcal{F}_2 \hat{U}_x(dt/2) \mathcal{F}^{-1} \hat{U}_p(dt) \mathcal{F} \hat{U}_x(dt/2), \quad (\text{B6b})$$

respectively. Here, $\hat{U}_{x/p}(t) = e^{-i(\hat{H}_{x_1/p_1} + \hat{H}_{x_2/p_2})t}$, $\hat{U}_{x_1,p_2}(t) = e^{-i\hat{H}_{x_1,p_2}t}$, \mathcal{F} denotes the two-dimensional Fourier transform and \mathcal{F}_2 denotes the partial Fourier transform on the second mode.

2. Imaginary time evolution

For each gate simulation, we first find the ground states of the two-mode Hamiltonian by applying the split-operator method with an imaginary time-step, $dt \rightarrow -idt$, to an initial ansatz wavefunction $\psi(0)$. For the gate with the idealised qubit, this ansatz wavefunction is chosen to be

$$\psi(0) = \frac{1}{\sqrt{2}} [\mathcal{N}_{\sigma_1, \sigma_2}(0, 0) + \mathcal{N}_{\sigma_1, \sigma_2}(0, \pi)], \quad (\text{B7})$$

where $\mathcal{N}_{\sigma_1, \sigma_2}(\mu_1, \mu_2)$ denotes a two-dimensional Gaussian with standard deviations σ_1 , σ_2 and means μ_1 , μ_2 . After evolving under the Hamiltonian for sufficiently long, each Gaussian in Eq. (B7) converges to a ground state wavefunction that is localised near $x_2 = 0$ or $x_2 = \pi$, and therefore the equal superposition defines a $+1$ eigenstates of \bar{X}_m as per our subsystem decomposition (see Appendix C). Whilst the true ground state of the Hamiltonian may correspond to a different superposition of the two localised wavefunctions, for the Hamiltonians we consider, tunnelling in the x_2 direction occurs on a much longer time scale than tunnelling in the x_1 direction due to the large charging energy separation, e.g.,

$E_{C_\theta} \ll E_{C_\phi}$. Therefore, we choose a total (imaginary) evolution time that is on the order of the harmonic oscillator period in the x_1 direction. Furthermore, we choose the standard deviations σ_1, σ_2 to minimise the number of time-steps required to obtain the ground state, with $\sigma_1 \gg \sigma_2$ to reflect the charging energy separation.

When simulating the gate with the $0-\pi$ qubit, the ansatz wavefunction must be modified since position in θ corresponds to momentum in the effective mode α . We choose

$$\psi(0) = \mathcal{N}_{\sigma_1, \sigma_2}(0, 0), \quad (\text{B8})$$

which approximately corresponds to a $+1$ eigenstate of \bar{X}_{eff} when x_2 represents the position basis for the effective mode α .

Appendix C: Subsystem decomposition and diamond norm error

In this appendix we introduce a subsystem decomposition of the full Hilbert space, and derive expressions for the diamond norm error using this subsystem decomposition.

1. Subsystem decomposition

We choose a subsystem decomposition of the Hilbert space that allows us to define the qubit state based on its modular position in θ . In the context of quantum error correction, this corresponds to a particular choice of decoder. See Refs [15, 16] for similar applications of subsystem decompositions applied to the GKP code.

Under this decomposition, the full Hilbert space may be decomposed as follows

$$\mathcal{H} = \mathcal{H}_\theta \otimes \mathcal{H}_\xi = (\mathcal{H}_L \otimes \mathcal{H}_{\tilde{\theta}}) \otimes \mathcal{H}_\xi,$$

where \mathcal{H}_θ and \mathcal{H}_ξ represent the subsystems for the θ and ξ modes, with $\xi \in \{\phi, \zeta, \varphi\}$. Here we have decomposed \mathcal{H}_θ into a logical subsystem \mathcal{H}_L and a gauge subsystem $\mathcal{H}_{\tilde{\theta}}$ via the following map:

$$|\theta\rangle \rightarrow |\mu\rangle |\tilde{\theta}\rangle, \quad (\text{C1})$$

such that $\theta = \mu\pi + \tilde{\theta}$, where $\mu = 0, 1$ and $\tilde{\theta} \in [-\pi/2, \pi/2)$ [52]. In this way, we define states whose support lies in $[-\pi/2, \pi/2)$ to be $+1$ eigenstates of the Pauli- Z effective qubit operator \bar{Z}_{eff} , and states whose support lies in $[\pi/2, 3\pi/2)$ to be the -1 eigenstates of \bar{Z}_{eff} . This facilitates the following (unitary and Hermi-

tian) effective qubit operators

$$\bar{X}_{\text{eff}} = \int_{-\pi/2}^{\pi/2} d\theta |\theta\rangle_{\theta} \langle \theta + \pi| + |\theta + \pi\rangle_{\theta} \langle \theta|, \quad (\text{C2a})$$

$$\bar{Y}_{\text{eff}} = \int_{-\pi/2}^{\pi/2} d\theta -i |\theta\rangle_{\theta} \langle \theta + \pi| + i |\theta + \pi\rangle_{\theta} \langle \theta|, \quad (\text{C2b})$$

$$\bar{Z}_{\text{eff}} = \int_{-\pi/2}^{\pi/2} d\theta |\theta\rangle_{\theta} \langle \theta| - |\theta + \pi\rangle_{\theta} \langle \theta + \pi|, \quad (\text{C2c})$$

which implicitly act as the identity on the ξ -mode. Here and in what follows we use the notation $|x\rangle_x$ to represent an eigenstate of the operator \hat{x} with eigenvalue x . Using the above operators, we can define a *logical* density matrix $\hat{\rho}_L \in \mathcal{H}_L$ via

$$\hat{\rho}_L = \frac{1}{2} \left(\hat{I} + \langle \bar{X}_{\text{eff}} \rangle \hat{X} + \langle \bar{Y}_{\text{eff}} \rangle \hat{Y} + \langle \bar{Z}_{\text{eff}} \rangle \hat{Z} \right), \quad (\text{C3})$$

where $\hat{I}, \hat{X}, \hat{Y}, \hat{Z}$ are the usual 2×2 Pauli matrices, and the expectation values are taken with respect to the state in the full Hilbert space.

2. Diamond norm

To quantify the performance of the gate we use the diamond norm deviation. We use this as our primary metric instead of the average gate fidelity due to the fact that it is a worst-case estimate for the gate performance [21], and coincides with the metric used in threshold theorems [17–19]. In particular, for the case of coherent errors, which we primarily consider here, the average gate infidelity is the square of the diamond norm deviation [20]. Here we derive the expression for the diamond norm deviation, closely following the approach taken in [7].

We assume that no logical bit-flips occur during the gate, which is a valid assumption so long as $E_J \gg E_C$, in the case of the ideal qubit, or $E_J \gg E_{C_{\theta}}$ in the case of the $0-\pi$ qubit. This allows us to write an arbitrary pure state before and after the gate as

$$|\psi_{i/f}\rangle = a |0\rangle |\psi_{0,i/f}\rangle + b |1\rangle |\psi_{1,i/f}\rangle, \quad (\text{C4})$$

where a and b are two complex amplitudes satisfying $|a|^2 + |b|^2 = 1$, subscripts i and f denote initial and final states, respectively, and we have divided the Hilbert space in two, with $|\mu\rangle \in \mathcal{H}_L$ and $|\psi_{\mu,i/f}\rangle \in \mathcal{H}_{\bar{\theta}} \otimes \mathcal{H}_{\xi}$, $\mu = 0, 1$. Note that we have also absorbed the factor of $-i$ from the gate into the definition for the state $|\psi_{1,f}\rangle$. The corresponding reduced density matrices in the $|\mu\rangle$ basis are

$$\hat{\rho}_{i/f} = \begin{pmatrix} |a|^2 & ab^* \langle \psi_{1,i/f} | \psi_{0,i/f} \rangle \\ a^*b \langle \psi_{0,i/f} | \psi_{1,i/f} \rangle & |b|^2 \end{pmatrix}. \quad (\text{C5})$$

and a set of Kraus operators corresponding to the CPTP

map $\mathcal{U}_{\text{noisy}} : \hat{\rho}_i \rightarrow \hat{\rho}_f$ are as follows

$$K_0 = \sqrt{\frac{1+r}{2}} \begin{pmatrix} e^{-i\alpha/2} & 0 \\ 0 & e^{i\alpha/2} \end{pmatrix}, \quad (\text{C6a})$$

$$K_1 = \sqrt{\frac{1-r}{2}} \begin{pmatrix} e^{-i\alpha/2} & 0 \\ 0 & -e^{i\alpha/2} \end{pmatrix}, \quad (\text{C6b})$$

where $r = |\langle \psi_{0,f} | \psi_{1,f} \rangle| / |\langle \psi_{0,i} | \psi_{1,i} \rangle|$ and $\alpha = \arg \langle \psi_{0,f} | \psi_{1,f} \rangle - \arg \langle \psi_{0,i} | \psi_{1,i} \rangle$ are the relative magnitudes and phases of the inner products $\langle \psi_{0,i/f} | \psi_{1,i/f} \rangle$.

The diamond norm for a quantum operation \mathcal{E} acting on a single qubit is defined to be the trace norm of the operation extended to 2 qubits, maximised over all two-qubit states [53]

$$\|\mathcal{E}\|_{\diamond} = \frac{1}{2} \max_{\rho} \|\mathcal{E} \otimes I(\rho)\|_1. \quad (\text{C7})$$

We note that the convention used in Ref. [7] for the diamond norm is larger than our definition by a factor of 2, but we use the above definition to be consistent with more recent literature [20, 21].

For the quantum operation described by the Kraus operators in Eq. (C6), the state that maximises the norm of the extended operator $\mathcal{U}_{\text{noisy}} \otimes \mathcal{I}$ is a maximally entangled state, which we may take to be the Bell state $|\phi_+\rangle = (|00\rangle + |11\rangle) / \sqrt{2}$. Under the noisy extended operation, the Bell state gets mapped to

$$\mathcal{U}_{\text{noisy}} \otimes \mathcal{I} (|\phi_+\rangle \langle \phi_+|) = \frac{1}{2} \begin{pmatrix} 1 & 0 & 0 & re^{-i\alpha} \\ 0 & 0 & 0 & 0 \\ 0 & 0 & 0 & 0 \\ re^{i\alpha} & 0 & 0 & 1 \end{pmatrix} \quad (\text{C8})$$

and thus, the diamond norm deviation corresponds to half of the trace-norm of the matrix

$$\begin{aligned} & (\mathcal{U}_{\text{noisy}} - \mathcal{U}_{\text{ideal}}) \otimes \mathcal{I} (|\phi_+\rangle \langle \phi_+|) \\ &= \frac{1}{2} \begin{pmatrix} 0 & 0 & 0 & re^{-i\alpha} - i \\ 0 & 0 & 0 & 0 \\ 0 & 0 & 0 & 0 \\ re^{i\alpha} + i & 0 & 0 & 0 \end{pmatrix}, \quad (\text{C9}) \end{aligned}$$

which is

$$\varepsilon_{\diamond} = \frac{1}{2} \sqrt{(re^{i\alpha} + i)(re^{-i\alpha} - i)} \quad (\text{C10a})$$

$$= \frac{1}{2} \frac{|\langle \psi_{0,i} | \psi_{1,i} \rangle - i \langle \psi_{0,f} | \psi_{1,f} \rangle|}{|\langle \psi_{0,i} | \psi_{1,i} \rangle|}. \quad (\text{C10b})$$

Note that when $|\psi_{0,i}\rangle = |\psi_{1,i}\rangle$, which is the case when $\xi = \phi$ or ζ , then the diamond norm deviation reduces to

$$\varepsilon_{\diamond} = \frac{1}{2} |1 - i \langle \psi_{0,f} | \psi_{1,f} \rangle|. \quad (\text{C11})$$

This coincides with the half of the trace distance between the final state from the noisy gate and the final state from an ideal gate.

To compute the diamond norm deviation numerically, we choose $a = b = 1/\sqrt{2}$ in Eq. (C4) and observe that

$$\bar{\theta}\langle\tilde{\theta}|\psi_{0,i/f}\rangle = \sqrt{2}\langle\tilde{\theta}|\psi_{i/f}\rangle \quad (\text{C12a})$$

$$\bar{\theta}\langle\tilde{\theta}|\psi_{1,i/f}\rangle = \sqrt{2}\langle\tilde{\theta} + \pi|\psi_{i/f}\rangle. \quad (\text{C12b})$$

Using this, we can compute the inner product as follows

$$\langle\psi_{0,i/f}|\psi_{1,i/f}\rangle = \int_{-\pi/2}^{\pi/2} d\tilde{\theta} \langle\psi_{0,i/f}|\tilde{\theta}\rangle_{\bar{\theta}}\langle\tilde{\theta}|\psi_{1,i/f}\rangle \quad (\text{C13a})$$

$$= 2 \int_{-\pi/2}^{\pi/2} d\theta \langle\psi_{i/f}|\theta\rangle_{\theta}\langle\theta + \pi|\psi_{i/f}\rangle \quad (\text{C13b})$$

$$= \langle\psi_{i/f}|\left(\int_{-\pi/2}^{\pi/2} d\theta |\theta\rangle_{\theta}\langle\theta + \pi|\right)|\psi_{i/f}\rangle \quad (\text{C13c})$$

$$= \langle\bar{X}_{\text{eff}}\rangle_{i/f} + i\langle\bar{Y}_{\text{eff}}\rangle_{i/f}, \quad (\text{C13d})$$

where $\langle\cdot\rangle_{i/f} = \langle\psi_{i/f}|\cdot|\psi_{i/f}\rangle$. This leads to the following expression for the diamond norm deviation in terms of the logical operators

$$\varepsilon_{\diamond} = \frac{1}{2}\sqrt{\frac{(\langle\bar{X}_{\text{eff}}\rangle_i + \langle\bar{Y}_{\text{eff}}\rangle_f)^2 + (\langle\bar{Y}_{\text{eff}}\rangle_i - \langle\bar{X}_{\text{eff}}\rangle_f)^2}{\langle\bar{X}_{\text{eff}}\rangle_i^2 + \langle\bar{Y}_{\text{eff}}\rangle_i^2}}. \quad (\text{C14})$$

When $|\psi_{i,0}\rangle = |\psi_{i,1}\rangle$, then $\langle\bar{X}_{\text{eff}}\rangle_i = 1$ and $\langle\bar{Y}_{\text{eff}}\rangle_i = 0$, and the diamond norm deviation reduces to

$$\varepsilon_{\diamond} = \frac{1}{2}\sqrt{(1 + \langle\bar{Y}_{\text{eff}}\rangle_f)^2 + \langle\bar{X}_{\text{eff}}\rangle_f^2}. \quad (\text{C15})$$

a. Comparison to average gate fidelity

To compare with the average gate fidelity, we compute the latter in terms of the effective qubit operator expectation values. The average gate fidelity in the logical subsystem is [54]

$$\begin{aligned} \bar{\mathcal{F}} &= \frac{1}{2} + \\ &\frac{1}{12} \left\{ \text{Tr}[\hat{S}^\dagger \hat{X} \hat{S} \mathcal{E}(|0\rangle\psi_{0,i}\langle\psi_{1,i}|1\rangle + |1\rangle\psi_{1,i}\langle\psi_{0,i}|0\rangle)] \right. \\ &+ \text{Tr}[\hat{S}^\dagger \hat{Y} \hat{S} \mathcal{E}(-i|0\rangle\psi_{0,i}\langle\psi_{1,i}|1\rangle + i|1\rangle\psi_{1,i}\langle\psi_{0,i}|0\rangle)] \\ &\left. + \text{Tr}[\hat{S}^\dagger \hat{X} \hat{S} \mathcal{E}(|0\rangle\psi_{0,i}\langle\psi_{0,i}|0\rangle + |1\rangle\psi_{1,i}\langle\psi_{1,i}|1\rangle)] \right\}, \end{aligned} \quad (\text{C16})$$

where \hat{S} denotes the standard phase gate in the logical subsystem and \mathcal{E} represents the composition of the time-evolution unitary operation with the quantum operation that maps a state in the full Hilbert space into the logical Hilbert space via Eq. (C3). Using Eq. (C3) and comput-

ing the traces, this expression becomes

$$\begin{aligned} \bar{\mathcal{F}} &= \frac{1}{2} + \\ &\frac{1}{12} \left(i\langle\psi_{0,f}|\langle 0|\bar{X}_{\text{eff}}|1\rangle|\psi_{1,f}\rangle - i\langle\psi_{1,f}|\langle 1|\bar{X}_{\text{eff}}|0\rangle|\psi_{0,f}\rangle \right. \\ &- \langle\psi_{0,f}|\langle 0|\bar{Y}_{\text{eff}}|1\rangle|\psi_{1,f}\rangle - \langle\psi_{1,f}|\langle 1|\bar{Y}_{\text{eff}}|0\rangle|\psi_{0,f}\rangle \\ &\left. + \langle\psi_{0,f}|\langle 0|\bar{Z}_{\text{eff}}|0\rangle|\psi_{0,f}\rangle - \langle\psi_{1,f}|\langle 1|\bar{Z}_{\text{eff}}|1\rangle|\psi_{1,f}\rangle \right). \end{aligned} \quad (\text{C17})$$

Using the definition of the effective qubit operators, this simplifies to

$$\bar{\mathcal{F}} = \frac{2}{3} + \frac{i}{6} (\langle\psi_{0,f}|\psi_{1,f}\rangle - \langle\psi_{1,f}|\psi_{0,f}\rangle). \quad (\text{C18})$$

Finally, using Eq. (C13d), the gate infidelity may be written as

$$1 - \bar{\mathcal{F}} = \frac{1}{3} (1 + \langle\bar{Y}_{\text{eff}}\rangle_f), \quad (\text{C19})$$

where the expectation value is taken with respect to the final state in Eq. (C4) with $a = b = 1/\sqrt{2}$. Comparing with Eq. (C15), we see that the gate infidelity differs from the diamond norm deviation in that it does not account for non-zero $\langle\bar{X}_{\text{eff}}\rangle_f$, and it is smaller by a factor of 2/3.

b. Extension to arbitrary Z-rotations

The expression for the diamond norm deviation may be easily generalised to the case where the ideal operation corresponds to an arbitrary rotation, θ , about the Z -axis by replacing $-i \rightarrow e^{-i\theta}$ in Eq. (C10b). In particular, in the case of a T -gate using an ancillary oscillator, as considered in Appendix D5, we have $\theta = \pi/4$ and $\xi = \phi$. Using Eq. (C13d), the expression for the diamond norm deviation becomes

$$\varepsilon_{\diamond} = \frac{1}{2} |1 + e^{-i\pi/4} \langle\bar{X}_{\text{eff}}\rangle_f + e^{i\pi/4} \langle\bar{Y}_{\text{eff}}\rangle_f|. \quad (\text{C20})$$

Appendix D: Additional analysis and extensions of the protected gate

In this appendix we give additional analysis and extensions of the protected gate discussed in the main text. In Appendix D1 we give analytical justification for the gate's protection and the optimal ancilla impedance. In Appendices D2 and D3 we analyse the effects of varying the ramp time, and the charging energy ratio on the performance of the gate, respectively. In Appendices D4 and D5 we investigate using the internal φ -mode of the 0- π qubit to perform a protected gate, and an extension of the protected phase gate to a protected T -gate, respectively.

1. Analytical justification for the gate's protection and optimal ancilla impedance

Here we give analytical justification for the protection of the gate and explain why there is an optimal ancilla impedance for a given mistiming error. Our approach follows a similar line of analysis to Refs. [7, 55]. We consider the case of an ideal qubit coupled to an external oscillator. To simplify the analysis, we neglect the errors that occur due to the finite ramp time in the pulse and only consider the part of the gate when the pulse is on [point (ii) to (iii) in Fig. 2]. Furthermore, we consider only the finite width of the Gaussian envelope in the GKP states of the oscillator and disregard the non-zero width of each peak. To this end, the states in the oscillator may be approximated as a superposition of ϕ -eigenstates at the centre of each cosine well, with amplitudes weighted by an envelope parameter κ :

$$|\tilde{\mu}\rangle = \frac{1}{\mathcal{N}_\mu} \sum_{n \in \mathbb{Z}} e^{-\kappa\pi(n+\mu/2)^2} |(n+\mu/2)2\pi\rangle_\phi, \quad (\text{D1})$$

where \mathcal{N}_μ are normalisation factors given by

$$\mathcal{N}_\mu^2 = \sum_{n \in \mathbb{Z}} e^{-2\pi\kappa(n+\mu/2)^2}, \quad (\text{D2})$$

and $\mu = 0, 1$ labels the qubit state. In the limit that $\kappa \rightarrow \infty$ these become ± 1 eigenstates of the logical operator \bar{Z}_ϕ and $+1$ eigenstates of the stabilisers \hat{S}_{X_ϕ} and \hat{S}_{Z_ϕ} . We now consider the evolution of these states under a noisy version of the ideal unitary,

$$\hat{S}_\eta = e^{i(1+\eta)\hat{\phi}^2/2\pi}, \quad (\text{D3})$$

where η corresponds to a dimensionless overrotation in the gate. Under this operation, the states evolve to

$$\hat{S}_\eta |\tilde{\mu}\rangle = \frac{i^\mu}{\mathcal{N}_\mu} \sum_{n \in \mathbb{Z}} e^{-2\pi(\kappa/2 - i\eta)(n+\mu/2)^2} |2\pi(n+\mu/2)\rangle_\phi. \quad (\text{D4})$$

Since the states $\hat{S}_\eta |\tilde{\mu}\rangle$ are orthogonal, we cannot use their overlap to estimate the gate error. Instead, we directly estimate their relative phase,

$$\begin{aligned} \frac{\langle \tilde{1} | \hat{S}_\eta | \tilde{1} \rangle}{\langle \tilde{0} | \hat{S}_\eta | \tilde{0} \rangle} &= i \left(\frac{\sum_{n \in \mathbb{Z}} e^{-2\pi\kappa n^2}}{\sum_{n \in \mathbb{Z}} e^{-2\pi\kappa(n+1/2)^2}} \right) \\ &\times \left(\frac{\sum_{n \in \mathbb{Z}} e^{-2\pi(\kappa - i\eta)(n+1/2)^2}}{\sum_{n \in \mathbb{Z}} e^{-2\pi(\kappa - i\eta)n^2}} \right). \end{aligned} \quad (\text{D5})$$

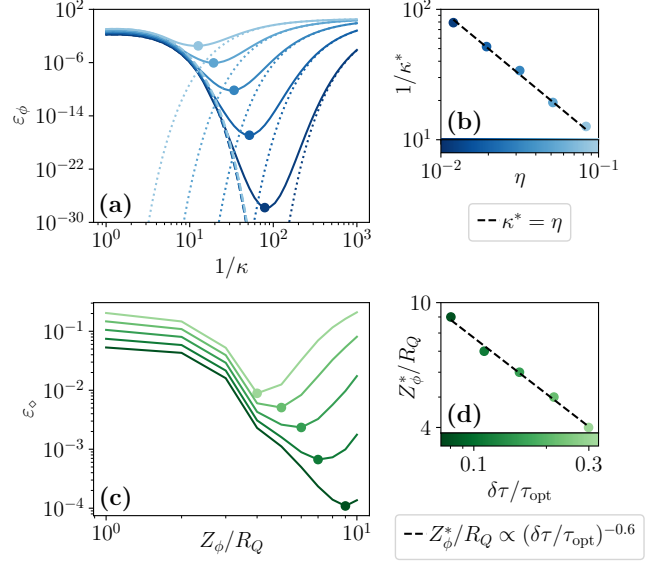


FIG. 10. Optimal oscillator impedance. (a) Relative phase error defined in Eq. (D8a) as a function of the envelope parameter κ for different overrotation errors η . The circles denote the optimal envelope parameter κ^* and the dotted (dashed) curves show the asymptotic scalings given in Eq. (D8c) for $\kappa \ll \eta \ll 1$ ($\eta \ll \kappa \ll 1$). (b) The optimal envelope parameter as a function of the overrotation error η . The black dashed line denotes $\kappa^* = \eta$. (c) Gate errors as a function of oscillator impedance for different mistiming errors $\delta\tau$. The circles denote the optimal oscillator impedance Z_ϕ^* . (d) Optimal oscillator impedance as a function of the mistiming error. The black dashed line denotes a power-law fit to the data.

Using the Poisson summation formula, the sums may be rewritten over their frequency components, resulting in

$$\begin{aligned} \frac{\langle \tilde{1} | \hat{S}_\eta | \tilde{1} \rangle}{\langle \tilde{0} | \hat{S}_\eta | \tilde{0} \rangle} &= i \left(\frac{\sum_{k \in \mathbb{Z}} e^{-\frac{\pi}{2\kappa} k^2}}{\sum_{k \in \mathbb{Z}} (-1)^k e^{-\frac{\pi}{2\kappa} k^2}} \right) \\ &\times \left(\frac{\sum_{k \in \mathbb{Z}} (-1)^k e^{-\frac{\pi}{2(\kappa - i\eta)} k^2}}{\sum_{k \in \mathbb{Z}} e^{-\frac{\pi}{2(\kappa - i\eta)} k^2}} \right). \end{aligned} \quad (\text{D6})$$

Assuming both the overrotation error η and the envelope parameter κ to be small facilitates the truncation of each sum to the leading order corrections $k = \pm 1$:

$$\frac{\langle \tilde{1} | \hat{S}_\eta | \tilde{1} \rangle}{\langle \tilde{0} | \hat{S}_\eta | \tilde{0} \rangle} \approx i \left(\frac{1 + 2e^{-\frac{\pi}{2\kappa}}}{1 - 2e^{-\frac{\pi}{2\kappa}}} \right) \left(\frac{1 - 2e^{-\frac{\pi}{2(\kappa - i\eta)}}}{1 + 2e^{-\frac{\pi}{2(\kappa - i\eta)}}} \right) \quad (\text{D7a})$$

$$\approx i(1 + 4e^{-\frac{\pi}{2\kappa}} - 4e^{-\frac{\pi}{2(\kappa - i\eta)}}), \quad (\text{D7b})$$

where we have expanded to first order in $e^{-1/\kappa}$ and $e^{-1/\eta}$ in the final line.

The gate error may then be approximated by the deviation of this relative phase from its ideal value of i ,

$$\varepsilon_\phi = \left| i - \frac{\langle \hat{1} | \hat{S}_\eta | \hat{1} \rangle}{\langle \hat{0} | \hat{S}_\eta | \hat{0} \rangle} \right| \quad (\text{D8a})$$

$$\approx \left| 4e^{-\frac{\pi}{2\kappa}} - 4e^{-\frac{\pi}{2(\kappa-i\eta)}} \right| \quad (\text{D8b})$$

$$\sim \begin{cases} 4e^{-\frac{\pi\kappa}{2\eta^2}} & \text{for } \kappa \ll \eta \ll 1 \\ \frac{2\pi\eta}{\kappa^2} e^{-\frac{\pi}{2\kappa}} & \text{for } \eta \ll \kappa \ll 1 \end{cases}, \quad (\text{D8c})$$

where \sim in the final line denotes the asymptotic scaling of this error as a function of κ . Since the first of these exponentials decays with increasing κ , whilst the second grows with increasing κ , these scalings imply an optimal envelope parameter of $\kappa = \eta$ for a given overrotation η . In Figs. 10(a) and 10(b) we confirm these scalings and the existence of this optimal envelope parameter by plotting this error as a function of the envelope parameter κ for different overrotations η . Here we find that the optimal envelope is given by $\kappa = \eta$. Crucially, Eq. (D8c) and Fig. 10(a) also show that the phase error is exponentially suppressed in $1/\kappa$ when $\eta \ll \kappa \ll 1$, owing to the protection of the gate.

To compare this approximate analysis with the full behaviour of the gate we plot the gate errors from Fig. 3(a) as a function of the oscillator impedance at different pulse mistimings in Fig. 10(c). Similarly to Fig. 10(a) we observe an optimal impedance for a given pulse mistiming. This is because the envelope of the GKP states is inherited from the ground state of the oscillator, whose variance is controlled by the impedance; if the envelope parameter of the GKP states is exactly given by the variance of the ground state, then $\kappa = R_Q/Z_\phi$. Figure 10(d) shows the optimal oscillator impedance as a function of the pulse mistiming. A fit to the data reveals that $Z_\phi^*/R_Q \propto (\delta\tau/\tau_{\text{opt}})^{-0.6}$, which is similar to the scaling expected from the envelope parameter inherited from the ground state of the oscillator, $\kappa = R_Q/Z_\phi$. The optimal impedance for a given mistiming error implies an optimal impedance for a given gate error threshold, explaining the maxima in the gate robustness as a function of the oscillator impedance observed in Fig. 3(c).

2. Impact of variations in the pulse ramp-time on the performance of the gate

In this section we examine the impact of varying the ramp-time τ_J on the performance of the gate. As discussed in the main text, the rise time is chosen to be approximately equal to an oscillator period, $\tau_J \approx \hbar/\sqrt{8E_{C_\phi}E_{L_\phi}}$, to ensure that the evolution remains adiabatic with respect to the envelope inherited from the oscillator, but fast enough to prevent the wavefunction from collapsing into a single cosine well. However, just as the gate is insensitive to variations in the precise wait-time τ , it is also expected to be insensitive to variations in this rise time. Here we verify this numerically.

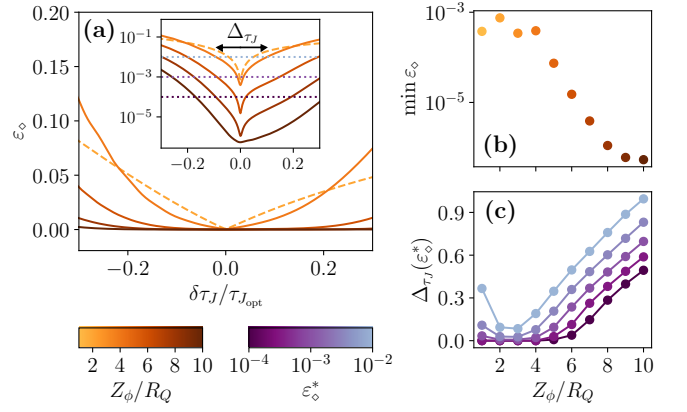


FIG. 11. Gate errors as a function of ramp-time. (a) Gate error ε_ϕ as a function of deviations in the pulse ramp-time $\delta\tau_J$, where $\delta\tau_J$ is given by Eq. (D9), calculated for different values of the oscillator impedance Z_ϕ . Protected gates are marked in solid lines whereas the dashed line denotes an unprotected gate. Inset: identical data on a log-linear plot. Dotted lines correspond to threshold gate errors ε_ϕ^* for (c). (b) Gate imprecision as a function of Z_ϕ . (c) Gate robustness as a function of Z_ϕ . For these simulations, $E_{C_\phi}/E_C = 100$, $E_J/E_{C_\phi} = 1$, $E_{J_{\min}} = 0$, $E_{J_{\max}}/E_{C_\phi} = 100$ and $\tau = \tau_{\text{opt}}$.

Figure 11 shows analogous results to Figs. 3(a) to 3(c), where we have defined

$$\delta\tau_J = \tau_J - \tau_{J_{\text{opt}}}, \quad (\text{D9})$$

analogously to Eq. (15). The error curves in Fig. 11(a) are very similar in appearance to those in Fig. 3(a), whereby the gate error increase linearly with $\delta\tau_J$ for low oscillator impedances (dashed line), and are flat near $\delta\tau_J = 0$ suppressed for higher oscillator impedances (solid lines). The imprecision shown in Fig. 11(b) is identical to that shown in Fig. 3(b) since the parameters achieved at the minimal gate error are the same in both cases. The most notable difference is in the robustness, where we observe the gate to be more robust to relative imperfections in the ramp-time than the wait-time. In particular, for the range of impedances considered here, the robustness parameter $\Delta\tau_J$ does not reach its maximum value for the same thresholds ε_ϕ^* considered in Fig. 3(c), with values as large as $\Delta\tau_J(0.01) = 0.995$ achieved. This is in contrast to Fig. 3(c) where the optimal impedances for the same error thresholds were $Z_\phi/R_Q \leq 10$, with a maximum robustness of $\Delta\tau_J(0.01) = 0.55$.

3. Impact of charging energy ratio on the performance of the gate

Here we analyse the impact of the charging energy ratio on the performance of the gate. Specifically, in Appendix D 3a we analyse the impact of varying E_{C_ϕ}/E_C

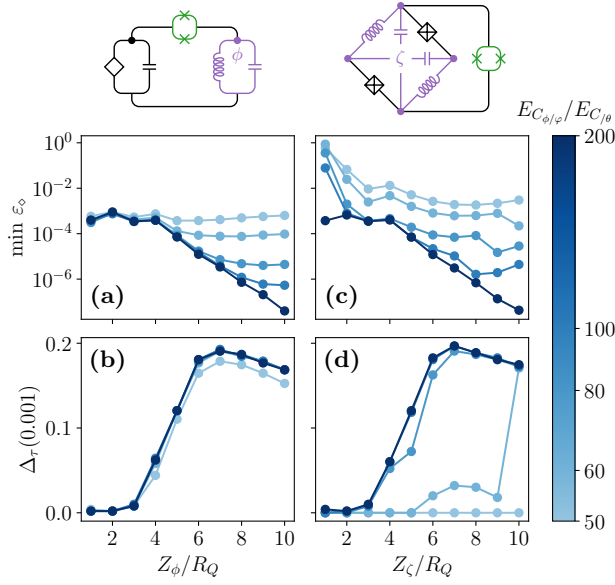


FIG. 12. Impact of charging energy ratio on the performance of protected phase gates. (a) Imprecision and (b) robustness of a gate for an ideal qubit coupled to an external oscillator as a function of the oscillator impedance Z_ϕ , at different values of the charging energy ratio E_{C_ϕ}/E_C . (c) Imprecision and (d) robustness of a gate for a $0-\pi$ qubit using its internal ζ mode as a function of the ζ -mode impedance Z_ζ , at different values of the charging energy ratio E_{C_ϕ}/E_{C_θ} . Throughout all simulations, the minimal and maximal coupling strengths have been fixed to $E_{J_{\min}} = 0$ and $E_{J_{\max}}/E_{C_{\phi/\varphi}} = 100$, and in panels (a) and (b) $E_J/E_{C_\phi} = 1$. The circuit diagrams corresponding to each version of the gate are shown above each column.

on the performance of the gate for the ideal qubit coupled to an external oscillator and in Appendix D 3 b we analyse the impact of varying E_{C_ϕ}/E_{C_θ} on the performance of the gate for the $0-\pi$ qubit using its internal ζ mode.

a. Ideal qubit coupled to an external oscillator

Figures 12(a) and 12(b) shows the imprecision and robustness for a gate with an ideal qubit coupled to an external oscillator as a function of the oscillator impedance at different values of the charging energy ratio E_{C_ϕ}/E_C . The data at $E_{C_\phi}/E_C = 100$ corresponds to the same data as in Figs. 3(b) and 3(c) at $\varepsilon_\phi^* = 10^{-3}$, as a point of comparison. Figure 12(a) shows that the value of the oscillator impedance at which the imprecision plateaus increases with the charging energy ratio E_{C_ϕ}/E_C . In particular, for $E_{C_\phi}/E_C = 200$ this critical value is larger than $Z_\phi/R_Q = 10$, the largest value considered here. Therefore, E_{C_ϕ}/E_C sets the error floor for the gate assuming an arbitrarily large oscillator impedance can be obtained. Figure 12(b) shows that despite the decrease in precision with smaller E_{C_ϕ}/E_C , the robustness remains

largely unaffected for all $E_{C_\phi}/E_C \geq 50$.

b. $0-\pi$ qubit using its internal harmonic mode

Here we investigate the impact of varying the largest charging energy ratio in the $0-\pi$ qubit, E_{C_ϕ}/E_{C_θ} , on the performance of the gate when using its internal ζ mode. Figures 12(c) and 12(d) show the imprecision and robustness as a function of the impedance of the ζ mode for different charging energy ratios E_{C_ϕ}/E_{C_θ} . Similarly to the case of the ideal qubit coupled to an oscillator, we find that larger charging energy ratios improve the performance of the gate. This is due to the fact that the nearest-neighbour tunnelling term in Eq. (22) is exponentially suppressed relative to the next-nearest-neighbour tunnelling term in E_{C_ϕ}/E_{C_θ} [see Fig. 4(c)].

Comparing to Figs. 12(a) and 12(b) shows that nearly identical performance to the case of the ideal qubit coupled to an oscillator can be recovered at a charging energy ratio of $E_{C_\phi}/E_{C_\theta} = 200$. The results also reveal that a minimum value of $E_{C_\phi}/E_{C_\theta} = 60$ is required for a protected gate. However, at this charging energy ratio, a ζ -mode impedance of $Z_\zeta/R_Q = 10$ is required to obtain appreciable robustness, which corresponds to a φ -mode impedance of $Z_\varphi/R_Q = 77$, where $Z_\varphi = \sqrt{L/4C_J}$. This exceeds the minimal φ -mode impedance of $Z_\varphi/R_Q = 50$ required for a protected gate at a charging energy ratio of $E_{C_\phi}/E_{C_\theta} = 100$. Therefore, reducing the charging energy ratio does not lead to a smaller critical Z_φ to obtain a protected gate.

4. Using the internal φ mode of the $0-\pi$ qubit for a gate

Here we investigate the possibility of using the internal φ mode of the $0-\pi$ qubit to perform a protected gate. Unlike the ζ mode, the internal φ mode is already coupled to the θ mode. Therefore, in order to utilise the φ mode in place of the ancillary oscillator, each of the static Josephson junctions in the $0-\pi$ qubit must be replaced with a tunable Josephson element, and threaded with equal external fluxes; the inset of Fig. 13(b) shows the circuit diagram and in Appendix A 4 we provide the circuit quantisation.

To simulate the gate using this internal mode, we use Eq. (16) with $2E_J \rightarrow E_{J_{\text{int}}}(t)$ and $\varphi_{\text{ext}} = 0$. This means the interaction term now becomes

$$\hat{H}_{\text{int}}(t) = -E_{J_{\text{int}}}(t) \cos \hat{\theta} \cos \hat{\varphi}, \quad (\text{D10})$$

which differs from the interaction term for the ancillary oscillator [Eq. (7)] by $-E_{J_{\text{int}}}(t) \sin \hat{\theta} \sin \hat{\varphi}$. As explained in Section IV A, this additional potential does not change the location of the minima in $\theta-\varphi$ space, resulting in a similar potential. However, the interaction strength now also affects the qubit, whereby a small $E_{J_{\text{int}}}$ leads to increased tunnelling between the two qubit states. On the

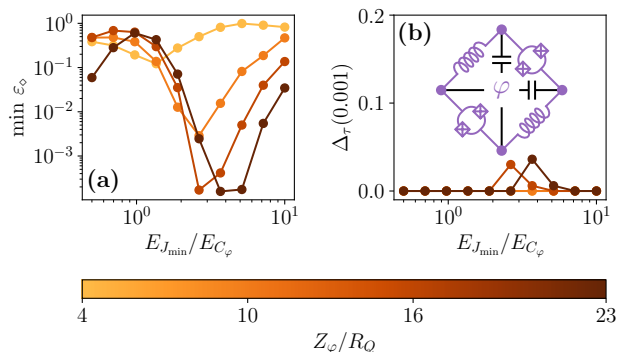


FIG. 13. Gate errors for a phase gate with the $0-\pi$ qubit using its internal ϕ mode. (a) Imprecision and (b) robustness of the gate as a function of the impedance of the ϕ mode Z_ϕ , for different minimal coupling strength $E_{J_{\min}}/E_{C_\phi}$. The charging energy ratio is fixed to $E_{C_\phi}/E_{C_\theta} = 100$, and the maximal coupling strength to $E_{J_{\max}}/E_{C_\phi} = 100$. The inset of panel (b) shows the circuit diagram for the gate.

other hand, the results of Section II C 2 showed that a small initial coupling strength is necessary for protection of the gate. In the following we investigate the performance of the gate as a function of the minimal coupling strength $E_{J_{\min}}$. Note that because the ϕ wavefunction is different for the $|0\rangle$ and $|1\rangle$ states, the definition of the gate error must be modified from Eq. (14) to include expectation values of the effective qubit oscillators in the initial state; in Appendix C 2 we provide the exact expression.

Figure 13 shows the performance of the gate as a function of $E_{J_{\min}}$. In Fig. 13(a) we find optimal values of $E_{J_{\min}}$, which minimise the imprecision. These optimal values increase with increasing impedance, but the minimal imprecision begins to saturate for $Z_\phi/R_Q \geq 16$. Figure 13(b) shows that the gate remains nearly unprotected, with a maximal robustness of $\Delta_\tau < 4\%$ observed over all impedances and $E_{J_{\min}}$ values considered here. The lack of protection is because the optimal values of $E_{J_{\min}}/E_{C_\phi}$ observed in Fig. 13(a) are greater than unity, which exceeds the maximum value of $E_{J_{\min}}/E_{C_\phi}$ required for a protected gate found in Section II C 2; there we found that $E_{J_{\min}}/E_{C_\phi} < 0.08$ for a protected gate.

One way to decrease the tunnelling between the two qubit states whilst maintaining a sufficiently low $E_{J_{\min}}/E_{C_\phi}$ for a protected gate is to increase the ratio of E_{C_ϕ}/E_{C_θ} . However, given that current experiments [9, 11] have yet to reach the value of E_{C_ϕ}/E_{C_θ} considered here ($E_{C_\phi}/E_{C_\theta} = 100$), obtaining a protected gate in this way is likely to be challenging.

Whilst we have considered using the ϕ mode to perform a gate analogously to the Brooks-Kitaev-Preskill gate, an alternative way of utilising the ϕ mode to perform a gate is to tune a single Josephson junction in the $0-\pi$ qubit, as proposed in Ref. [11]. This tunes the barrier

height in the $\theta + \phi$ direction, allowing tunnelling to occur between the two qubit states and implementing a rotation about the X axis. The benefit of this approach is that it eliminates the need to tune two tunable Josephson elements symmetrically, but the gate is manifestly unprotected due to removing the tunnel barrier entirely. A comprehensive simulation of this gate and comparison to the unprotected gate here would be an interesting direction for future work.

5. A protected T-gate

Here we investigate a possible extension of the protected S -gate to a protected T -gate. The basic idea is that the quadratic potential in Eq. (6) is replaced with a different potential such that a T -gate is performed on the GKP codewords.

In Ref. [13], the unitary gate

$$\hat{U} = \exp \left[-i2\pi \left(\frac{\hat{x}^3}{4} + \frac{\hat{x}^2}{8} - \frac{\hat{x}}{4} \right) \right], \quad (\text{D11})$$

where $\hat{x} = \hat{\phi}/\pi$ is suggested as a way to perform a logical T -gate on GKP codewords. Therefore, by replacing the quadratic potential in Eq. (6) with the cubic potential

$$V(x) = V_0 \left(\frac{x^3}{4} + \frac{x^2}{8} - \frac{x}{4} \right) \quad (\text{D12})$$

and turning on the interaction for a time $\tau \approx 2\pi\hbar/V_0$, a T -gate will be enacted on the qubit states. In this context, odd-ordered potentials are problematic since they are non-confining, meaning that there will be no well-defined ground state of the ancillary mode. However, the polynomial in Eq. (D12) is not unique for enacting a logical T -gate. In particular, recent work [40] has shown that the following quartic polynomial potential also realises a T -gate on the GKP code

$$V(x) = V_0 \left(\frac{x^2}{6} - \frac{x^4}{24} \right). \quad (\text{D13})$$

This can be seen to enact a phase of $e^{i\mu\pi/4}$ on the GKP codestates $|\bar{\mu}\rangle$, with $\mu = 0, 1$ by letting $x = 2n + \mu$, with n an integer, and observing that $4x^2 - x^4 = 3\mu \pmod{24}$. Thus, $\exp[i2\pi\hat{V}(\hat{x})/V_0]|\bar{\mu}\rangle = e^{i\mu\pi/4}|\bar{\mu}\rangle$.

Higher-order potentials such as the quartic potential in Eq. (D13) may be realised by flux-pumping a superconducting nonlinear asymmetric inductive element (SNAIL) oscillator [41–43]. Therefore, in order to engineer this protected T -gate, the linear oscillator in Fig. 2(a) would be replaced with a SNAIL oscillator. We do not give a detailed analysis of the experimental requirements here, but note that engineering the precise coefficients in Eq. (D13) would be an additional challenge.

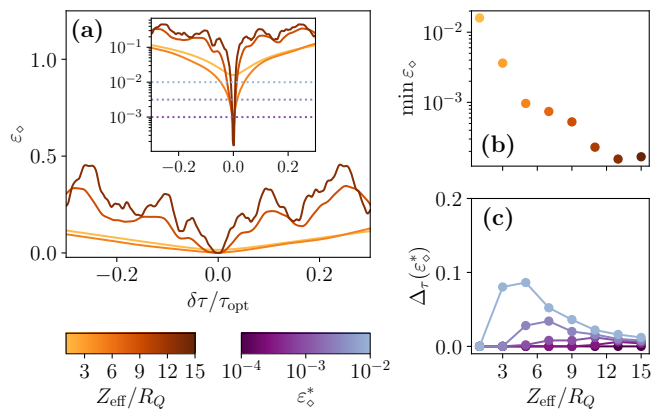


FIG. 14. Gate errors for a T -gate using a quartic potential. (a) Gate error ε_∞ as a function of deviations in the pulse wait-time $\delta\tau$, calculated for different values of the effective impedance Z_{eff} , where Z_{eff} is defined in Eq. (D15). Inset: identical data on a log-linear plot. Dotted lines correspond to threshold gate errors ε_∞^* for (c). (b) Gate imprecision as a function of Z_{eff} . (c) Gate robustness as a function of Z_{eff} . For these simulations, $E_{C_\phi}/E_C = 100$, $E_J/E_{C_\phi} = 1$, and in panels (a) – (c) $E_{J_{\text{min}}} = 0$ and $E_{J_{\text{max}}}/E_{C_\phi} = 100$

To simulate this gate for an ideal qubit coupled to the SNAIL oscillator, we use the Hamiltonian $\hat{H}(t) = \hat{H}_\theta + \hat{H}_\phi + \hat{H}_{\text{int}}(t)$, where the first and last terms are given by Eqs. (3) and (7) respectively, and the second term is given by

$$\hat{H}_\phi = 4E_{C_\phi}\hat{n}_\phi^2 + V_0 \left(\frac{\hat{\phi}^4}{24\pi^4} - \frac{\hat{\phi}^2}{6\pi^2} \right). \quad (\text{D14})$$

We define an effective impedance Z_{eff} as function of V_0 as follows

$$\frac{Z_{\text{eff}}}{R_Q} = \left(\frac{24E_{C_\phi}}{V_0} \right)^{1/4}, \quad (\text{D15})$$

which ensures that $V(\phi) = E_{C_\phi}$ at approximately the same value of ϕ as for the inductive potential with an inductance $L = Z_{\text{eff}}^2 C_\phi$. This means that the ground-state wavefunction of Eq. (D14) will have a similar expectation value with the GKP stabiliser \hat{S}_{X_ϕ} as the ground-state of a linear oscillator with an impedance of Z_{eff} . The definition of the gate error must also be modified due to the different logical gate. In Appendix C2, we give the modification.

Figure 14 shows the gate errors for a range of different effective impedances. As in Section II C 1, we use a charging energy ratio of $E_{C_\phi}/E_{C_\theta} = 100$, a protected qubit Josephson energy of $E_J/E_{C_\phi} = 1$, and minimum and maximum Josephson couplings of $E_{J_{\text{min}}} = 0$ and $E_{J_{\text{max}}}/E_{C_\phi} = 100$. The result shows that the imprecision saturates just above 10^{-4} , and that the robustness does not exceed 10% over all effective impedances and threshold gate errors. These values are roughly 2 orders

of magnitude and a factor of 8 worse than for the analogous S -gate results in Figs. 3(a) to 3(c), respectively. The worse performance of the T -gate may be attributed to the fact that unitary operations constructed from quadratic potentials are fault-tolerant for the GKP code, whereas higher-order potentials are not [13]. Nonetheless, this provides a way to obtain an unprotected non-Clifford gate that does not explicitly break the protection of the qubit since the quartic potential.

Appendix E: The $0-\pi$ qubit

In this appendix we give supplementary information for the $0-\pi$ qubit. In Appendix E1 we analyse the optimal Josephson energy for the $0-\pi$ qubit, and in Appendix E2 we give details on the effective model for the $0-\pi$ qubit.

1. Optimal Josephson energy

Here we analyse the optimal Josephson energy for a $0-\pi$ qubit. This is also analysed in Ref. [8] but here we perform our own analysis to be consistent with the parameters and notation used in this work. For fixed C , C_J and L (equivalently fixed $E_{C_\varphi}/E_{C_\theta}$ and Z_ζ/R_Q) in the $0-\pi$ qubit, there is an optimal Josephson energy E_J that maximises the protection of the $0-\pi$ qubit. This is for the following reason. On the one hand, a larger E_J raises the tunnel barrier in the θ direction, suppressing the tunnelling between the two qubit states localised at $\theta = 0$ and $\theta = \pi$, resulting in a longer lifetime. On the other hand, increasing E_J simultaneously raises the tunnel barrier in the φ direction, leading to more localised qubit state wavefunctions that are more susceptible to flux-noise induced dephasing. Thus, there is an optimal E_J , which balances out these two competing effects.

To quantify the protection of the qubit, we compute its degeneracy, defined as [8]

$$D = \frac{\log_{10}(E_2 - E_0)}{\log_{10}(E_1 - E_0)}, \quad (\text{E1})$$

where E_i denotes the i -th energy of the $0-\pi$ qubit. Note that at the flux sweetspot $\varphi_{\text{ext}} = \pi$, the degeneracy of the qubit is maximised in the $E_J \rightarrow \infty$ limit since the potential energy minima at $\theta = 0$ and $\theta = \pi$ take the same value. However, away from this exact value, the coherence time suffers from very large E_J . Therefore, we fix $\varphi_{\text{ext}} = 0$ to find the optimal E_J for dephasing protection due to highly localised wavefunctions.

Figure 15(a) shows the degeneracy of the qubit as a function of E_J and Z_ζ/R_Q with a fixed charging energy ratio of $E_{C_\varphi}/E_{C_\theta} = 100$. Here we see that there are clear optimal values of E_J that maximise the degeneracy of the qubit. In Fig. 15(b), we plot these optimal values E_J^* as a function of Z_ζ . We find that the square root of these optimal values scales logarithmically with the

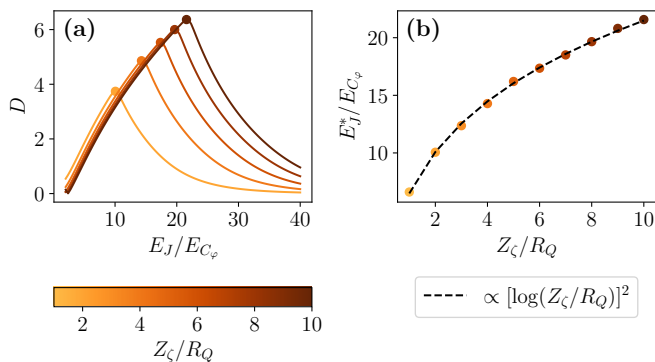


FIG. 15. Optimal Josephson energy for the 0- π qubit. (a) Degeneracy of the 0- π qubit as a function of E_J and Z_ζ for a fixed charging energy ratio of $E_{C_\varphi}/E_{C_\theta} = 100$ and $\varphi_{\text{ext}} = 0$. (b) The value of E_J that maximises the degeneracy as a function of Z_ζ . The black dashed line shows a fit to the data via Eq. (E2).

ζ -mode impedance,

$$\sqrt{E_J^*/E_{C_\varphi}} \sim \log(Z_\zeta/R_Q), \quad (\text{E2})$$

which is consistent with the results in Ref. [8]. These optimal values are used to determine E_{J_α} in the effective model by choosing $E_J = E_J^*$ when fitting to the two-dimensional Hamiltonian (see Appendix E2).

2. Effective model

Here we provide a derivation and supporting explanations for the effective one-dimensional model for the 0- π Hamiltonian. A heuristic effective model for the 0- π qubit is

$$\hat{H} = 4E_{C_\alpha} \hat{n}_\alpha^2 - E_{J_\alpha} \cos \hat{\alpha} - E_{J_{2\alpha}} \cos 2\hat{\alpha}, \quad (\text{E3})$$

with $[\hat{\alpha}, \hat{n}_\alpha] = i$. In the limit of $E_{J_\alpha} \ll E_{C_\alpha} \ll E_{J_{2\alpha}}$, this represents a $4e$ -tunnelling element perturbed by a $2e$ -tunnelling term. This heuristic model was originally used to explain the behaviour of the current mirror qubit [6], for which the 0- π qubit is based on, and was later used in Refs. [11, 12, 23] for numerical analyses of the 0- π qubit. In Ref. [23], expressions for the parameters E_{C_α} , E_{J_α} and $E_{J_{2\alpha}}$ are derived in terms of the parameters for the 0- π qubit in a particular parameter regime. This derivation makes use of a Born-Oppenheimer approximation, motivated by the “mass separation” given by the energy restriction $E_{C_\theta} \ll E_{C_\varphi}$. Here we explain that the Born-Oppenheimer approximation is only valid in a restricted parameter regime where, in addition, $E_{C_\theta} < 2E_L$ and $2E_J \ll E_{C_\varphi}$. Note that neither of these latter inequalities are a requirement for topological protection of the 0- π qubit [Eq. (18)]. Moreover, we find that this is not the relevant parameter regime for performing a gate with

the 0- π qubit. In Appendix E2 a we closely follow the approach taken in Ref. [23] to derive an effective model using the Born-Oppenheimer approximation in the regime where $E_{C_\theta} < 2E_L$, and in Appendix E2 b we derive an effective model using a tight-binding approximation in the regime where $E_{C_\theta} \geq 2E_L$. The latter is the one-dimensional model that is used and discussed in the main text. In Appendix E2 c we compute the exponential scalings for the tunnelling rates in the tight-binding model, which are given in Eqs. (24) and (25).

a. Born-Oppenheimer approximation

The Born-Oppenheimer approximation makes use of the fact that $E_{C_\theta} \ll E_{C_\varphi}$ to separate the dynamics of the “heavy” degree of freedom (θ) from the “light” degree of freedom (φ) by assuming the latter is in its ground state. To this end, we treat $\hat{\theta}$ as a classical variable and take $4E_{C_\theta} \hat{n}_\theta \rightarrow 0$ in Eq. (16), yielding the following Hamiltonian for the φ degree of freedom

$$\hat{H}_\varphi = 4E_{C_\varphi} \hat{n}_\varphi^2 + E_L \hat{\varphi}^2 - 2E_J \cos \theta \cos \hat{\varphi}, \quad (\text{E4})$$

where we have fixed $\varphi_{\text{ext}} = 0$ for simplicity. The effective one-dimensional Hamiltonian in the Born-Oppenheimer approximation is then given by

$$\hat{H}_{\text{BO}} = 4E_{C_\theta} \hat{n}_\theta^2 + E_0(\hat{\theta}), \quad (\text{E5})$$

where $E_0(\hat{\theta})$ is the ground-state energy of Eq. (E4), and θ has been promoted back to an operator.

Crucially, owing to the assumption that the φ mode is in its ground state, the spectrum of Eq. (E5) is only accurate up to the i -th energy level of the 0- π Hamiltonian if $\Delta_{i0}^{0-\pi} < \Delta_{i0}^\varphi$, where $\Delta_{i0}^{0-\pi}$ and Δ_{i0}^φ denote the energy gap from the ground state to the i -th excited state of the 0- π Hamiltonian [Eq. (16)] and the Hamiltonian for the φ mode [Eq. (E4)], respectively. In Fig. 16(a) we plot the energy gaps for the second excited state of the 0- π Hamiltonian, $\Delta_{20}^{0-\pi}$, and the first excited state of the φ -mode Hamiltonian, Δ_{10}^φ . Here we find that the energy gap for the 0- π Hamiltonian is less than the energy gap for the φ -mode Hamiltonian when $E_{C_\theta} < 2E_L$, and that the two energy gaps become equal for $E_{C_\theta} \geq 2E_L$. The reason for this is that when $E_{C_\theta} < 2E_L$, the excitations in the 0- π Hamiltonian are plasmon-like with an energy gap given by $\Delta_{02}^{0-\pi} \approx 4\sqrt{E_J E_{C_\theta}}$. In contrast, the excitations of Eq. (E4) are fluxon-like with an energy gap given by $\Delta_{10}^\varphi \approx 4\sqrt{E_L E_{C_\varphi}}$. In Fig. 16(a) we also plot the value of the Josephson energy in the 0- π Hamiltonian, which is chosen to be the value that optimises the degeneracy of the qubit at zero external flux (see Appendix E1). This shows that when $E_{C_\theta} < 2E_L$, then $2E_J \lesssim E_{C_\varphi}$, and therefore $\Delta_{02}^{0-\pi} \lesssim \Delta_{10}^\varphi$. On the other hand, when $E_{C_\theta} \geq 2E_L$ then the excitations in the 0- π Hamiltonian become fluxon-like and the gaps become same as in the φ -mode Hamiltonian. Therefore, we conclude that the Born-Oppenheimer approximation is only a good approximation when $E_{C_\theta} < 2E_L$ and $2E_J < E_{C_\varphi}$.

We now estimate $E_0(\theta)$ under the above assumptions. With $2E_J < E_{C_\varphi}$, Eq. (E4) corresponds to a harmonic oscillator with frequency $\omega_\varphi = 4\sqrt{E_{C_\varphi}E_L}/\hbar$ that is perturbed by the θ -dependent tunnelling term $-2E_J \cos\theta \cos(\hat{\varphi})$. Therefore, the ground-state energy of Eq. (E4) may be approximated by the first and second-order corrections to the harmonic oscillator frequency,

$$E_0(\theta) \approx \frac{\hbar\omega_\varphi}{2} + E_0^{(1)} + E_0^{(2)}. \quad (\text{E6})$$

These corrections are obtained through perturbation theory and may be simplified as follows,

$$E_0^{(1)} = -2E_J \langle 0 | \cos \hat{\varphi} | 0 \rangle \quad (\text{E7a})$$

$$= -2E_J e^{-\pi Z_\varphi/2R_Q} \cos\theta, \quad (\text{E7b})$$

$$E_0^{(2)} = -\frac{4E_J^2}{\hbar\omega_\varphi} \sum_{n=1}^{\infty} \frac{|\langle n | \cos \hat{\varphi} | 0 \rangle|^2}{n} \cos^2\theta \quad (\text{E7c})$$

$$= -\frac{4E_J^2}{\hbar\omega_\varphi} e^{-\pi Z_\varphi/R_Q} \sum_{n=1}^{\infty} \frac{(\pi Z_\varphi/R_Q)^{2n}}{2n(2n)!} \cos^2\theta \quad (\text{E7d})$$

$$\sim -\frac{2E_J^2 R_Q}{\pi \hbar \omega_\varphi Z_\varphi} \cos^2\theta \quad (\text{E7e})$$

$$= -\frac{E_J^2}{2E_{C_\varphi}} \cos^2\theta, \quad (\text{E7f})$$

where $|n\rangle$ and $Z_\varphi/R_Q = \sqrt{E_{C_\varphi}/\pi^2 E_L} = \sqrt{L/4C_J}$ are the eigenstates and impedance for the unperturbed harmonic oscillator, respectively. In Eq. (E7d) we used that $\langle n | e^{i\hat{\varphi}} | 0 \rangle = e^{-\pi Z_\varphi/2R_Q} (\pi Z_\varphi/R_Q)^{n/2} / \sqrt{n!}$, and in Eq. (E7e) we used the following asymptotic scaling for the sum

$$\sum_{n=1}^{\infty} \frac{x^{4n}}{n(2n)!} \sim \frac{e^{x^2}}{x^2}, \quad (\text{E8})$$

which is justified since $Z_\varphi/R_Q \gg 1$.

Promoting θ back to an operator, and substituting Eqs. (E6), (E7b) and (E7f) into Eq. (E5), the effective one-dimensional Hamiltonian is

$$\hat{H}_{\text{BO}} = 4E_{C_\theta} \hat{n}_\theta^2 - 2E_J e^{-\pi Z_\varphi/2R_Q} \cos \hat{\theta} - \frac{E_J^2}{4E_{C_\varphi}} \cos 2\hat{\theta}, \quad (\text{E9})$$

where we have used that $2\cos^2\hat{\theta} = \cos 2\hat{\theta} + 1$ and neglected constant-energy terms. We see that this matches the heuristic model [Eq. (E3)], where the effective degree of freedom $\hat{\alpha}$ may be identified with the θ -mode of the 0 - π qubit, and the effective energies are given by

$$E_{C_\alpha} = E_{C_\theta}, \quad E_{J_\alpha} = 2E_J e^{-\pi Z_\varphi/2R_Q}, \quad E_{J_{2\alpha}} = \frac{E_J^2}{4E_{C_\varphi}}. \quad (\text{E10})$$

Importantly, the $2e$ tunnelling term is exponentially suppressed in Z_φ relative to the $4e$ -tunnelling term, agreeing with our intuition for the 0 - π qubit being an approximate π -periodic Josephson element.

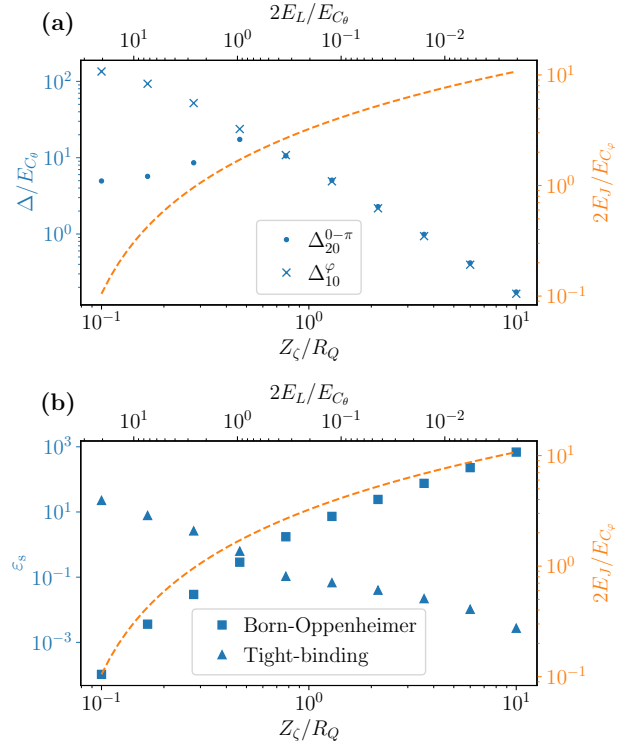


FIG. 16. Effective models. (a) Energy gaps for the two-dimensional 0 - π Hamiltonian [Eq. (16)] and the Hamiltonian for the φ mode [Eq. (E4)] as a function of the ζ -mode impedance Z_ζ . Energy gaps for the 0 - π Hamiltonian, $\Delta_{02}^{0-\pi}$, are shown by the dots and energy gaps for the φ mode Hamiltonian, Δ_{01}^φ are shown by crosses. Δ_{i0} denotes the energy gap between the i -th excited state and the ground state. (b) Spectral error ϵ_s [Eq. (E16)] for the effective models as a function of the ζ -mode impedance Z_ζ . Spectral errors for the Born-Oppenheimer model [Eq. (E5)] are shown with squares and spectral errors for the tight-binding model [Eq. (E14)] are shown with triangles. In (a) and (b) the charging energy ratio is fixed to $E_{C_\varphi}/E_{C_\theta} = 100$, and the corresponding values of E_J and E_L are shown by the orange dashed line and the upper axis, respectively.

b. Tight-binding approximation

As discussed above, when $E_{C_\theta} \geq 2E_L$, the Born-Oppenheimer approximation is no longer valid and $2E_J$ becomes larger than E_{C_φ} . Now E_J is the dominant energy in the 0 - π qubit and we use a tight-binding approximation instead of the Born-Oppenheimer approximation to reduce the Hamiltonian to a one-dimensional model. A two-dimensional tight-binding model was also used to derive an effective model for a multi-mode qubit in Ref. [25]. We follow a similar approach.

To begin with, we express the Hamiltonian in the basis of flux eigenstates localised at the minima of the potential $-2E_J \cos\theta \cos\varphi$. These are located at the positions $(\theta, \varphi) = (m_\theta\pi, m_\varphi\pi)$, where $m_\theta \in \{0, 1\}$ and $m_\varphi \in \mathbb{Z}$ such that $m_\theta + m_\varphi \in 2\mathbb{Z}$. We then enumerate these min-

ima by a single site index $m = 2\lfloor m_\varphi/2 \rfloor + m_\theta$. This facilitates the following one-dimensional tight-binding Hamiltonian

$$\hat{H}_{\text{TB}} = \sum_{m \in \mathbb{Z}} \left[E_L (\pi m)^2 |m\rangle\langle m| - t_1 (|m\rangle\langle m+1| + \text{h.c.}) - t_2 (|m\rangle\langle m+2| + \text{h.c.}) \right], \quad (\text{E11})$$

where $|m\rangle$ denotes the flux eigenstate at the m -th cosine well, and t_1 and t_2 represent nearest and next-nearest neighbour tunnelling rates, respectively. The next-nearest neighbour tunnelling path is purely in the φ direction, and its value is well-approximated by the formula for one-dimensional tunnelling when $E_{C_\varphi} \gg E_{C_\theta}$ [3]

$$t_2 = \frac{8E_{C_\varphi}}{\sqrt{\pi}} \left(\frac{4E_J}{E_{C_\varphi}} \right)^{3/4} e^{-4\sqrt{E_J/E_{C_\varphi}}}. \quad (\text{E12})$$

The nearest-neighbour tunnelling rate may be calculated from a two-dimensional WKB or instanton calculation along a numerically computed tunnelling path [14, 26]. In Appendix E 2 c we numerically compute its tunnelling path and show that it scales as

$$t_1 \propto e^{-2(\sqrt{2}-1)\sqrt{2E_J/E_{C_\theta}} - \pi(\sqrt{2}-1)\sqrt{E_J/2E_{C_\varphi}}}. \quad (\text{E13})$$

Note that whilst the distance for nearest-neighbour tunnelling is smaller than the next-nearest neighbour tunnelling path, its rate is exponentially suppressed in $\sqrt{E_{C_\varphi}/E_{C_\theta}}$ relative to t_2 due to the component of its tunnelling path in the θ direction. To obtain the exact value of t_1 , we numerically fit the spectrum for the one-dimensional model to the two-dimensional Hamiltonian with t_2 given by the formula in Eq. (E12). We show in Appendix E 2 c that its numerically fitted value is consistent with the scaling in Eq. (E13).

Introducing the operators $\hat{m} = \sum_{m \in \mathbb{Z}} |m\rangle\langle m|$ and $\cos(k\hat{p}_m) = \frac{1}{2} \sum_{m \in \mathbb{Z}} (|m\rangle\langle m+k| + \text{h.c.})$, Eq. (E11) may be written as

$$\hat{H}_{\text{TB}} = E_L \pi^2 \hat{m}^2 - 2t_1 \cos(\hat{p}_m) - 2t_2 \cos(2\hat{p}_m). \quad (\text{E14})$$

By identifying \hat{m} with \hat{n}_α and \hat{p}_m with \hat{a} , this takes the form of Eq. (E3) where the effective capacitive and Josephson energies are given by

$$E_{C_\alpha} = \pi^2 \frac{E_L}{4}, \quad E_{J_\alpha} = t_1, \quad E_{J_{2\alpha}} = t_2. \quad (\text{E15})$$

Note that here flux and charge have swapped roles relative to the original interpretation of Eq. (E3). This is similar to fluxonium where a periodic fluxon-basis is used [24].

In this tight-binding model, $\hat{\theta}$ may be replaced by $\pi\hat{n}_\alpha$ in the interaction terms Eqs. (20) and (21) since n_α is even when $\theta = 0$ and n_α is odd when $\theta = \pi$. This yields Eqs. (26) and (27), which we use for the numerical results in Figs. 5(a) to 5(d). Furthermore, since $\hat{\varphi}$ becomes

$\pi\hat{n}_\alpha$ in the effective model, the disorder term $\delta E_L \hat{\varphi} \hat{\zeta}$ becomes $\pi \delta E_L \hat{n}_\alpha \hat{\zeta}$, which we use for the numerical results in Figs. 6(a) and 6(b).

To compare the both effective models, we compute their spectral errors for the first five excited states, defined as

$$\varepsilon_s = \frac{1}{5} \sum_{i=1}^5 \frac{|E_i^{1\text{D}} - E_i^{2\text{D}} - E_0^{1\text{D}} + E_0^{2\text{D}}|}{E_i^{2\text{D}} - E_0^{2\text{D}}}, \quad (\text{E16})$$

where $E_i^{1\text{D}/2\text{D}}$ denotes the i -th eigenstate of the 1D/2D Hamiltonian. Figure 16(b) shows the spectral errors for both effective models as a function of Z_ζ/R_Q . Consistent with the regime of validity shown in Fig. 16(a) and discussed in Appendix E 2 a, we find that the Born-Oppenheimer model is a better approximation to the two-dimensional Hamiltonian when $E_{C_\theta} < 2E_L$, and the tight-binding model is a better approximation when $E_{C_\theta} \geq 2E_L$. Moreover, this transition occurs at the point where $2E_J \approx E_{C_\varphi}$, consistent with the assumptions made in each model. In particular, Fig. 16(b) shows that the tight-binding model is the better effective model when $Z_\zeta/R_Q \geq 1$. Since this is the relevant regime for our simulations, we use this as the effective model to simulate a gate with the $0-\pi$ qubit in Section III.

c. Calculation of tunnelling rate action

Here we calculate the exponential scaling of the nearest and next-nearest neighbour tunnelling rates t_1, t_2 for the tight-binding model, referred to as E_{J_α} and $E_{J_{2\alpha}}$, respectively, in the main text. These are given by e^{-S} , where S is the classical action [26, 56]:

$$S = \int_\ell \mathbf{n} \cdot d\boldsymbol{\theta}. \quad (\text{E17})$$

Here, $\boldsymbol{\theta} = (\varphi, \theta)$ and $\mathbf{n} = (n_\varphi, n_\theta)$ are the two-dimensional position and momentum vectors, and the integral is over the tunnelling path ℓ that minimises the action.

For these calculations, we consider the classical kinetic and potential energy corresponding to the two-dimensional $0-\pi$ Hamiltonian, Eq. (16), in the $E_L \rightarrow 0$ limit:

$$\begin{aligned} T &= 4E_{C_\varphi} n_\varphi^2 + 4E_{C_\theta} n_\theta^2, \\ V &= 2E_J (1 - \cos \varphi \cos \theta). \end{aligned} \quad (\text{E18})$$

We have also added $2E_J$ to the potential energy to ensure it is positive.

First, we compute the action for the next-nearest neighbour tunnelling path. Its path is a straight line in the φ direction as shown by the red line in Fig. 17(a). Therefore, Eq. (E17) reduces to

$$S_2 = \int_0^{2\pi} n_\varphi d\varphi. \quad (\text{E19})$$

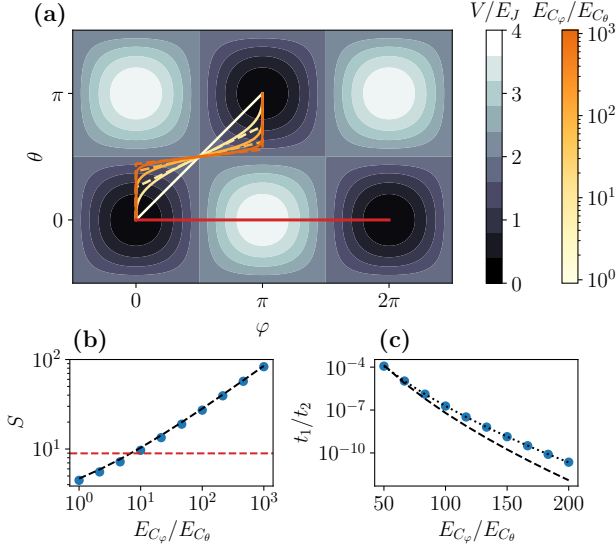


FIG. 17. Tight-binding model tunnelling paths and rates. (a) Nearest and next-nearest neighbour tunnelling paths for a $0-\pi$ qubit with $E_J/E_{C_\varphi} = 5$ and different charging energy ratios $E_{C_\varphi}/E_{C_\theta}$, in the $Z_\zeta \rightarrow \infty$ ($E_L = 0$) limit. The numerically computed nearest-neighbour tunnelling paths for different charging energy ratios are shown in the orange solid lines and the linear approximation for each path are shown in the dashed lines. The next-nearest neighbour tunnelling path is shown in the red line. (b) Classical action S for the tunnelling paths shown in panel (a) as a function of the charging energy ratio $E_{C_\varphi}/E_{C_\theta}$. Blue denotes the numerically computed action for the nearest-neighbour tunnelling paths shown in the solid orange lines in panel (a). The black dashed line denotes the theoretical expression for the nearest-neighbour action in Eq. (E21), calculated using the dashed lines in panel (a). The horizontal red dashed line denotes the action for the next-nearest neighbour tunnelling in Eq. (E20), corresponding to the red line in panel (a). (c) Ratio of nearest- to next-nearest-neighbour tunnelling rates t_1/t_2 as a function of the charging energy ratio $E_{C_\varphi}/E_{C_\theta}$. The blue circles denote the numerically computed tunnelling rates from fitting the one-dimensional Hamiltonian in Eq. (22) to the two-dimensional Hamiltonian in Eq. (16) with $Z_\zeta/R_Q = 10$ and $E_J/E_{C_\varphi} = 5$ [the same data as in Fig. 4(c)]. The dashed line denotes the scaling from the formulae for the tunnelling rates computed in Eqs. (E20) and (E21), and the dotted line is a fit to the blue circles.

Here, n_φ may be found by equating T and V in Eq. (E18) with $\theta = n_\theta = 0$, yielding $n_\varphi = \sqrt{E_J(1 - \cos \varphi)}/2E_{C_\varphi}$. Substituting into Eq. (E19) and computing the integrals results in

$$S_2 = 4\sqrt{\frac{E_J}{E_{C_\varphi}}}, \quad (\text{E20})$$

which leads to the exponential scaling in Eqs. (25) and (E12).

Next, we compute the action for the nearest-neighbour tunnelling path. In the case of equal charging energies,

the nearest-neighbour tunnelling path is given by the diagonal line connecting adjacent minima, as shown by the white line in Fig. 17(a). Solving the integral in Eq. (E17) along this diagonal path $\theta = \varphi$ with $E_{C_\theta} = E_{C_\varphi}$ in Eq. (E18) leads to $S_1 = S_2/2$. This means that nearest-neighbour tunnelling path is preferred over the next-nearest neighbour tunnelling when the charging energies are equal.

In the case of unequal charging energies, the tunnelling path is no longer a straight line. To find the tunnelling paths for unequal charging energies we numerically solve the classical equations of motion corresponding to Eq. (E18), following the approach of Refs. [14, 56]. The solid lines in Fig. 17(a) show the numerically computed paths over a range of charging energy ratios $E_{C_\varphi}/E_{C_\theta}$. To obtain a formula for the action corresponding to these paths, we approximate each path by the piecewise linear paths shown in the dashed lines in Fig. 17(a).

We set the slope of the diagonal segment to $\sqrt{E_{C_\theta}/E_{C_\varphi}}$, which we find is very close to the gradient of the numerically computed tunnelling paths at the saddle point $(\varphi, \theta) = (\pi/2, \pi/2)$. This slope determines the angle of the momentum vector, and its magnitude is found by equating T and V in Eq. (E18). The action along the diagonal segment is then found by computing the integral in Eq. (E17) along this line. The action for each vertical segment is found by setting $\varphi = n_\varphi = 0$ in Eq. (E18) and computing the integral in Eq. (E17) from $\theta = 0$ to $\theta = (1 - \sqrt{E_{C_\theta}/E_{C_\varphi}})\pi/2$. Adding the contribution from both linear segments and expanding to leading order in $E_{C_\theta}/E_{C_\varphi}$ leads to the following action

$$S_1 \approx 2(\sqrt{2} - 1)\sqrt{\frac{2E_J}{E_{C_\theta}}} + (\sqrt{2} - 1)\pi\sqrt{\frac{E_J}{2E_{C_\varphi}}}, \quad (\text{E21})$$

which is the scaling given in Eqs. (24) and (E13).

In Fig. 17(b) we plot the numerically computed action for the nearest-neighbour tunnelling as a function of the charging energy ratio $E_{C_\varphi}/E_{C_\theta}$ at a fixed value of $E_J/E_{C_\varphi} = 5$ in blue along with the equation for S_1 in Eq. (E21) in the black dashed line. We find good agreement over the entire range of charging energy ratios and that the agreement improves with increasing $E_{C_\varphi}/E_{C_\theta}$. We also plot the action for next-nearest-neighbour tunnelling S_2 from Eq. (E20) in the red dashed line. This shows that the nearest-neighbour action exceeds the next-nearest neighbour action for $E_{C_\varphi}/E_{C_\theta} \geq 10$. This means that next-nearest neighbour tunnelling will be preferred over nearest-neighbour tunnelling when $E_{C_\varphi}/E_{C_\theta} \geq 10$ for sufficiently large E_J .

In Fig. 17(c) we compare the analytically calculated scalings for the tunnelling rates to the numerically fitted values plotted in Fig. 4(c). Recall that the latter are obtained by fitting the one-dimensional Hamiltonian Eq. (22) to the two-dimensional Eq. (16) with $E_J/E_{C_\varphi} = 5$ and $Z_\zeta/R_Q = 10$, whereas the former are computed in the $Z_\zeta \rightarrow \infty$ limit. The blue cir-

cles shows the numerically fitted tunnelling rates and the black dashed line shows the scaling from Eqs. (E20) and (E21). A fit to the numerically computed tunnelling rates, shown by the dotted black line, shows that their

scaling is

$$\frac{t_1}{t_2} \propto e^{-2.2\sqrt{E_{C\phi}/E_{C\theta}}}. \quad (\text{E22})$$

The pre-factor in the exponential is close to the value obtained from Eqs. (E20) and (E21), which is $2(\sqrt{2} - 1)\sqrt{2E_J/E_{C\phi}} \approx 2.7$ for $E_J/E_{C\phi} = 5$. The smaller value from the numerical fit is likely due to the non-zero E_L , which will contribute more to the next-nearest neighbour action than the nearest-neighbour action.

-
- [1] Google Quantum AI and Collaborators, Suppressing quantum errors by scaling a surface code logical qubit, *Nature* **614**, 676 (2023).
- [2] Google Quantum AI and Collaborators, Quantum error correction below the surface code threshold, *Nature* **638**, 920 (2024).
- [3] J. Koch, T. M. Yu, J. Gambetta, A. A. Houck, D. I. Schuster, J. Majer, A. Blais, M. H. Devoret, S. M. Girvin, and R. J. Schoelkopf, Charge-insensitive qubit design derived from the Cooper pair box, *Physical Review A* **76** (2007).
- [4] V. E. Manucharyan, J. Koch, L. I. Glazman, and M. H. Devoret, Fluxonium: Single Cooper-Pair Circuit Free of Charge Offsets, *Science* **326**, 113–116 (2009).
- [5] A. Gyenis, A. Di Paolo, J. Koch, A. Blais, A. A. Houck, and D. I. Schuster, Moving beyond the Transmon: Noise-Protected Superconducting Quantum Circuits, *PRX Quantum* **2** (2021).
- [6] A. Kitaev, Protected qubit based on a superconducting current mirror (2006), [arXiv:cond-mat/0609441](https://arxiv.org/abs/cond-mat/0609441) [cond-mat.mes-hall].
- [7] P. Brooks, A. Kitaev, and J. Preskill, Protected gates for superconducting qubits, *Physical Review A* **87** (2013).
- [8] J. M. Dempster, B. Fu, D. G. Ferguson, D. I. Schuster, and J. Koch, Understanding degenerate ground states of a protected quantum circuit in the presence of disorder, *Physical Review B* **90** (2014).
- [9] A. Gyenis, P. S. Mundada, A. Di Paolo, T. M. Hazard, X. You, D. I. Schuster, J. Koch, A. Blais, and A. A. Houck, Experimental Realization of a Protected Superconducting Circuit Derived from the $0-\pi$ Qubit, *PRX Quantum* **2** (2021).
- [10] J. Kim, I. Rosen, J. An, M. Hays, A. Di Paolo, L. Ding, K. Azar, J. Gertler, T. Hazard, M. Gingras, B. Niedzielski, H. Stickler, K. Sliwa, M. Schwartz, J. Yoder, T. Orlando, J. Grover, K. Serniak, and W. Oliver, Measurement of soft zero- π qubit with parallel-plate capacitors, in *APS March Meeting Abstracts*, Vol. 2024 (2024) p. M48.005.
- [11] F. Hassani, *Superconducting qubits capable of dynamic switching between protected and high-speed control regimes*, *Ph.D. thesis*, Institute of Science and Technology Austria (2024).
- [12] A. Di Paolo, A. L. Grimsmo, P. Groszkowski, J. Koch, and A. Blais, Control and coherence time enhancement of the $0-\pi$ qubit, *New Journal of Physics* **21**, 043002 (2019).
- [13] D. Gottesman, A. Kitaev, and J. Preskill, Encoding a qubit in an oscillator, *Physical Review A* **64** (2001).
- [14] W. C. Smith, A. Kou, X. Xiao, U. Vool, and M. H. Devoret, Superconducting circuit protected by two-Cooper-pair tunneling, *npj Quantum Information* **6** (2020).
- [15] G. Pantaleoni, B. Q. Baragiola, and N. C. Menicucci, Modular Bosonic Subsystem Codes, *Phys. Rev. Lett.* **125**, 040501 (2020).
- [16] M. H. Shaw, A. C. Doherty, and A. L. Grimsmo, Stabilizer Subsystem Decompositions for Single- and Multimode Gottesman-Kitaev-Preskill Codes, *PRX Quantum* **5**, 010331 (2024).
- [17] A. Y. Kitaev, Quantum computations: algorithms and error correction, *Russian Mathematical Surveys* **52**, 1191 (1997).
- [18] D. Aharonov and M. Ben-Or, Fault-tolerant quantum computation with constant error, in *Proceedings of the Twenty-Ninth Annual ACM Symposium on Theory of Computing*, STOC '97 (Association for Computing Machinery, New York, NY, USA, 1997) p. 176–188.
- [19] E. Knill, R. Laflamme, and W. H. Zurek, Resilient quantum computation: error models and thresholds, *Proceedings of the Royal Society of London. Series A: Mathematical, Physical and Engineering Sciences* **454**, 365–384 (1998).
- [20] Y. R. Sanders, J. J. Wallman, and B. C. Sanders, Bounding quantum gate error rate based on reported average fidelity, *New Journal of Physics* **18**, 012002 (2015).
- [21] R. Kueng, D. M. Long, A. C. Doherty, and S. T. Flammia, Comparing Experiments to the Fault-Tolerance Threshold, *Physical Review Letters* **117**, 170502 (2016).
- [22] A. Blais, A. L. Grimsmo, S. M. Girvin, and A. Wallraff, Circuit quantum electrodynamics, *Reviews of Modern Physics* **93** (2021).
- [23] F. Shen, *Theoretical analysis of a protected superconducting qubit*, *Master's thesis*, University of Waterloo (2015).
- [24] J. Koch, V. Manucharyan, M. H. Devoret, and L. I. Glazman, Charging Effects in the Inductively Shunted Josephson Junction, *Physical Review Letters* **103** (2009).
- [25] W. C. Smith, M. Villiers, A. Marquet, J. Palomo, M. R. Delbecq, T. Kontos, P. Campagne-Ibarcq, B. Douçot, and Z. Leghtas, Magnifying Quantum Phase Fluctuations with Cooper-Pair Pairing, *Phys. Rev. X* **12**, 021002 (2022).
- [26] B. Zwiebach, *Mastering Quantum Mechanics* (MIT Press, 2022) p. 1200.
- [27] T. W. Larsen, K. D. Petersson, F. Kuemmeth, T. S. Jespersen, P. Krogstrup, J. Nygård, and C. M. Marcus, Semiconductor-Nanowire-Based Superconducting Qubit, *Physical Review Letters* **115** (2015).

- [28] L. Banszerus, C. W. Andersson, W. Marshall, T. Lindemann, M. J. Manfra, C. M. Marcus, and S. Vaitiekėnas, The hybrid Josephson rhombus: A superconducting element with tailored current-phase relation (2024), [arXiv:2406.20082](https://arxiv.org/abs/2406.20082) [cond-mat.mes-hall].
- [29] A. Miano and O. A. Mukhanov, Symmetric traveling wave parametric amplifier, *IEEE Transactions on Applied Superconductivity* **29**, 1 (2019).
- [30] R. Lescanne, M. Villiers, T. Peronmin, A. Sarlette, M. Delbecq, B. Huard, T. Kontos, M. Mirrahimi, and Z. Leghtas, Exponential suppression of bit-flips in a qubit encoded in an oscillator, *Nature Physics* **16**, 509 (2020).
- [31] A. Miano, G. Liu, V. V. Sivak, N. E. Frattini, V. R. Joshi, W. Dai, L. Frunzio, and M. H. Devoret, Frequency-tunable Kerr-free three-wave mixing with a gradiometric SNAIL, *Applied Physics Letters* **120**, 184002 (2022).
- [32] M. D. Hutchings, J. B. Hertzberg, Y. Liu, N. T. Bronn, G. A. Keefe, M. Brink, J. M. Chow, and B. L. T. Plourde, Tunable Superconducting Qubits with Flux-Independent Coherence, *Physical Review Applied* **8**, 044003 (2017).
- [33] N. Didier, E. A. Sete, J. Combes, and M. P. da Silva, AC Flux Sweet Spots in Parametrically Modulated Superconducting Qubits, *Physical Review Applied* **12**, 054015 (2019).
- [34] I. V. Pechenezhskiy, R. A. Mencia, L. B. Nguyen, Y.-H. Lin, and V. E. Manucharyan, The superconducting quasicharge qubit, *Nature* **585**, 368–371 (2020).
- [35] M. Peruzzo, A. Trioni, F. Hassani, M. Zemlicka, and J. M. Fink, Surpassing the resistance quantum with a geometric superinductor, *Physical Review Applied* **14** (2020).
- [36] P. Groszkowski, A. Di Paolo, A. L. Grimsmo, A. Blais, D. I. Schuster, A. A. Houck, and J. Koch, Coherence properties of the $0-\pi$ qubit, *New Journal of Physics* **20**, 043053 (2018).
- [37] C. Cohen-Tannoudji, *Atom-photon interactions* (Wiley, 1992) p. 656.
- [38] V. V. Albert, K. Noh, K. Duivenvoorden, D. J. Young, R. T. Brierley, P. Reinhold, C. Vuillot, L. Li, C. Shen, S. M. Girvin, B. M. Terhal, and L. Jiang, Performance and structure of single-mode bosonic codes, *Phys. Rev. A* **97**, 032346 (2018).
- [39] F. Motzoi, J. M. Gambetta, P. Rebentrost, and F. K. Wilhelm, Simple Pulses for Elimination of Leakage in Weakly Nonlinear Qubits, *Phys. Rev. Lett.* **103**, 110501 (2009).
- [40] M. T. P. Nguyen and M. H. Shaw, Error correction for non-Clifford gates in the GKP code, forthcoming.
- [41] V. Sivak, N. Frattini, V. Joshi, A. Lingenfelter, S. Shankar, and M. Devoret, Kerr-Free Three-Wave Mixing in Superconducting Quantum Circuits, *Phys. Rev. Appl.* **11**, 054060 (2019).
- [42] T. Hillmann, F. Quijandría, G. Johansson, A. Ferraro, S. Gasparinetti, and G. Ferrini, Universal Gate Set for Continuous-Variable Quantum Computation with Microwave Circuits, *Phys. Rev. Lett.* **125**, 160501 (2020).
- [43] A. M. Eriksson, T. Sépulcre, M. Kervinen, T. Hillmann, M. Kudra, S. Dupouy, Y. Lu, M. Khanahmadi, J. Yang, C. Castillo-Moreno, P. Delsing, and S. Gasparinetti, Universal control of a bosonic mode via drive-activated native cubic interactions, *Nature Communications* **15** (2024).
- [44] V. Manucharyan, *Superinductance*, Ph.D. thesis, Yale University (2012).
- [45] K. Kalashnikov, W. T. Hsieh, W. Zhang, W.-S. Lu, P. Kamenov, A. Di Paolo, A. Blais, M. E. Gershenson, and M. Bell, Bifluxon: Fluxon-Parity-Protected Superconducting Qubit, *PRX Quantum* **1** (2020).
- [46] F. Hassani, M. Peruzzo, L. N. Kapoor, A. Trioni, M. Zemlicka, and J. M. Fink, Inductively shunted transmons exhibit noise insensitive plasmon states and a fluxon decay exceeding 3 hours, *Nature Communications* **14** (2023).
- [47] T. Rajabzadeh, Z. Wang, N. Lee, T. Makihara, Y. Guo, and A. H. Safavi-Naeini, Analysis of arbitrary superconducting quantum circuits accompanied by a Python package: SQcircuit, *Quantum* **7**, 1118 (2023).
- [48] U. Vool and M. Devoret, Introduction to quantum electromagnetic circuits, *International Journal of Circuit Theory and Applications* **45**, 897–934 (2017).
- [49] X. You, J. A. Sauls, and J. Koch, Circuit quantization in the presence of time-dependent external flux, *Physical Review B* **99** (2019).
- [50] R.-P. Riwar and D. P. DiVincenzo, Circuit quantization with time-dependent magnetic fields for realistic geometries, *npj Quantum Information* **8**, 36 (2022).
- [51] J. A. Fleck, J. R. Morris, and M. D. Feit, Time-dependent propagation of high energy laser beams through the atmosphere, *Applied physics* **10**, 129 (1976).
- [52] We note that such a decomposition is well-defined for states whose support vanishes at the values $\theta = -\pi/2, \pi/2$, which is the case for the states considered in this work. This is a sufficient condition to satisfy the θ -mode periodic boundary condition: $\psi(\theta = -\pi/2) = \lim_{\theta \rightarrow 3\pi/2} \psi(\theta)$, since it allows us to equip the states in the gauge subsystem with the consistent boundary condition $\psi(\tilde{\theta} = -\pi/2) = \lim_{\tilde{\theta} \rightarrow \pi/2} \psi(\tilde{\theta}) = 0$.
- [53] D. Aharonov, A. Kitaev, and N. Nisan, Quantum Circuits with Mixed States (1998), [arXiv:quant-ph/9806029](https://arxiv.org/abs/quant-ph/9806029) [quant-ph].
- [54] M. A. Nielsen, A simple formula for the average gate fidelity of a quantum dynamical operation, *Physics Letters A* **303**, 249 (2002).
- [55] J. Preskill, *Kitaev superconducting qubit* (2007), written notes.
- [56] V. Benderskii, S. Grebenshchikov, and G. Mil'nikov, Tunneling splittings in model 2D potentials. III. Generalization to N-dimensional case, *Chemical Physics* **198**, 281 (1995).